

CONSTRUCTION AND APPLICATION OF ANTHROPOMORPHIC PHANTOMS FOR USE
IN CT DOSE STUDIES

By

JAMES FREDERICK WINSLOW

A DISSERTATION PRESENTED TO THE GRADUATE SCHOOL
OF THE UNIVERSITY OF FLORIDA IN PARTIAL FULFILLMENT
OF THE REQUIREMENTS FOR THE DEGREE OF
DOCTOR OF PHILOSOPHY

UNIVERSITY OF FLORIDA

2009

© 2009 James Frederick Winslow

This work is dedicated to my loving wife Celeste, my brilliant children Abigail and Preston, and my wonderful parents Robert and Bonnie - Without their sacrifice and support, none of this would have been possible.

ACKNOWLEDGMENTS

First and foremost, I would like to thank my advisor and the chairman of my supervisory committee, Dr. David Hintenlang. Dr. Hintenlang's guidance, instruction, friendship, support, and availability was invaluable, and my time at the University of Florida was much richer because of my relationship with him. I would also like to thank each of my committee members, including Dr. Manuel Arreola, Dr. Wesley Bolch, and Dr. Bruce Welt. I am very appreciative for their assistance with my PhD dissertation, but am also especially grateful for their advice and support with regard to career and life in general.

I also want to thank my fellow students, past and present, in the Nuclear and Radiological Engineering Department. Kyle Jones, Ryan Fisher, Dan Hyer, and Chris Tien have been particularly important to the progress I have made towards completing my dissertation; I am much further along than I would have been without their help. Choonsik Lee has been such a great help. I really appreciate his finishing the MDCT Monte Carlo simulations (after he left the department!). I also want to express my gratitude to Jason Parker, Matthew Studenski, William Moloney, and Perry Johnson. These people have been great friends and great fellow students.

The staff in the Nuclear and Radiological Engineering Department also deserves my debt of gratitude. They have been so helpful and knowledgeable, that the problems that would inevitably occur were always short-lived. I also want to thank Dr. Alireza Haghghat for everything, especially for holding the annual departmental Christmas/Holiday party, at which I was able to get to know everybody in the department, and their families, much better than I would have otherwise. Also, I am thankful to the faculty within the program. Their expert instruction and being always available to answer my questions, both related to and apart from class, has helped me immeasurably.

Finally, I want to thank my family and friends for their love and support. The friends I have made at the University of Florida have been great in so many ways. I would like to express my gratitude to my parents for everything they have done for me over the years. Most importantly, I would like to extend my deepest gratitude to my wife Celeste, and my children Abigail and Preston; their support and sacrifice has been incredible.

I suppose it is worth thanking the Florida Gators for their four National Championships in four years; that was surely the icing on the cake of a great UF experience.

TABLE OF CONTENTS

	<u>page</u>
ACKNOWLEDGMENTS	4
LIST OF TABLES	9
LIST OF FIGURES	10
ABSTRACT	14
CHAPTER	
1 INTRODUCTION	16
Background and Significance	18
Dosimetric Quantities	18
Radiation Effects and Risks	20
Dosimeters	23
Strategies for Reducing Patient Dose in CT	27
Patient Simulation in CT	29
Image Quality Assessment in CT	30
2 CONSTRUCTION OF ANTHROPOMORPHIC PHANTOMS FOR USE IN DOSIMETRY STUDIES	40
Introduction	40
Methods	42
Materials	42
Phantom Construction Methodology	44
Results	50
Materials	50
Completed Phantom	50
Discussion	51
Conclusion	52
3 CT ABDOMEN/PELVIS DOSIMETRY STUDY	57
Introduction	57
Materials and Methods	57
Study Selection	57
Dosimetry System and Integration	58
Selection of Point Dose Measurement Locations	58
Technique Selection	59
Overranging, Beam Width, and Ramp-Up Time	60
Results	61
Detector Collimation Width	62

	Effective Dose	64
	Overranging, Beam Width, and Ramp-Up Time.....	66
	Discussion.....	67
	Overbeaming	67
	Overranging.....	69
	Conclusions.....	71
4	COMPARISON TO MONTE CARLO: CT ABDOMEN DOSIMETRY STUDY	82
	Introduction.....	82
	Materials and Methods	82
	Computational Phantom.....	82
	Computational Model of the CT Scanner.....	83
	Monte Carlo Codes.....	83
	Conversion to Absolute Organ Absorbed Dose	83
	Scan Parameters.....	84
	Results.....	84
	Discussion.....	86
	Comparison of Measured and Simulated Data.....	86
	Sources of Error.....	87
	Detector Collimation Width Comparison.....	88
	Conclusions.....	89
5	TEMPORAL/SPATIAL MODULATION OF DOSE IN MDCT.....	94
	Introduction.....	94
	Materials and Methods	96
	Temporal Modulation of Dose	96
	Cumulative Point Dose.....	97
	Total Dose to Radiosensitive Tissues.....	99
	Starting Angle Study	100
	Sample Set of Total Point Dose Measurements	101
	Results.....	101
	Temporal Modulation of Dose	101
	Cumulative Point Dose.....	102
	Total Dose to Radiosensitive Tissues.....	105
	Starting Angle Study	106
	Sample Distribution of Total Point Dose Measurements	106
	Discussion.....	106
	Cumulative Point Dose Measurements	108
	Total Dose to Radiosensitive Tissues.....	111
	Conclusions.....	112
6	A DOSIMETER RESPONSE WEIGHTED TECHNIQUE FOR MEASURING EFFECTIVE DOSE CONTRIBUTIONS.....	125
	Introduction.....	125

Methods and Materials	126
TLDs and OSLs	126
FOC Dosimetry	128
Results.....	130
Discussion.....	131
Conclusions.....	133
7 CONCLUSIONS	134
Results of This Work.....	134
Future Work and Development	135
Phantom Construction	135
Dose Distribution to Peripheral Axes in MDCT	136
FOC Dosimetry	137
Final Words	137
LIST OF REFERENCES.....	138
BIOGRAPHICAL SKETCH	144

LIST OF TABLES

<u>Table</u>	<u>page</u>
1-1 Recommended tissue weighting factors ⁵	32
1-2 Solid cancer cases by dose category ²	33
1-3 Detriment adjusted nominal risk coefficients for stochastic effects after exposure to radiation at low dose rate (10-2 Sv-1) ¹¹	33
1-4 Estimated effective radiation dose for common diagnostic imaging tests (D. Lockwood, J Radiol Nursing 26 , 121-124 (2007), Table 1, p 122).	34
1-5 Comparison of dosimetry systems with desirable characteristics for diagnostic dosimetry.....	36
3-1 Active marrow in a given bone expressed as a percentage of active marrow in the body for a 40 year old human. ⁵⁶	73
3-2 Phantom point dose measurement locations.	73
3-3 The portion of radiosensitive tissue located between slice 92 and 181 as compared to the tissue amount within the entire phantom.	78
4-1 Comparison of simulated and measured organ doses (mGy) for detector collimation widths of 16×0.75 mm (12 mm) and 16×1.5 mm (24 mm). Organs located within the user planned scan volume are in bold.	90
4-2 Comparison of the contributions to effective dose (mSv) for detector collimation widths of 16×0.75 mm (12 mm) and 16×1.5 mm (24 mm) from the organs considered in both the simulated and physically measured studies.	91
5-1 Minimum values, maximum values, average values, and standard deviations for normalized point dose distributions.	121
5-2 Minimum values, maximum values, average values, and standard deviations of normalized total organ/tissue doses	122
5-3 Normalized total point dose average for pitch 1.5 divided by that for pitch 1	123
5-4 Normalized total point dose average for detector collimation 40 mm divided by that for detector collimation 24 mm.....	123
5-5 Results for the MDCT starting angle study.	124
5-6 Comparison of FOC measured and calculated total point dose metrics for pitch 1.	124
5-7 Comparison of FOC measured and calculated total point dose metrics for pitch 1.5.	124

LIST OF FIGURES

<u>Figure</u>	<u>page</u>
1-1 Estimated number of CT scans performed annually in the United States (D. J. Brenner and E. J. Hall, N Engl J Med 357 (22), 2277-2284 (2007), Figure 2, p. 2280).	32
1-2 The head and body CTDI phantoms.	32
1-3 Number of excess cancer deaths caused by a single radiation exposure of 0.1 Gy as a function of age at the time of exposure and gender (H. D. Royal, Semin Nucl Med 38 (5), 392-402 (2008), Figure 4, p. 400).	33
1-4 Estimated dependence of lifetime radiation induced risk of cancer vs. age at exposure for two common radiogenic cancers (D. J. Brenner and E. J. Hall, N Engl J Med 357 (22), 2277-2284 (2007), Figure 4, p. 2282)	35
1-5 Schematic of UF plastic scintillator FOC dosimetry system.	37
1-6 Normalized sensitivity of the FOC dosimeter, as a function of depth in soft tissue-equivalent material.	37
1-7 Commercially available phantoms. A) The CIRS ATOM® phantom series. B) The RANDO® phantom.	37
1-8 The UF pediatric phantom series. A) MIRD phantom. B) Newborn Phantom. C) 1 year old phantom.....	38
1-9 Cross-sectional diagrams of the ACR accreditation phantom nodules. A) Nodule 1 examines CT number and slice width accuracy. B) Nodule 2 examines low-contrast resolution. C) Nodule 3 is used to assess image uniformity. D) Nodule 4 examines high-contrast (spatial) resolution (C. H. McCollough, M. R. Bruesewitz, M. F. McNitt-Gray, K. Bush, T. Ruckdeschel, J. T. Payne, J. A. Brink and R. K. Zeman, Med Phys 31 (9), 2423-2442 (2004), Figure 13, p. 2441).	38
1-10 Measured ESF, LSF, and MTF. A) The resulting ESF along a spherical surface derived from phantom data. B) The LSF computed from the ESF. C) The derived MTF (B. Li, G. B. Avinash and J. Hsieh, Med Phys 34 (10), 3732-3738 (2007), Figure 7, p. 3735).44.....	39
2-1 The steps in the phantom construction process: segmented CT image (top left), soft tissue bitmap (top right), VisionPro engraving path (bottom left), engraving system milling a soft tissue mold (bottom right).	54
2-2 A fully formed phantom slice. A) STES. B) LTES. C) BTES.	54

2-3	The UF adult phantom series. A) Phantom (i.e., GatorMan) based on a segmented CT data set of an adult male. B) Phantom based on a computational adult female hybrid data set. C) Phantom based on a computational adult male hybrid data set.....	55
2-4	The computational adult hybrid 50th percentile adult male phantom.	55
2-5	A CT topogram of a tomographic physical phantom.....	56
3-1	Abdomen/pelvis scan range as provided by the UF Shands Department of Radiology website (Clinical Protocol Database, radiology practice Committee of the Department of Radiology, University of Florida. Copyright 2008, http://xray.ufl.edu/protocols/documents/ct/body/abdomen_pelvis.pdf).	72
3-2	Schematic of the experimental setup used to evaluate CT x-ray tube ramp-up and overranging. The dashed pink lines indicate the user planned scan length.	72
3-3	Absorbed dose measurement for all point dose locations for detector collimation widths of 16×1.5 mm (black) and 16×0.75 mm (red). Imaged scan range is indicated by the blue region.....	75
3-4	Differences in absorbed dose measurement for all point dose locations for detector collimation widths of 16×1.5 mm (black) and 16×0.75 mm (red). Imaged scan range is indicated by the blue region.	75
3-5	Weighted absorbed dose measurement for all point dose locations for detector collimation widths of 16×1.5 mm (black) and 16×0.75 mm (red). Imaged scan range is indicated by the blue region.	76
3-6	Weighted point organ dose differences for detector collimation widths of 16×1.5 mm (black) and 16×0.75 mm (red). Imaged scan range is indicated by the blue region.....	76
3-7	Ratio of corresponding absorbed dose measurements for 24 mm detector collimation width and 12 mm detector collimation width for all points within the imaged scan range.....	77
3-8	Real-time FOC dosimetric data from the experiment illustrated in Figure 3-10. The x-axis was converted to distance using measured CT table speed values.	77
3-9	Schematic illustrating the difference in overbeaming for two different detector collimation widths over an identical scan length. Represented are the primary beam incident on the detector array (dark blue), the primary beam penumbra not incident on the detector array (light blue), and the detector array (gold).	79
3-10	The overbeaming present in a 24 mm scan section within the user planned scan range due to 16×1.5 mm and 16×0.75 mm detector collimation widths. Represented are the primary beam incident on the detector array (dark blue), the primary beam penumbra not incident on the detector array (light blue), and the detector array (gold).	79

3-11	A simplified depiction of overranging for helical MDCT scanning. Definitions of overranging vary; either the difference between planned and exposed scan length (Def 1) or the difference between imaged and exposed scan length (Def 2) is used. (A. J. van der Molen and J. Geleijns, Radiology 242 (1), 208-216 (2007), Figure 1, p. 210).....	80
3-12	Overview setup used by van der Molen et al. I is the ionization chamber, C _i is the collimator, D _i is the detector, D _o is the dosimeter, and F _i is the focal spot. (A. J. van der Molen and J. Geleijns, Radiology 242 (1), 208-216 (2007), Figure 2, p. 210)	80
3-13	Representative graph of the relationship of dose to planned CT scan length. (A. J. van der Molen and J. Geleijns, Radiology 242 (1), 208-216 (2007), Figure 3, p. 211)	81
4-1	Differences in corresponding simulated average organ dose measurements for detector collimation widths of 16×1.5 mm (black) and 16×0.75 mm (red). Imaged scan range is indicated by the blue region.	92
4-2	Differences in weighted simulated average organ dose measurements for detector collimation widths of 16×1.5 mm (black) and 16×0.75 mm (red). Imaged scan range is indicated by the blue region.	92
4-3	Ratio of corresponding simulated average organ dose measurements for 16×1.5 mm and 16×0.75 mm detector collimation width within the user-planned scan range	93
5-1	Schematic for the starting angle study.....	114
5-2	Normalized plot of FOC dosimeter counts received at a point located within the lens of the eye of the GatorMan phantom, in the center of the primary beam, during a single axial MDCT scan.....	114
5-3	Axial-based normalized helical dose rate plot at a point located within the lens of the eye of the GatorMan phantom, while continuously in the primary beam, during a hypothetical helical MDCT scan with no table translation, plotted as a function of index i, and time.....	115
5-4	Total normalized point dose as a function of distance expected near the region of the lens of the eye for settings of pitch 1, detector collimation 24 mm, for a given x-ray tube starting angle and starting scan location. The blue curve represents the dose distribution that results when the beam width is 28.3 mm. The red curve results if the beam width was equal to the detector collimation (24 mm).....	115
5-5	Total normalized point dose as a function of distance expected near different tissue locations for settings of pitch 1 and detector collimation 24 mm.....	116
5-6	Total normalized point dose as a function of distance expected near different tissue locations for settings of pitch 1.5 and detector collimation 24 mm.....	116

5-7	Total normalized point dose as a function of distance expected near different tissue locations for settings of pitch 1 and detector collimation 40 mm.....	117
5-8	Total normalized point dose as a function of distance expected near different tissue locations for settings of pitch 1.5 and detector collimation 40 mm.....	117
5-9	The degree of variation in total organ/tissue dose depending on the organ's location with respect to the point dose distribution for pitch 1 and detector collimation 24 mm.	118
5-10	The degree of variation in total organ/tissue dose depending on the organ's location with respect to the point dose distribution for pitch 1.5 and detector collimation 24 mm.	118
5-11	The degree of variation in total organ/tissue dose depending on the organ's location with respect to the point dose distribution for pitch 1 and detector collimation 40 mm.	119
5-12	The degree of variation in total organ/tissue dose depending on the organ's location with respect to the point dose distribution for pitch 1.5 and detector collimation 40 mm.	119
5-13	Normalized organ/tissue mass distributions plotted against index j corresponding to using a pitch 1.5, detector collimation 24 mm, and gantry rotation time 0.5s. The step pattern for the thyroid, stomach, and testes is due to deriving mass distributions from a segmented CT data set comprising 5 mm axial slices.....	120
5-14	Synchronized FOC dosimeter responses used to determine the starting angle of the activated x-ray tube.....	123

Abstract of Dissertation Presented to the Graduate School
of the University of Florida in Partial Fulfillment of the
Requirements for the Degree of Doctor of Philosophy

CONSTRUCTION AND APPLICATION OF ANTHROPOMORPHIC PHANTOMS FOR USE
IN CT DOSE STUDIES

By

James Frederick Winslow

August 2009

Chair: David E. Hintenlang
Major: Nuclear Engineering Sciences

The unmatched diagnostic information provided by CT, comes with a cost of increased radiation dose to patients. It is therefore useful to assess the radiation dose to patients for particular CT studies. Absorbed dose, effective dose, and organ dose measurements are all metrics that permit a better understanding of risks associated with radiation exposures to patients receiving CT studies. Anthropomorphic phantoms constructed from tissue-equivalent materials have historically been used to provide a physical representation of the body's anatomy and attenuation characteristics for radiation dosimetry studies.

This dissertation expands upon methods originally published by White et al. [Med Phys **5**, 467-479 (1978)], and later improved upon by Jones et al. [Med Phys **30**, 2072-2081 (2003)]. Discussed is a method of construction for a tomographic anthropomorphic phantom. Phantoms constructed using this process have the distinct advantages of precisely knowing the anatomy with respect to the CT data set used for phantom construction, and having a corresponding segmented computational phantom that was created from the same original CT data set, such as those developed by Lee et al. [Med Phys **33**, 380-390 (2006)].

In addition to development of the phantom construction process, a phantom abdominal MDCT study is presented that illustrates effects of overbeaming and overranging on radiation

doses received by patients undergoing MDCT studies. A fiber optic coupled (FOC) dosimetry system was used in the physical phantom to measure average organ doses. These average organ doses were compared with those derived using Monte Carlo simulations. Also presented is an analysis of the quasi-periodic dose distributions in superficial phantom locations that occur in MDCT scanning. These dose distributions result in increased uncertainty in point dose measurements, and a shift in their phase could potentially be used to reduce average organ doses in smaller, more superficially located organs. Finally, a more convenient (for TLD dosimetry) and cost-effective (for FOC dosimetry) alternative method for measuring contributions to effective dose is discussed. Here, the ICRP 103 tissue weighting for effective dose is accomplished physically rather than computationally.

CHAPTER 1 INTRODUCTION

Developed in the 1970's, the first generation of computed tomography (CT) scanners included a single thin x-ray beam and a single x-ray detector element. Initially, CT was used almost exclusively to rule out malignant disease or replace more dangerous procedures. Technological innovations have improved the utility of CT. Development of slip ring electrical energy transfer permitted continuous gantry rotation, and subsequently spiral and helical scanning. Greatly improved heat storage and transfer capability within specially designed CT x-ray tubes, allowed increasingly faster sub-second scans. Additionally, multirow detector arrays were developed to increase coverage per gantry rotation. From the 4-slice multidetector row CT (MDCT) introduced in 1998, MDCT systems of 16, 40, 64, even 256 rows are available. System software and computational power has also improved greatly, allowing for real-time 3-D displays of volume rendered data. With these technological improvements have come expanded clinical applications of CT, effectively diagnosing ailments in a variety of organ systems, including lungs, liver, stomach, pancreas, colon, kidneys, and coronary vasculature.^{1,2} Figure 1-1 below shows the estimated number of CT scans performed annually in the United States.¹

The unmatched diagnostic information provided by CT, comes with the cost of increased radiation dose to patients. Background (natural) sources are responsible for 85% of the total annual population exposure, approximately 3-3.6 mSv per year. Roughly 14% of the remainder is radiation from medical sources, with 67-75% of this exposure resulting from CT, making CT the largest source of radiation after background.^{1,2,4,5} In the United States, it has been estimated that per capita radiation dose from CT has increased from 0.67 mSv per year in 1980, to more than 3 mSv per year in 2008.² This illustrates the sharp trend towards increasing dose to the population from CT.

The CT dose index (CTDI), useful for quality control and understanding the relationship between techniques and dose, is not directly related to organ dose or risk. CTDI can be used to obtain the dose length product (DLP), which can then be combined with an empirically obtained weighting factor that is a function of body region to approximate effective dose. Effective dose is a useful metric for radiation risk estimation because it allows different CT scan scenarios to be compared with each other, and with exposures such as those present in the largest epidemiological low dose radiation studies. In order to calculate effective dose, organ dose measurements must be known. Organ doses can be predicted using deterministic simulations of radiation transport through computational phantoms such as the voxelized phantoms developed at the University of Florida.^{2, 7-12} More directly, organ doses can be measured using anthropomorphic physical phantoms. Both The Phantom Lab (RANDO® Phantoms) and CIRS Inc. (the ATOM® phantoms) produce tissue equivalent anthropomorphic (not tomographic) phantoms, but the documentation of anatomy, anatomical detail, and ability to accurately position (differing types of) dosimeters for the measurement of organ doses is not ideal or exact.³

Considering the reasoning above, a research project with the following specific aims was proposed.

- Beginning with a segmented full-body CT data set, develop a process for construction of an anthropomorphic tomographic adult male phantom that comprises soft tissue-equivalent substitute, bone tissue-equivalent substitute, lung tissue-equivalent substitute, and air. Develop a lung tissue-equivalent substitute.
- Construct an anthropomorphic tomographic adult male phantom and identify point dose locations representative of organ doses that can be integrated with an FOC dosimetry system.
- Perform and evaluate a dosimetric study for MDCT that illustrates the utility of anthropomorphic phantoms in CT dosimetry. Measure absorbed dose at organ locations and calculate effective dose.

- Examine overranging, overbeaming, and how the MDCT scanner (Siemens SOMATOM Sensation 16 helical) x-ray tube ramps up. Evaluate how these characteristics affect absorbed dose and effective dose.
- Compare organ dose measurements within the physical phantom with organ doses calculated using a computational phantom based on the identical tomographic data set.
- Consider expected dose distributions along the z-axis in MDCT that result from overbeaming and pitch. Investigate whether these distributions pose a problem for point dose measurements and whether or not these distributions could conceivably be used to reduce absorbed doses to radiosensitive tissues.

Background and Significance

Dosimetric Quantities

There are multiple types of dosimetric quantities typically used in CT. The most commonly used are weighted CT dose index ($CTDI_w$), volume CT dose index ($CTDI_{vol}$), dose length product (DLP), and effective dose.

CTDI measurements describe the average absorbed dose (mGy) within a scanned region. The head and body CTDI phantoms, shown in Figure 1-2, are two standardized polymethylmethacrylate (PMMA, e.g., acrylic or Lucite) cylinders, 14 cm in length, and diameters of 16 cm and 32 cm, respectively. Holes with 1 cm diameter are drilled at centers and 1 cm from outer edges at angles of 0° , 90° , 180° , and 270° in each phantom. $CTDI_w$ and $CTDI_{vol}$ depend on $CTDI_{100}$, which requires integration of the radiation dose profile from a single axial scan over limits of ± 50 mm. This can be measured using a commercially available, 100 mm pencil ionization chamber. $CTDI_{100}$ is defined by Equation 1-1.

$$CTDI_{100} = \frac{1}{nT} \int_{-50mm}^{+50mm} D(z) dz \quad (1-1)$$

Here, n is number of slices per scan, T is slice thickness, and $D(z)$ is dose as a function of position along the z -axis. $CTDI_w$ was developed because radiation dose varies with increasing depth. A 2/3 peripheral to 1/3 central weighting was selected, and is shown in Equation 1-2.

$$CTDI_w = (2/3)CTDI_{100peripheral} + (1/3)CTDI_{100center} \quad (1-2)$$

$CTDI_w$ reflects a weighted average dose within a single scan plane, but not dose along the z-axis in volumetric scanning. To account for gaps or overlaps between radiation dose profiles from consecutive gantry rotations (or in spiral or helical acquisition), the patient volume dose descriptor $CTDI_{vol}$ was created.

$$CTDI_{vol} = (nT / I)CTDI_w = CTDI_w / pitch \quad (1-3)$$

In spiral or helical CT, distance of table travel per rotation (I) to total beam width (nT) is pitch. $CTDI_{vol}$ indicates average absorbed dose to a point within a scan volume for a particular set of techniques in a standardized phantom. CTDI measurements are useful in understanding how adjusting techniques will adjust average absorbed dose, but CTDI does not represent accurately the average dose for an object with different size, shape, or attenuation.^{2, 11} The American College of Radiology (ACR) began a CT accreditation program in 2002. In part, the ACR CT accreditation requires that the $CTDI_w$ not exceed 60 mGy for the adult head protocol, 25 mGy for the pediatric abdomen protocol, and 35 mGy for the adult abdomen protocol.⁴

By definition, CTDI measurements do not indicate total energy deposited during a scan because they are independent of scan lengths. Dose length product (DLP) is a means to compare total energy absorbed from a specific scan acquisition against reference doses set for typical CT examinations. Equation 1-4 shows how DLP is calculated.

$$DLP(mGy \cdot cm) = CTDI_{vol}(mGy) \cdot scan_length(cm) \quad (1-4)$$

It is not a measure of patient dose for individual patients.^{2, 11}

CTDI and DLP measurements provide reasonable estimates of radiation dose, but it does not provide information on radiation risk. Effective dose (mSv) provides a risk-based dose from irradiation of human beings that is not homogeneous, as is the case with CT. Effective dose is a

calculated quantity that reflects the radiation detriment of a non-uniform exposure in terms of an equivalent whole body exposure. This allows non-uniform exposures such as those in CT to be compared with different sources of ionizing radiation, such as background radiation or radiation present in large epidemiological studies. Effective dose is defined in Equation 1-5.

$$E = \sum_T w_T H_T = \sum_T w_T \sum_R w_R D_{T,R} \quad (1-5)$$

Here, w_R is the radiation weighting factor (1 for photons), $D_{T,R}$ is the average absorbed dose to each tissue resulting from radiation type R, w_T is the tissue weighting factor for tissue T and $\sum w_T = 1$, summed over all tissues and organs considered sensitive to radiation. The w_T values in Table 1, taken from ICRP Publication 103, below were chosen based on the respective values of relative radiation detriment. The w_T for the remainder tissues apply to the arithmetic mean dose of those 13 organs and tissues, which is different from the treatment of remainder tissue in ICRP Publication 60.⁵

Effective dose (E) can be approximated using the relationship shown in Equation 1-6.

$$E = k \cdot DLP, \quad (1-6)$$

Here, k is an empirical weighting factor ($\text{mSv} \cdot \text{mGy}^{-1} \cdot \text{cm}^{-1}$) that is a function of body region.⁵

The ability to calculate effective doses from measured organ doses from CT scans permits estimates for excess risks of cancer due to radiation exposures received. Measuring organ doses in phantoms to calculate effective doses has been demonstrated by Hintenlang et al. and Chapple et al.^{15, 16}

Radiation Effects and Risks

There were an estimated 3 million CT scans in 1980; there are now an estimated 62 million scans per year in the United States. The increased exposure to the population due to CT could become a public health issue in the future. Two recent publications, BEIR VII (Biological

Effects of Ionizing Radiation) by the National Academy of Sciences and ICRP (International Commission on Radiological Protection) Publication 103, looked extensively at the latest biological and physical information in order to quantify risks due to low dose (defined as < 100mSv in both reports) radiation exposures (BEIR VII only considers low LET radiation).

Two types of risk are associated with radiation exposures, deterministic and stochastic. Deterministic effects (harmful tissue reactions) are largely due to the killing/malfunction of cells following high doses. A threshold dose exists for these risks, above which, the effect occurs, increasing in severity (e.g., skin erythema). Doses below the threshold result in no effect. Stochastic risks are those in which dose affects the probability of the effect occurring, not the severity (e.g., cancer).^{1,6,7} Deterministic effects are not really associated with CT and do not occur at doses less than 100 mSv.

Risks associated with radiation exposure is understood with respect to biological effects, but quantified primarily using direct human epidemiological data, and especially from studies of survivors of the atomic bombs dropped on Japan in 1945. Large cohorts of survivors have been studied for decades, and the statistical confidence improves as time passes. Approximately 25,000 survivors received radiation doses less than 50 mSv, doses similar to those received in CT. A recent large-scale study of 400,000 radiation workers with average doses of approximately 20 mSv supported estimates made using atomic bomb survivor (ABS) studies.^{1,8,9}

BEIR VII reconfirmed that the linear no threshold (LNT) model is the most practical model for radiation risks. Use of a dose and dose rate effectiveness factor (DDREF) of 1.5 is recommended; this means that chronic exposures are 1.5 times less carcinogenic than acute exposures. Table 2 below shows the attributable fraction of solid cancers in atomic bomb

survivors due to radiation exposure. Figure 1-3 illustrates the cancer mortality risk as a function of age and gender caused by a single radiation exposure of 0.1 Gy

The BEIR VII lifetime cancer mortality estimates are in good agreement with those of other scientific bodies (ICRP, EPA, UNSCEAR).^{2, 10} BEIR VII states that an effective dose of 10 mSv to a working age adult results in a 1 in 1000 lifetime risk of developing radiation induced cancer.⁷

ICRP Report 103 gives its risk coefficients in terms of detriment, or the total harm to health experienced by an exposed group and its descendants as a result of the group's exposure to a radiation source. Its principal components are the stochastic quantities: probability of attributable fatal cancer, weighted probability of attributable non-fatal cancer, weighted probability of severe heritable effects, and length of life lost if the harm occurs. Table 3 shows the most recent detriment adjusted risk coefficients after exposure to radiation at a low dose rate. Also shown are the previous ICRP risk coefficients (1990). The combined stochastic effects remain practically unchanged at roughly 5% per Sv.^{14, 21}

It is worth pointing out that ICRP Publication 103 recommends a DDREF of 2, as opposed to the BEIR VII recommended 1.5. Also of note is that ICRP Publication 103 lowered estimations for risks of serious heritable effects, and that this report lowered the tissue weighting factor for gonads while increasing the tissue weighting factor for breast.^{5, 11}

Using similar risk estimates and data on CT use from 1991 through 1996, it was estimated that 0.4% of all cancers in the United States could be attributable to radiation from CT studies. Adjusting for the increase in CT use, this estimate could be in the range of 1.5 to 2.0%.¹ Table 4 shows the estimated effective radiation dose for common diagnostic imaging tests. Figure 1-4 shows the estimated dependence of lifetime radiation induced risk of cancer vs. age at

exposure for two common radiogenic cancers. The average adult CT scan receives a radiation dose in the range of 15 mSv, with an average of two to three CT scans per study.¹ Mettler et al. reported that among all patients undergoing CT, at least three scans were obtained in 30% of patients, more than five in 7%, and more than eight in 4% of patients.¹² These references directly relate average CT dose to magnitudes of doses found in the ABS and large-scale radiation worker studies. Therefore, risks due to CT are statistically significant and do not have to be extrapolated. Risks at these dose levels are likely, with dose and risk increasing simultaneously. And so, improvements in CT dosimetry provide more accurate and reliable information to those attempting to decrease effective dose to patients.

Dosimeters

The most frequently used dosimeters in diagnostic dosimetry include ionization chambers, thermoluminescent dosimeters (TLDs), metal-oxide semiconducting field effect transistors (MOSFETs), diodes, optically-stimulated luminescence (OSL), and more recently, scintillation phosphors coupled with optical fiber. In diagnostic dosimetry, especially for in-phantom measurements, an ideal dosimeter should have the following characteristics: similar effective atomic number to that of soft tissue (7.4), uniform energy response, linear response to mAs, high sensitivity, excellent reproducibility, response independent of orientation, small size, *in situ* readability, real-time readings, possibility of simultaneous measurements, and low cost. Table 1-5 compares common dosimetry systems with these desirable characteristics.

The ionization chamber is mainly used for various CTDI and DLP measurements. It is very reliable in that it has excellent linearity, is very sensitive, has a uniform energy response, and shows little fading. Ionization chambers must be sent away to be calibrated and are relatively expensive. They are fairly large and are therefore not very suitable for making simultaneous in-phantom measurements.

The most common in-phantom dosimeter for diagnostic radiology dosimetry is the TLD. Its small size allows many TLDs to be placed within a phantom, and therefore measurements at multiple locations can be taken simultaneously. The effective atomic numbers found in LiF-based TLDs are a reasonably close match to those of soft tissue, which improves their ability to represent absorbed dose in soft tissue. Within a specified energy range, highly sensitive TLDs can be found that have a uniform, linear, and reproducible response. Unfortunately, TLDs have some inconvenient qualities. They must be annealed prior to each use, and reading must be performed relatively soon after exposure in a TLD reader, both of which are time consuming processes. Hohl et al. evaluated CT fluoroscopy and the effect of angular beam modulation in a 64-section MDCT. They measured organ dose and effective dose in a female RANDO® phantom using LiF:MgTi (TLD-100).¹³⁻¹⁵

Kawaura et al. placed multiple photodiode dosimeters in an anthropomorphic phantom to measure organ and effective doses in real time for CT examinations.¹⁶ Diodes are relatively inexpensive, sensitive, and can provide real-time measurements. Two major disadvantages with diode dosimeters is that they have a non uniform angular response, and their response is not uniform with energy.¹⁷

The use of optically stimulated luminescence (OSL) in $\text{Al}_2\text{O}_3\text{:C}$ is similar to that of TLDs, except that OSLs are read using light instead of heat. OSLs are linear over a wide range of dose values and tube current. An advantage OSLs have over TLDs is that they may be coupled to optic fibers, and using pulsed laser light, can be read in real-time to give point dose values. The main problem with OSL diagnostic dosimetry is that their effective atomic number of 11.28 is significantly greater than that of tissue equivalent (7.4)¹⁸ Because of this, OSL dosimeters over respond to low energy x-rays.¹⁹

The MOSFET dosimeter has a number of useful characteristics: excellent linearity, reproducibility, and suitability for measuring organ doses within a phantom real-time. However, as with many diagnostic dosimeters, the main problem lies with a non-uniform response for different energies, a higher effective atomic number than human tissue, and a significant angular dependence.²⁰ Yoshizumi et al. compared organ dose assessment in an anthropomorphic phantom during CT measured using MOSFETs with those measured using TLDs. Hurwitz et al. used a MOSFET dosimetry system to measure organ dose and to calculate effective dose for various adult MDCT protocols. In both studies, energy calibrations were performed free in air, which apparently neglects changes in the energy spectrum within the phantom.²¹⁻²³ There are also some issues with non-uniformity with respect to dosimeter orientation.^{24, 25}

The use of scintillation materials to detect radiation is one of the oldest methods on record. More recently, scintillators have been used to provide point dose measurements in radiation fields. Scintillation phosphors are coupled to optical fibers, which transmit radiation induced emitted light away from the radiation field, where it is then measured, usually by a photo-multiplier tube (PMT) or charged coupled device (CCD). Real-time measurements can be performed with a fiber-optic coupled (FOC) dosimeter using a scintillation phosphor. Scintillators should show little angular dependence. Generally, inorganic scintillators have better light output and linearity than organic ones. Unfortunately, inorganic scintillators typically have a much higher effective atomic number than human tissue, and non-linear energy dependences (due in part to K-edge absorption) within the diagnostic energy range. Organic scintillators, on the other hand, can be dissolved in a solvent and subsequently polymerized, resulting in scintillating materials with effective atomic numbers closer to those of soft tissue. Therefore, energy absorbed within an organic scintillating material should be closer to the amount of energy

absorbed by human tissue. Plastic scintillators designed with effective atomic numbers similar to human tissue, as well as with attenuation behavior similar to water are available. One concern with scintillators is that they can degrade over time with accumulated exposure.⁵

Very few studies have been performed using FOC scintillation phosphors on diagnostic energies. Moloney constructed a Gd based FOC dosimetry system that showed little angular dependence in-phantom, was highly reproducible, and provided real-time measurements, but over-responded to low energy photons.²⁶ Lacroix et al. constructed a scintillating fiber dosimeter array using 1 mm plastic scintillation detectors (BCF-12), optical fibers, and a CCD. They designed and tested their array considering therapeutic energy levels.⁸ Villagresa et al. have begun developing a prototype plastic scintillation detector and anthropomorphic phantom instrument that will measure, in real-time, effective dose due to low-dose rates found at workplaces.²⁷ Jones et al. evaluated an FOC dosimeter based on the phosphorescence of a Cu^{1+} -doped quartz fiber. This detector system displayed high sensitivity, tissue equivalence, minimal angular response, and excellent dose linearity. However, it had a positive energy dependence, and reproducibility was a concern.²⁸

More recently, a water-equivalent plastic scintillator FOC dosimetry system prototype was constructed at the University of Florida. Figure 1-5 contains a schematic of this system. This system collects scintillation photons using a photomultiplier tube (PMT), which converts the photon count into a proportional voltage signal. This voltage is relayed in terms of photon counts to a PC. A custom MATLAB program records incoming counts, providing real-time dosimetry measurements. This dosimeter demonstrates high sensitivity, excellent dose linearity, excellent reproducibility, and is suitable for in-phantom measurements. Most importantly, this dosimetry system does not over-respond to low energy photons. Figure 1-6 shows normalized

sensitivity of the FOC dosimeter as a function of depth in soft tissue-equivalent material. The main disadvantage of this system is cost. Each scintillating fiber/reference fiber combination requires two PMTs, which currently cost about \$3000 each. Therefore, this experimental dosimetry system currently has only two channels.

Strategies for Reducing Patient Dose in CT

In most cases, CT scans are associated with a very favorable benefit to risk ratio. In CT, there are no penalties in image quality for increasing patient dose, but as the previous section emphasized, there are risks related to the absorbed doses due to CT radiation exposure. CT image quality and associated patient doses should be just sufficient to ascertain diagnoses. However, reducing image quality to a point where images become useless, resulting in repeated scans, must be avoided. The “as low as reasonably achievable” (ALARA) principle should be followed. A recent straw poll of pediatric radiologists suggested that 1/3 of CT studies could be eliminated. A survey of radiologists and emergency room physicians revealed that 75% of those questioned significantly underestimated the radiation dose from a CT scan. Additionally, 53% of radiologists and 91% of physicians do not believe that CT scans increase the lifetime risk of cancer. A favorable benefit to risk ratio is good, but an improved ratio is even better, and so strategies to reduce patient dose in CT should be followed.¹ This is being addressed for children with the “Image Gently Campaign” (www.imagegently.org), whose goal is to raise awareness about the opportunities to decrease imaging radiation doses in children.

There are many ways to decrease dose to patients and/or the population. First, besides simply prescribing fewer CT exams, CT exams should be replaced with alternate procedures such as MRI and ultrasonography. For example, appendicitis can be successfully diagnosed using ultrasonography instead of CT.^{1,7} All protocols should be reviewed to see if technique settings can be adjusted to reduce dose. Dose is proportional to mAs, and inversely proportional

to slice thickness. For human soft tissue and fat, lowering kVp will lower dose and raise contrast, but will reduce the contrast to noise ratio (CNR).^{17, 39} However, kVp can be lowered in order to reduce radiation doses to patients for studies that use iodinated contrast media.²⁹ Typical doses for CT procedures should be displayed prominently to allow physicians and radiologists to become more aware of higher-dose procedures. Dose information should be recorded with every patient's permanent file. The scan volume should be limited to the volume needed and critical organs should be shielded when possible. Unnecessarily repeated CT scans should be avoided, and CT scans should not be used in practice of defensive medicine. Radiologists and CT operators should understand that a decrease in patient size permits a decrease in dose.^{2, 3} There has been increasing information about the feasibility of low-dose lung cancer screening and CT colonography. If possible, images should be acquired only during contrast phases if clinically needed.³⁰ Ask whether follow-up diagnostic radiologic studies are necessary; increase follow-up intervals for regular examinations.⁷ Radiologists should communicate more with physicians instead of simply performing the study requested. CT scans can be designed to answer specific questions and follow up studies do not have to be full (e.g., only over a lesion). Changing gantry rotation angles and using bismuth shields to avoid/protect particularly radiosensitive sensitive organs has been reported to lower dose significantly in some instances, but this also results in additional noise and artifacts near the shields.^{29, 31, 32} Automatic tube current modulation (ATCM) has been one of the most useful tools in decreasing patient dose. With ATCM, tube current is adjusted based on thickness, cross sectional geometry, and/or intrinsic density of structures and tissues in order to maintain a constant level of image noise; image noise is proportional to the inverse of the square root of dose. Effective dose due to computed tomography cardiac imaging (cardiac volumetric cine imaging) was found to decrease

significantly using a 256-multislice CT (MSCT) scanner, as opposed to using a 16 and 64-MSCT in helical mode with electrocardiographic (ECG) gating.^{29, 33} Finally, detector efficiency and filtering algorithms can also be improved upon.^{29, 34, 35}

Patient Simulation in CT

Patient simulation in CT is mostly limited to the CTDI phantoms described earlier, computational phantoms/Monte Carlo simulation, and physical anthropomorphic phantoms. Physical phantom studies have an advantage over Monte Carlo studies in that no knowledge of the photon spectrum or irradiation geometry is required. Also, modeling CT is becoming increasingly difficult with increased use of proprietary scanning techniques such as automatic tube current modulation. Two disadvantages of physical phantom studies versus Monte Carlo studies is that dose measurements are typically made in small localized volumes and physical dosimeters are imperfect. Taking dose measurements in small localized volumes and using them as representative of the dose in a larger region ignores dose distributions present within the phantom. The main problem with dosimeters used in phantom studies is their non-uniform energy responses.

There are several attributes that are desirable in anthropomorphic phantoms. They are as follows: tissue-equivalence, durability, anatomical accuracy, include a method for integrating dosimetry, include a computational “twin” phantom, have a relatively low material cost. The tissue-equivalent materials primarily used represent soft tissue, bone tissue, and lung tissue. Besides commonly used acrylic, water, and air, more exact tissue equivalent materials are used. An extensive set of tissue equivalent materials has been developed by White.³⁶⁻³⁹ ICRU Report 44 contains detailed tabulations of the elemental compositions and physical characteristics of a variety of tissue substitutes.⁴⁰ Tissue-equivalent materials have also been developed at the University of Florida for soft tissue, bone, and lung, for both newborn and adult. Two

commonly used commercially produced phantoms are the CIRS ATOM® phantom series which comprise a 1, 5, 10 year old, and adult male and female phantoms, and The Phantom Laboratory's RANDO®Man and RANDO®Woman. Both of these phantoms use precisely designed tissue equivalent materials in an anatomically based anthropomorphic phantom. RANDO® used to include human skeletal bone, but has recently switched to a bone tissue substitute. These phantoms are typically made up of 25 mm sections that contain hole/plug locations for placement of TLDs. Neither phantom has a corresponding computational model, and both are relatively expensive (\$10,000-\$20,000+). The CIRS ATOM® phantom series has a map of organ locations, but traceability is not well documented. The RANDO® phantoms are loosely based on anthropometry numbers taken from a 1950's U.S. Air Force survey. The CIRS ATOM® phantom series and the RANDO® phantom are pictured in Figure 1-7.⁴¹

The UF phantom series has been constructed using both epoxy resin based and polyurethane elastomer based tissue-equivalent materials developed at the University of Florida. This series includes an MIRD, newborn, and 1 year old phantom, which can be viewed in Figure 1-8. These phantoms each have a computational "twin" phantom. The tomographic phantoms are based on segmented CT data sets and are constructed in 5 mm slices. Because they are developed using a CT data set, the exact organ locations are known.

Image Quality Assessment in CT

The American College of Radiology (ACR) began a CT accreditation program in 2002. This accreditation program is intended to evaluate image quality of CT. Understanding this accreditation process helps to illustrate concepts of interest in CT image quality. Selecting CT technique factors is a balancing act between improved image quality and increased patient dose.

The ACR accreditation phantom (model 464, Gammex-RMI, Middleton, WI) was designed to examine the following image quality parameters: positioning accuracy, CT number

accuracy, slice width, low contrast resolution, high contrast (spatial) resolution, CT number uniformity, image noise. The phantom has four modules made from a water equivalent material, and is 4 cm in depth and 20 cm in diameter each. Figure 1-9 shows a cross-sectional diagram of each module.

The first module is used to evaluate phantom positioning and has cylindrical rods for assessing the CT number of different materials (water, air, polyethylene, acrylic, bone, and air). It is also used to measure slice thickness. The second module tests low-contrast spatial resolution with different sized sets of cylindrical rods whose CT number differs from the background material by 6 HU. The third module is used to measure image uniformity. Average CT numbers from peripheral regions of interest (ROI) are compared against the average CT number from a ROI at the center. The fourth module tests high contrast (spatial) resolution with eight different spatial frequency bar patterns.

A more complete description of the spatial resolution of an imaging system, although less convenient for quality assurance purposes, is the modulation transfer function (MTF). MTF reflects the fraction of an object's contrast that is recorded, as a function of image size. The MTF can be obtained by taking the Fourier transform (FT) of the line spread function (LSF), which describes the system's response to a linear stimulus. In CT, LSF can be obtained by imaging a very thin sheet of contrasting material. Alternatively, the edge spread function (ESF) describes the system response to a sharp edge. ESF can be differentiated to obtain the LSF, which is then transformed into the frequency domain via FT to obtain MTF. Figure 1-10 shows a measured ESF, differentiated LSF, and the resulting MTF.⁴²⁻⁴⁴

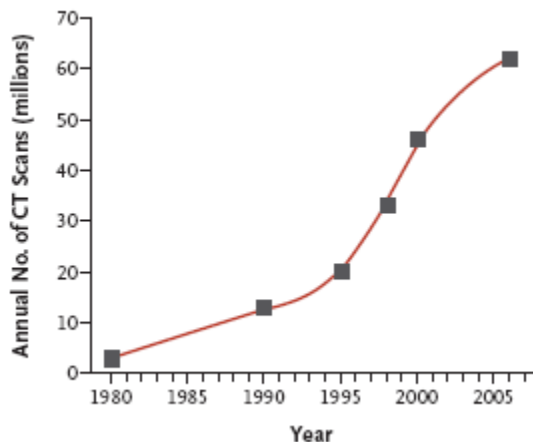


Figure 1-1. Estimated number of CT scans performed annually in the United States (D. J. Brenner and E. J. Hall, *N Engl J Med* **357** (22), 2277-2284 (2007), Figure 2, p. 2280).

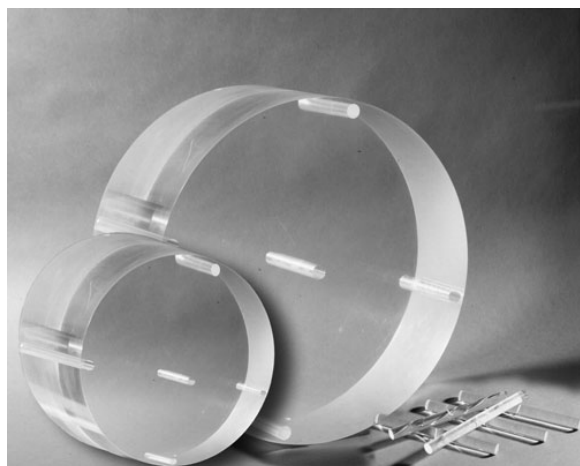


Figure 1-2. The head and body CTDI phantoms.

Table 1-1. Recommended tissue weighting factors⁵

Tissue	w_T	$\sum w_T$
Bone-marrow (red), Colon, Lung, Stomach, Breast, Remainder tissue*	0.12	0.72
Gonads	0.08	0.08
Bladder, Esophagus, Liver, Thyroid	0.04	0.16
Bone surface, Brain, Salivary glands, Skin	0.01	0.04
Total		1.00

*Remainder tissues: Adrenals, Extrathoracic (ET) region, Gall bladder, Heart, Kidneys, Lymphatic nodes, Muscle, Oral mucosa, Pancreas, Prostate, Small intestine, Spleen, Thymus, Uterus/cervix.

Table 1-2. Solid cancer cases by dose category²

Dose Category*	Subjects	Observed	Expected	Observed-Expected	Attributable Fraction (%)
<0.005	60,792	9597	9537	3	0.0
0.005 to 0.1	27,789	4406	4374	81	1.8
0.1 to 0.2	5527	968	910	75	7.6
0.2 to 0.5	5935	1144	963	179	15.7
0.5 to 1	3173	688	493	206	29.5
1 to 2	1647	460	249	196	44.2
2 to 4	564	185	71	111	61.0
Total	105,427	17,448	16,595	853	10.7

*Weighted colon dose in Gy.

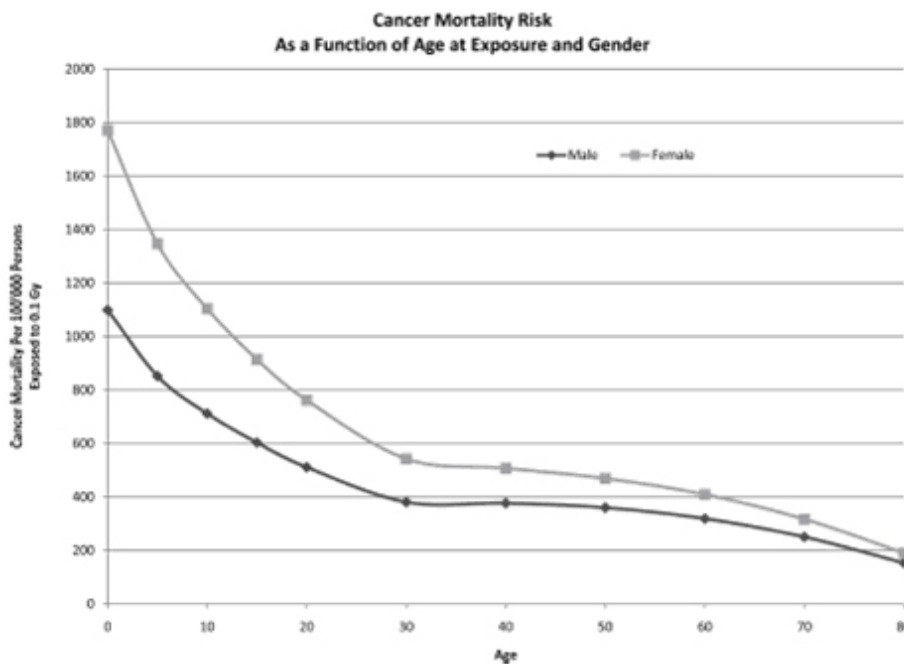


Figure 1-3. Number of excess cancer deaths caused by a single radiation exposure of 0.1 Gy as a function of age at the time of exposure and gender (H. D. Royal, Semin Nucl Med **38** (5), 392-402 (2008), Figure 4, p. 400).

Table 1-3. Detriment adjusted nominal risk coefficients for stochastic effects after exposure to radiation at low dose rate (10-2 Sv-1)¹¹

Exposed population	Cancer		Heritable effects		Total detriment	
	2007	1990	2007	1990	2007	1990
Whole	5.5	6.0	0.2	1.3	5.7	7.3
Adult	4.1	4.8	0.1	0.8	4.2	5.6

Table 1-4. Estimated effective radiation dose for common diagnostic imaging tests (D. Lockwood, J Radiol Nursing **26**, 121-124 (2007), Table 1, p 122).

Study	Effective Dose in Millisieverts [†]
Chest radiography, posteroanterior and lateral	0.06
Screening mammography	0.6
Gastric emptying study	1.4
Kidney-ureter-bladder radiography	1.7
CT of the head	1.8
Lumbar spine radiography	2.1
Background radiation, annual dose	3.6
Radionuclide bone scan	4.4
Ventilation-perfusion (V/Q) scan	6.8
CT of the pelvis	7.1
CT of the abdomen	7.6
CT of the chest	7.8
Barium enema radiography	8.7
CT angiography of coronary arteries	10
Positron emission tomography, whole body	14
Small bowel series (barium swallow x-ray study)	15
Intravenous pyelography	10.0-20.0
Whole-body screening CT	22.5
Three-phase hepatic CT scan	29.9
Dual-isotope myocardial rest and stress perfusion CT study	32.5
CT urographic study	44.1

*All values are for procedures performed at the Cleveland Clinic.

[†]10 mSv (millisieverts) = 1 rem.

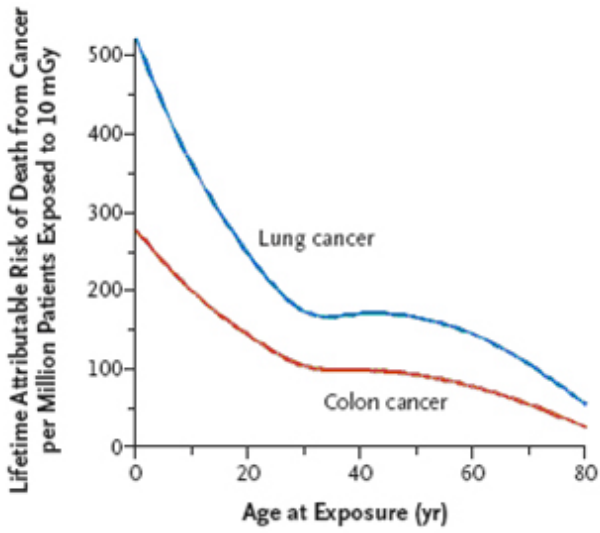


Figure 1-4. Estimated dependence of lifetime radiation induced risk of cancer vs. age at exposure for two common radiogenic cancers (D. J. Brenner and E. J. Hall, *N Engl J Med* **357** (22), 2277-2284 (2007), Figure 4, p. 2282)

Table 1-5. Comparison of dosimetry systems with desirable characteristics for diagnostic dosimetry.

	Ionization Chamber	TLDs	MOSFETs	(Photo)diodes	OSLs	Scintillation Phosphors
Effective Z Similar to Soft Tissue (7.4)		Fair	Poor		Poor	Good
Uniform Energy Response	Good	Fair	Poor	Poor	Poor	Fair
Linear Response with mAs	Good	Good	Good		Good	Good
Sensitivity	Good	Good		Good		Good
Reproducibility	Good		Good			Good
Little Angular Dependence	Possible	Possible	Poor	Poor	Possible	Possible
Small Size	Poor	Good	Good	Good	Good	Good
Readings <i>in situ</i>	Yes	No		Yes	Possible	Yes
Real-Time Measurements	Possible	No	Yes	Yes	Possible	Yes
Simultaneous Measurements	No	Yes	Yes	Yes	Yes	Yes

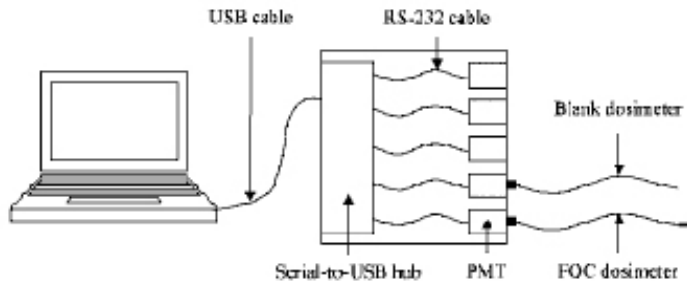


Figure 1-5. Schematic of UF plastic scintillator FOC dosimetry system.

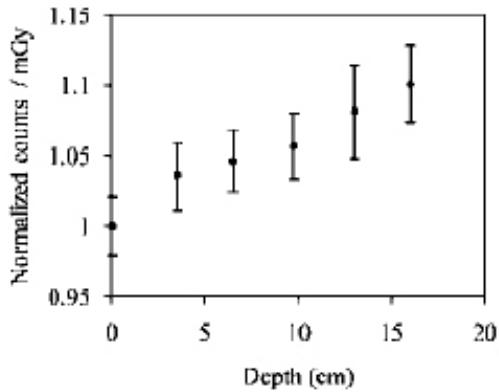


Figure 1-6. Normalized sensitivity of the FOC dosimeter, as a function of depth in soft tissue-equivalent material.

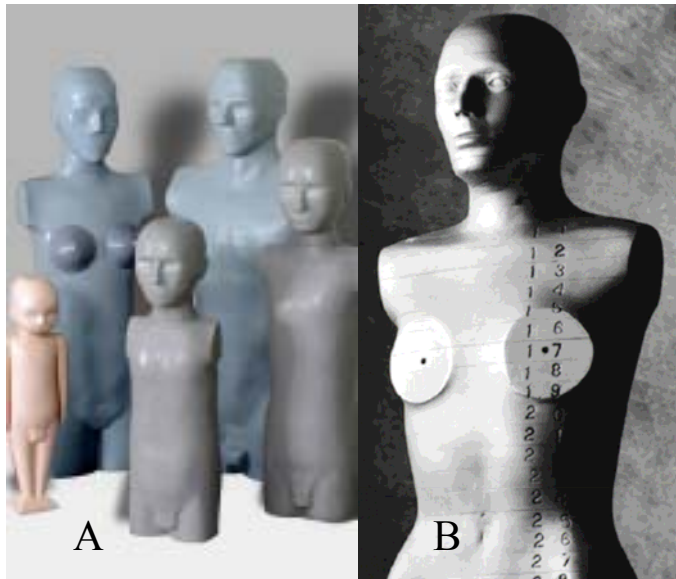


Figure 1-7. Commercially available phantoms. A) The CIRS ATOM® phantom series. B) The RANDO® phantom.

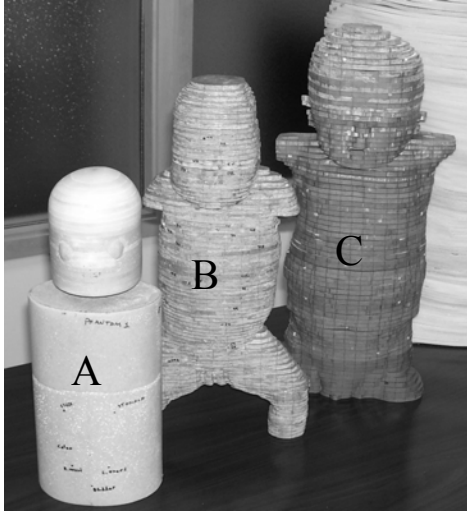


Figure 1-8. The UF pediatric phantom series. A) MIRD phantom. B) Newborn Phantom. C) 1 year old phantom.

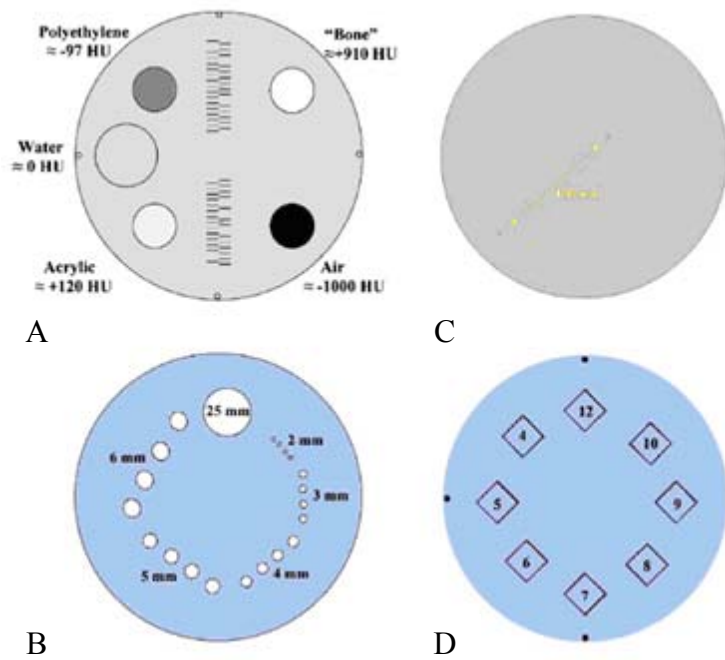


Figure 1-9. Cross-sectional diagrams of the ACR accreditation phantom nodules. A) Nodule 1 examines CT number and slice width accuracy. B) Nodule 2 examines low-contrast resolution. C) Nodule 3 is used to assess image uniformity. D) Nodule 4 examines high-contrast (spatial) resolution (C. H. McCollough, M. R. Bruesewitz, M. F. McNitt-Gray, K. Bush, T. Ruckdeschel, J. T. Payne, J. A. Brink and R. K. Zeman, *Med Phys* **31** (9), 2423-2442 (2004), Figure 13, p. 2441).

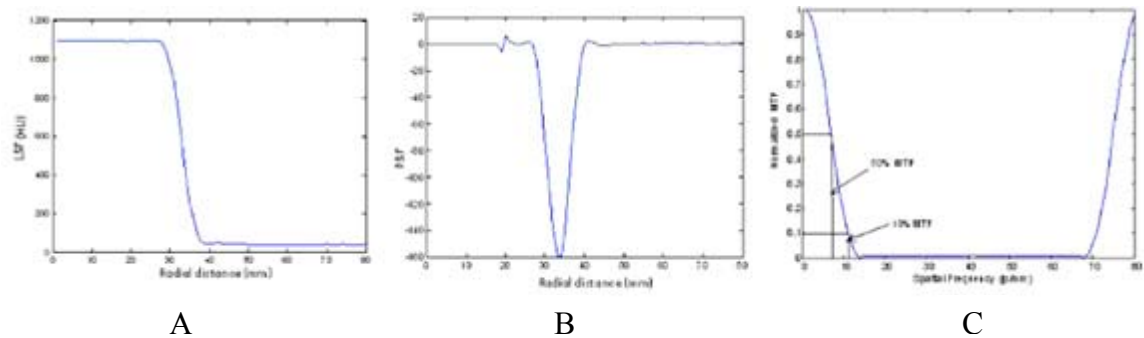


Figure 1-10. Measured ESF, LSF, and MTF. A) The resulting ESF along a spherical surface derived from phantom data. B) The LSF computed from the ESF. C) The derived MTF (B. Li, G. B. Avinash and J. Hsieh, *Med Phys* 34 (10), 3732-3738 (2007), Figure 7, p. 3735).44

CHAPTER 2 CONSTRUCTION OF ANTHROPOMORPHIC PHANTOMS FOR USE IN DOSIMETRY STUDIES

Introduction

Anthropomorphic phantoms constructed from tissue-equivalent materials have historically been used to provide a physical representation of the body's anatomy and attenuation characteristics for radiation dosimetry studies. Of particular interest here is use of anthropomorphic phantoms for measuring dose in diagnostic imaging procedures, where such measurements have been used by several authors to calculate average organ doses as well as effective doses in computed tomography (CT), cone-beam CT, and pediatric radiology.^{21, 45, 46} Quantifying organ doses in physical phantoms offers a distinct advantage over computational methods because knowledge of the exact photon energy spectrum or irradiation geometry is not required. This is especially useful considering increasing use of proprietary scanning techniques that are difficult to model, such as automatic tube current modulation in CT and automatic exposure control (AEC) in fluoroscopy. The majority of organ dose studies in diagnostic imaging utilize commercially available anthropomorphic phantoms such as RANDO® (The Phantom Laboratory, Salem, NY) or ATOM® phantoms (Computerized Imaging Reference Systems, Inc, Norfolk, VA). In order to provide a representation of the human anatomy, these commercially available phantoms typically use three tissue equivalent materials imitating bone, lung, and soft tissue. To allow access to organ locations for the placement of dosimeters, the RANDO® and ATOM® phantoms are assembled in axial slices 2.5 cm thick. Unfortunately, widespread clinical use of these phantoms has been limited by cost.

A series of low-cost tissue equivalent materials that are easily prepared in the laboratory was recently developed at the University of Florida (UF). These materials have been incorporated into several sophisticated anthropomorphic phantoms. To date, this process has

been used to create a series of three adult phantoms. Expanding upon methods originally published by White et al.,^{36, 39} and later improved upon by Jones et al.,⁴⁷ three tissue-equivalent materials were developed for use in phantom construction: soft tissue-equivalent substitute (STES), lung tissue-equivalent substitute (LTES), and bone tissue-equivalent substitute (BTES). BTES is based on an epoxy resin which forms a hard thermoset polymer, as previously described by Jones et al.⁴⁷ STES and LTES are based on a new urethane mixture which forms a pliable compound. This material was chosen in part for ease in phantom construction, improved phantom durability, and easier accommodation of real-time dosimeters.

Advantages of the UF phantoms compared to commercially available phantoms is that they utilize a 5 mm slice thickness, allowing greater options for dosimeter placement when performing internal dose measurements. Also, phantom anatomy is precisely known with respect to the CT data set used to construct the phantom. Each physical phantom has a corresponding segmented computational phantom that was created from the same original CT data set, such as those developed by Lee et al.⁴⁸ This allows the physical phantom to serve as a direct comparison to the computational phantom for the experimental validation of Monte Carlo codes. In turn, the computational phantom can be used to determine point-to-organ dose scaling factors, allowing the calculation of average organ doses from simple point organ dose measurements made in the physical phantom.⁴⁹

The full-body data set includes over three-hundred axial slices; however, lack of radiosensitive organs in the legs justified their exclusion from fabrication. As such, each phantom includes approximately two-hundred axial slices, ranging from the crown of the head to mid-thigh. All internal organs in the phantoms are modeled as soft tissue and therefore dosimeter placement for organ dose measurements is based solely on position of the segmented

organs in the original data set. To aid in dosimeter placement, organ locations have been transferred onto each slice from full-scale printouts of the original segmented data set.

Methods

Materials

The tissue-equivalent substitutes used for this undertaking were developed with two goals in mind: 1. Similar physical properties to human tissue, such as density and attenuation coefficients, and 2. Ease of integration into the phantom manufacturing process. To meet these goals, new urethane based STES and LTES were developed.

Tissue-equivalent materials were evaluated by measuring material density and attenuation properties. Attenuation coefficient of STES was evaluated by measuring attenuation from multiple thicknesses using a narrow beam geometry generated by clinical radiographic unit. Additionally, Hounsfield Unit (HU) values were measured in the completed phantom using a Siemens SOMATOM Sensation 16 helical MDCT scanner operated at a tube voltage of 120 kVp and employing an mA modulated exposure control. Average HU was determined from the selected regions of interest (ROI) using areas of approximately 10 cm².

Density measurements of each sample were then taken utilizing Archimedes's principle. A cured sample of each material was weighed on a scale with 0.001 gram precision to find the dry mass, m_{dry} , of each sample. Samples were then weighed submerged in a beaker of de-ionized water to find the wet mass, m_{wet} , of each sample. Using both these measurements, as well as the known density of the de-ionized water, ρ_{H_2O} , the density of each sample was calculated using Equation 2-1.

$$\rho_{sample} = \frac{m_{dry}}{\left[\frac{m_{dry} - m_{wet}}{\rho_{H_2O}} \right]} \quad (2-1)$$

Soft tissue-equivalent substitute (STES)

A new urethane based STES was designed to match the x-ray attenuation and density of human soft tissue within the diagnostic energy range (80-120 kVp). Specifically, the STES was designed to have a density similar to that of human soft tissue (1.04 g/cm³) and to achieve a target x-ray attenuation coefficient based on the ICRU-44 reference soft tissue composition.^{49, 50} The commercially available, two part urethane rubber compound “PMC 121/30 Dry”, (Smooth-On, Easton, PA), was combined with 2.8% by weight of powdered CaCO₃ (Fisher Scientific, Hanover Park, IL) to achieve these design goals. Calcium carbonate was added to two parts of urethane and mixed with an electric mixer to ensure homogeneity with totally dissolved CaCO₃. The durable, readily available urethane based compound was found to be easy to work with and did not suffer from phase separation problems frequently encountered with epoxy resin based STES. An additional benefit of the urethane based STES is its flexibility, which allows easy removal from molds after curing.

Adipose tissue was not specifically modeled in the construction of the anthropomorphic phantom. The distribution of subcutaneous as well as intra-abdominal adipose tissue was initially determined to be too complicated to directly model with a specific tissue equivalent material. Thus, the STES was developed to be a homogeneous soft tissue analog that comprises skeletal muscle as well as organs, connective tissue and adipose tissue.

Lung tissue-equivalent substitute (LTES)

A new LTES was designed by combining uncured urethane based STES, prepared as described above, along with poly-fil® polystyrene micro beads (Fairfield Processing, Danbury,

CT) in a 10:1 ratio by weight. This LTES is very uniform and permits fabrication of a range of tissue densities spanning those representative of various levels of inspiration. Since it does not rely on a tissue surfactant and foaming agent, the LTES is more uniform and reproducible than the method proposed by White et al.³⁸ While the density of lung tissue can vary widely depending on the level of inspiration, patients undergoing diagnostic procedures are typically asked to hold their breath during the exposure. Therefore, a value of 0.33 g/cm³ was chosen for the LTES, representing the density of a fully inspired lung.⁴⁹

Bone tissue-equivalent substitute (BTES)

Bone tissue-equivalent substitute (BTES) used was the epoxy resin based material previously developed by Jones et al.⁴⁷ By mass, mixture of BTES was as follows: 36.4% Araldite GY6010 and 14.6% Jeffamine T-403 (Huntsman Corp., Woodlands, TX), as well as 25.5% Silicon dioxide and 23.5% Calcium carbonate (Fisher Scientific, Hanover Park, IL). It was designed to represent a homogenous mixture of cortical and trabecular spongiosa (bone trabeculae and bone marrow). BTES composition was adjusted to match mass density, mass attenuation coefficients (μ/ρ), and mass energy absorption coefficients (μ_{en}/ρ) for those defined by the Oak Ridge National Laboratory (ORNL) stylized model series⁵¹ within the diagnostic photon energy range. The effective atomic number for the BTES (8.80) is very similar to that of the ORNL reference tissue (8.59), and it was shown that values of μ/ρ and μ_{en}/ρ for BTES had a maximum deviation from ORNL reference values of only a few percent.⁴⁷

Phantom Construction Methodology

Initially, the methodology described by Jones et al.⁵² in construction of a newborn phantom was to be used in construction of the adult phantom series. This method involved several steps including preparing epoxy based soft tissue material in a vacuum chamber to eliminate air bubbles, pouring the material into a square mold, milling out the outer slice contour as well as

appropriate voids for bone and lung tissue-equivalent material, and finally filling these voids with bone or lung tissue-equivalent material as required. However, the far greater number and size of slices required to construct an adult phantom, as compared to a newborn phantom, required many changes in the original construction methodology. Construction of the first adult phantom began with a segmented CT data set and an automated machining system and software (VisionPro Version 7, Vision Engraving and Routing Systems, Phoenix AZ) which was intended to speed up the phantom construction process. Once the phantom construction was initiated, problems were identified and overcome as they arose. The final means of production are detailed below.

Using segmented tomographic images with the engraving system

Three different adult phantoms have been constructed to date. The first phantom “GatorMan” was based on a 35 year old Korean adult male, 172 cm in height and 68 kg in total body weight.⁴⁸ The exam was performed in conjunction with a cancer screening protocol using a Siemens SOMATOM Emotion Duo PET/CT system with a slice resolution of 1mm. The next two phantoms constructed were based on hybrid computational phantoms of a 50th percentile adult male and female developed at the University of Florida. These phantoms originated from tomographic data, but were subsequently modified to match anthropometric dimensions and organ masses as defined by the International Commission on Radiological Protection (ICRP) publication 89⁶⁰ reference data for a 50th percentile human in a process similar to that described by Lee et al.^{53, 54} The original tomographic data for each hybrid phantom came from a 36 year old Korean adult male (176 cm height, 73 kg weight) and 25 year old adult female (163 cm height, 60 kg weight). The adult male exam was performed as part of a cancer screening protocol using a Siemens SOMATOM Emotion Duo PET/CT system with a slice resolution of 3mm. The

adult female was performed with a 4.5 mm slice resolution. All scans were performed at full inspiration with an in-plane matrix size of 512x512 pixels. Organ segmentation was performed manually under supervision of a radiologist. While approximately 100 different tissues were segmented in the computational data set, only the organs needed for the calculation of effective dose, as outlined in ICRP 103,⁵ were transferred to the physical phantoms.

The first step in constructing the phantom was to convert the segmented data set into a form that could ultimately be read with the automated machining software. Using ImageJ software (Version 1.34s, National Institute of Health, Bethesda, MD), each segmented image was converted into a bitmap representing only soft tissue and other tissues (bone, lung, air). This was accomplished by segmenting bone, lung, and air to a single pixel value representing “voids,” while all remaining soft tissues were shaded with another single value representing soft tissue. Registration marks for assisting in phantom assembly and alignment were also added to each bitmap image and the finished bitmaps were then imported into the VisionPro software. Each bitmap was adjusted to conform to the 256 value color range in the VisionPro software and vectorized in order to smooth the pixilated edges of the digital images. A speckle filter was used to eliminate tissue islands less than four pixels in area. Once these steps were complete, engraving paths for all areas represented by the soft tissue pixel value were then created for each slice. Realizing that smaller diameter “end mill” bits allow finer details to be cut, a 1/8” diameter bit was selected for body engraving paths while a 1/16” diameter bit was chosen for engraving paths in more detailed regions of the head.

The engraving paths were used to mill soft tissue molds in a high density foam, which could then be filled with the soft tissue substitute. Foam blanks were fastened to the engraving table and single-pass engraving paths were set with depths resulting in 5 mm thick soft tissue

slices. To create clean edges in each foam mold, a perimeter engraving path was first performed at a slow feed (0.6” per second), outlining the entire perimeter of the area to be cut. This was followed by a much faster rate fill engraving path (3” per second), which removed all foam material within the perimeter engraving path. Molds for each slice could be created in approximately ten minutes. The process of manufacturing a soft tissue mold is shown in Figure 2-1.

After engraving was completed, the molds were checked to ensure that all areas to be filled with STES were connected to aid in future placement. In cases where an area to be filled with STES was surrounded by bone or lung, small grooves were cut in the mold with a razor blade in order to connect the soft tissue island to the main body of the slice. This is similar to a stencil where the center of the letter “O” must be joined with thin connectors to ensure proper orientation. Finally, the job time for each slice was recorded. The job time and feed rate was used to determine the approximate volume/weight of soft tissue equivalent material needed for each slice.

Fabrication of soft tissue

Depending on how many soft tissue molds were being filled at a time, an appropriate amount of the urethane based STES was mixed and immediately poured into the soft tissue molds. This was done fairly rapidly (less than 30 minutes) as the STES began setting immediately. The filled molds were covered with waxed paper and any trapped air pockets were relieved by slicing the waxed paper with a razor blade. The molds were then covered with smooth, weighted boards in order to force excess STES out of the molds, which would allow the soft tissue slices to cure at the correct thickness (5 mm). After roughly three hours, the weight and waxed paper was removed from the partially cured soft tissue slices. It is important to

remove the waxed paper prior to the STES fully curing in order to facilitate removal. After 24 hours, the soft tissue slice could be removed from the mold and any excess STES around the edges was trimmed with a razor blade.

Fabrication of lung inserts

For images that included lung tissue, separate molds were created in a similar fashion to the soft tissue molds described above in order to produce lung inserts for the phantom. Unlike the STES, the LTES is not fluid and must be spread into the lung molds. As with STES introduction, waxed paper along with smooth, weighted boards were used to ensure that the LTES inserts were uniform in thickness. The LTES is not as strong as the STES and did not remove as easily from the foam molds, requiring that the molds be cut away from the newly formed lung slices. These slices, which were an exact fit to the corresponding voids in the soft tissue slice, were then fixed to the soft tissue slice with the introduction of the BTES into rib locations.

Fabrication of bone

The method of placing bone into the soft tissue slices was analogous to that of Jones et al.⁵² First, the bottom of each soft tissue slice was sealed using contact paper to prevent any uncured BTES from running under the slice. Any soft tissue island connectors were then removed using a razor blade. An appropriate amount of BTES was mixed to fill the voids in the soft tissue slices that were left for bone tissue. A heat gun was used to warm the BTES material in order to reduce its viscosity and make it easier to mix and pour. The BTES material was then placed in a pastry bag including a pastry tip (#12) and forced into the appropriate voids in the soft tissue slices, taking care to avoid creating air pockets during pouring. Air pockets that were trapped during bone insertion would typically rise to the surface, where they could be pierced

and eliminated. Bone locations were slightly overfilled because it was found easier to remove excess bone than to add additional bone after curing. The segmented data set was referenced to avoid accidentally filling any voids intended to contain air. The BTES was allowed to cure for 48 hours. Finally, the contact paper masks were removed and the bone locations within each phantom slice were sanded flush with the soft tissue using a belt sander with an 80 grit belt. Figure 2-2 shows a completed slice which includes the STES, LTES, and BTES materials integrated into a transverse slice of the phantom.

Phantom assembly

Once all the phantom slices were completed, the organs and locations of dosimetric importance were selected. Full-scale printouts of the segmented images containing these measurement locations were used to trace and label the organs of interest onto the physical phantom slice using a permanent marker. Additionally, phantom slices containing these locations were left unattached to a bordering slice in order to allow access for dosimeter insertion. All other slices were bonded to adjacent slices using commercially available wood glue. The glue was placed uniformly over all areas of a slice surface with the exception of air spaces and LTES. Wood glue has been found to behave radiologically similar to soft tissue at diagnostic energies.⁵² Bonding slices of the phantom into sections permits easy disassembly/reassembly of selected portions of the completed phantom. During assembly, slices were aligned using registration marks and then glued together sequentially. After assembly was completed, excess wood glue was removed using wire cutters and registration marks were removed with a razor blade.

Results

Materials

Soft tissue-equivalent substitute

The STES was empirically evaluated using an x-ray source (3.9 mm Al HVL at 80 kVp) to have an HVL of 25 mm at 80 kVp, and 29 mm at 120 kVp. The measured density was 1.04 g cm^{-3} . The average HU for the STES material was found to be 9.8, at the lower end of the widely accepted range for human muscle (10-40 HU). However, the measured value is considered acceptable because STES represents a homogenized mixture of both muscle and adipose tissue, with the latter having a HU range of -50 to -100.

Lung tissue-equivalent substitute

The density of the LTES was measured to be 0.33 g cm^{-3} , agreeing with the targeted lung density for full inspiration. The average HU for the LTES material is -678.4, consistent with widely accepted HU values for lung, which range from -500 to -1000.

Bone tissue-equivalent substitute

The BTES has been previously characterized⁴⁷ and empirically evaluated to have an HVL of 9.8 mm at 80 kVp, and 13.3 mm at 120 kVp. The BTES material had an average HU of 622. This result is consistent with widely accepted HU values of bone, which range from 400 to 1000.

Completed Phantom

To date, three adult phantoms have been created using the methods and materials described in the previous section. As previously mentioned, the first phantom created, shown in Figure 2-3(a), was an adult male based on a segmented tomographic data set. The color differences observed between phantom regions occurs as a result of extended exposure of one of the pre-mixed urethane mixture components to humidity; however, testing showed no radiological difference. This color variation is more apparent in the first phantom since it was

constructed over a longer period of time. While the arms are not shown in the Figure 2-3, they can easily be attached when the phantom is used for dosimetry measurements. Also, as previously mentioned, the next two phantoms created were based on computational adult hybrid phantoms developed at UF representing the 50th percentile adult male and female, as shown in Figures 2-3(b) and 3(c), respectively. Figure 2-4 shows the computational adult hybrid 50th percentile adult male phantom. Although not pictured, both hybrid phantoms also include a pelvis section which extends to mid-thigh. Surface markings seen on all phantoms (black markings) refer to slice number and were used during the assembly process to keep slices in order.

Figure 2-5 shows a CT topogram of the adult tomographic phantom of Figure 2-3(a). A Vac Fix reusable patient positioning system for radiation therapy (S&S Par Scientific, Houston, TX) was used to hold the phantom and keep the slices together during imaging. The horizontal dark lines located within the phantom present in Figure 2-5 are slight gaps resulting from the vacuum bag's inability to perfectly hold all sections of a supine phantom in place. However, dosimetric measurements for CT have shown little difference when these gaps are present. The weight of the completed phantom as shown in Figure 2-3(a) is 54 kg.

Discussion

Urethane based STES has numerous advantages over the epoxy resin based soft tissue substitute originally proposed by Jones et al.⁴⁷ First, it is much less viscous than the epoxy resin soft tissue substitute, making it easier to pour into the foam molds. Once cured, it is easily removed from the foam molds; this is not the case with the epoxy resin materials. Additionally, it requires fewer modifying constituents than epoxy resin based tissue equivalents, and therefore better retains homogeneity. The urethane based STES remains pliable and strong when cured, while the epoxy resin soft tissue substitute is brittle when cured and can break under stress or

when dropped. Because of these properties, the urethane based material is more durable and unlikely to be damaged with use. Finally, STES better accommodates the insertion of real-time dosimeters, only requiring a thin slit to be cut into the material to allow passage of electrical or optical cords that connect the active regions of the detector to a read-out device; this avoids any potential concerns about radiation streaming along machined dosimeter channels.⁵²

Creating molds resulting in a uniform 5 mm thick phantom slices proved more challenging than expected. Small variations in individual slice thickness can accumulate to create large discrepancies when hundreds of slices are combined. Early on, molds would occasionally display a variation in cutting depth throughout the slice. The engraving system hardware and software was initially suspected and investigated. However, it was found that this variation in cutting depth was the result of the foam template bowing upwards and losing adhesion to the engraving table during the milling process. Similarly problematic, engraving path depths were also initially set to the desired 5 mm, which was expected to result in a 5 mm thick soft tissue slice. However, the excess freshly poured STES could not be pressed infinitely thin, and so an additional thickness of 0.5-1 mm would often result. Thicknesses of this magnitude, reflexively considered minor, are in fact considerable with respect to 5 mm thick slices, resulting in slices that were 10-20% too thick. This problem was corrected for by adjusting the indicated engraving depth to 4 mm and using a consistent procedure to define the cutting surface to the engraving system.

Conclusion

A unique methodology has been developed to construct anthropomorphic phantoms for use in dosimetry studies. While the value of this methodology has already been proven with the construction of three adult phantoms, it should be noted that the same methodology could be applied to the construction of phantoms of all sizes and ages. In particular, our group plans to

develop a family of phantoms that accurately represent patients of differing heights and weights. Future works also include the investigation of an adipose tissue-equivalent substitute which could be added to the existing phantoms, or included as an additional step in the construction of a new phantom, to represent subcutaneous fat in order to accurately model more obese patients. While anthropomorphic phantoms have many potential applications, this particular phantom series was created to quantify organ doses from diagnostic procedures. It is anticipated that other institutions could create their own phantoms for regular clinical use by following the methodology and using the described tissue equivalent materials for a total material cost of less than \$3500.

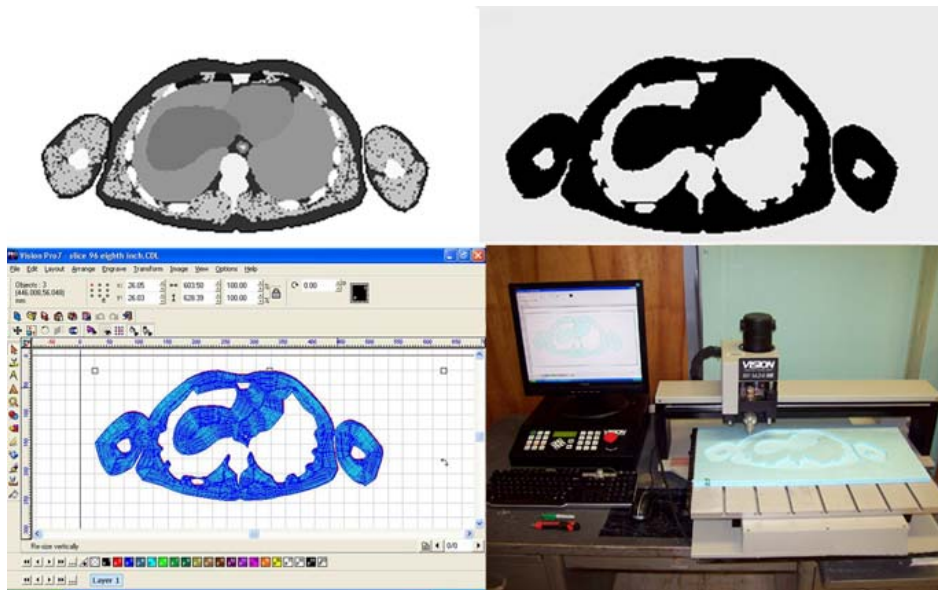


Figure 2-1. The steps in the phantom construction process: segmented CT image (top left), soft tissue bitmap (top right), VisionPro engraving path (bottom left), engraving system milling a soft tissue mold (bottom right).

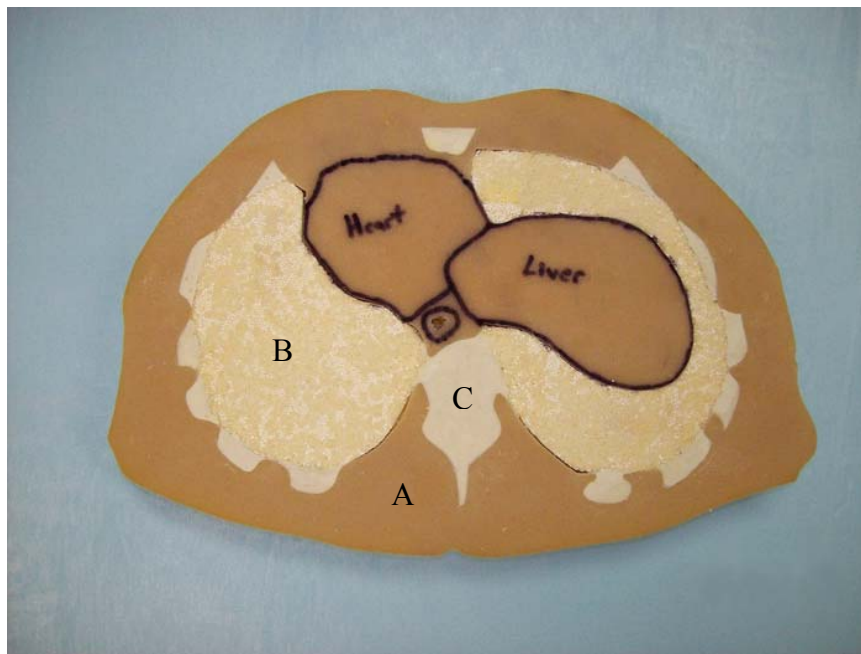


Figure 2-2. A fully formed phantom slice. A) STES. B) LTES. C) BTES.

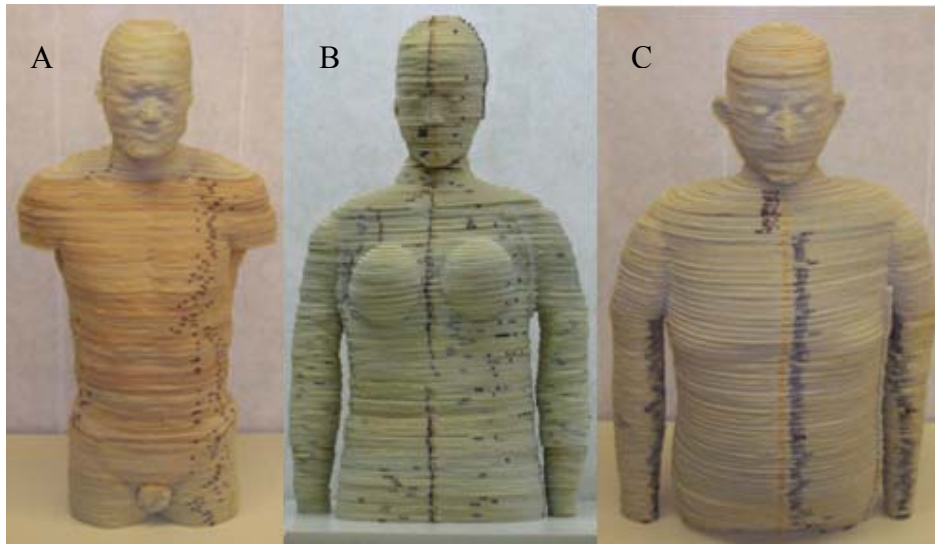


Figure 2-3. The UF adult phantom series. A) Phantom (i.e., GatorMan) based on a segmented CT data set of an adult male. B) Phantom based on a computational adult female hybrid data set. C) Phantom based on a computational adult male hybrid data set.

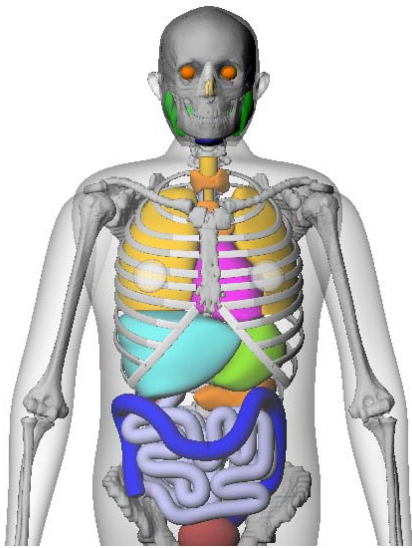


Figure 2-4. The computational adult hybrid 50th percentile adult male phantom.

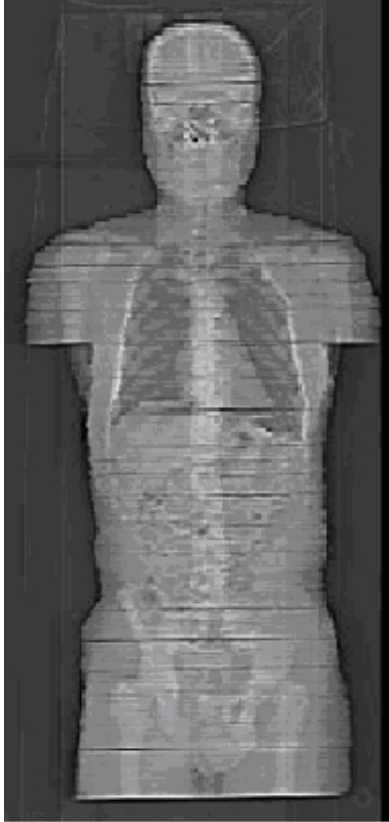


Figure 2-5. A CT topogram of a tomographic physical phantom.

CHAPTER 3 CT ABDOMEN/PELVIS DOSIMETRY STUDY

Introduction

It is useful to assess the radiation dose to patients for particular CT studies. Absorbed dose, effective dose, and organ dose measurements all permit a better understanding of the risks associated with the radiation exposure to patients receiving specific CT studies. With technological improvements to CT, the patient dose received during exams is becoming less intuitive. Factors such as MDCT, ATCM, overbeaming, overranging, scan technique selection, as well as scanner manufacturer differences all play a confounding role in the radiation dose received to a patient. Direct dosimetric measurements using physical phantoms provide a metric that accounts for all confounding factors. Carefully designed experiments can provide the relationships between CT parameters and patient doses. This study illustrates usefulness of dosimetric studies that can be performed using an anthropomorphic phantom.

Materials and Methods

A Siemens SOMATOM Sensation 16 helical MDCT scanner and an adult anthropomorphic phantom from the UF phantom series were used for all scans. A Vac Fix reusable patient positioning system for radiation therapy (S&S Par Scientific, Houston, TX) was used to support the phantom and keep the slices in place during CT scans.

Study Selection

The CT exam selected was an abdomen/pelvis scan. It was decided that an abdomen/pelvis study would be particularly useful due to the presence of many especially radiosensitive organs, as well as the fact that this study is associated with numerous indications (e.g., abdominal pain, appendicitis, abdominal hernia). Scan protocols were taken from the UF Shands Department of Radiology website (<http://xray.ufl.edu/patient-care/protocols/>)⁵⁵ for an

abdomen/pelvis exam. The acquisition of this scan begins at the dome of the diaphragm, and ends at the pubic symphysis. This range is illustrated in Figure 3-1. It was determined using the CT data set from which the phantom was constructed, that this abdomen/pelvis range corresponded to a range from slice 97 to slice 176 in the adult phantom.

Dosimetry System and Integration

The dosimetry system used was a water-equivalent plastic scintillator based fiber optic coupled (FOC) dosimetry system developed at the University of Florida; this system is described in Chapter 1. A major advantage of this type of dosimetry system over other commonly used systems is that it does not over-respond to low energy photons. This is of particular concern for in-phantom dosimetry. Another advantage is that measurements can be taken and recorded *in situ*. This permits multiple measurements at identical point locations within a phantom, taken using different scan techniques, without disturbing the phantom. The FOC dosimetry system is capable of running many channels, but presently allows two simultaneous point measurements. Measurements from the dosimetry system were collected using 100 ms bins since total counts were required, and not finely resolved real-time information.

Placing the FOC dosimeters within the phantom is a simple process. A point of interest (i.e. organ dose location) within a segment of the phantom is identified, and then a razor blade is used to create a thin slit in the phantom from the point of interest to the edge of the phantom. The fiber is pressed into the slit, and the phantom segment is set back into its location within the adult phantom.

Selection of Point Dose Measurement Locations

The choice of point locations (corresponding to organ dose locations) at which to place dosimeters relied primarily on ICRP Publication 103 and ICRP Publication 89.^{5, 56} A representative point within the phantom was designated for each radiosensitive tissue given a

weighting factor in ICRP 103. The point location was determined using the segmented CT data set on which the phantom was modeled. Especially radiosensitive tissues (i.e. ICRP 103 tissue weighting factors 0.01 and greater) with larger, longer, or irregular shapes had multiple dosimetry point locations. Also, whether an organ was located outside the user defined scan volume as well as how far from the scan edge was considered because the dose drop-off just outside the scan volume makes a single point dose less representative of average organ dose, and organs far (>~25 cm) from the scan volume would receive very little radiation. Multiple point dose locations were assigned to the esophagus, the lungs, the heart, the liver, and the colon. With the exception of bone marrow, the average of the point dose measurements for each tissue was taken to represent the average organ dose for that particular tissue. Bone marrow used a weighted average based on the percent of active bone marrow in a given bone as described in ICRP 89 for a 40 year old human.⁵⁶ These values are listed in Table 3-1. Ideally, numerous points would be taken for each radiosensitive tissue, but this is less practical when taking into account the limited number of simultaneous measurements per scan in combination with an inclination to conserve the x-ray tube lifetime. The tissues, locations, and matching phantom slices are listed in Table 3-2.

Technique Selection

Besides quantifying the radiation dose received by a patient undergoing an abdomen/pelvis CT scan, the effect that the beam collimation selection had on the absorbed radiation dose was also studied. Two sets of helical scans were performed. Both sets used identical values for all techniques except for detector collimation width. The scan settings were as follows: 120 kVp, 130 mAs, 0.5s gantry rotation time, 5 mm reconstruction width, CAREdose4D (Siemens ATCM) OFF, Pitch 1. The two sets of detector collimation values used were 16×1.5 mm and 16×0.75 mm. It is important to distinguish between detector collimation and beam collimation.

The collimation settings referred to in this study are detector collimation settings. Both beam collimation and detector collimation are directly related, and adjusting one selection automatically adjusts the other, but the magnitudes are slightly different. To ensure similar slice sensitivity profiles for each detector array in MDCT, manufacturers typically adjust the collimation so that the focal spot-collimator blade penumbra falls outside the detector's edge. Therefore, beam collimation is slightly greater than detector collimation in MDCT. Pitch values and table translation speeds are functions of detector collimation. It is difficult to model ATCM in CT, and so CAREDose4D was turned off to better allow for future data comparisons with Monte Carlo simulations. An mAs of 130 was selected because this was the default effective mAs with CAREDose4D turned on after the scout image was taken.

The range of the scan was set by placing metallic push-pins into phantom slices 97 and 176 before the scout image was acquired. Because of the high attenuation of the metallic push-pins, the marked slices were then readily identifiable within the scout image on the console. The push-pins were then removed before the abdomen/pelvis scan acquisitions. Both sets of scans used precisely the same console-set start and stop positions, and therefore had identical console-set scan lengths. This range will be referred to as the user planned scan range.

Overranging, Beam Width, and Ramp-Up Time

In order to quantify the x-ray tube ramp-up time and overranging for the Siemens SOMATOM Sensation MDCT scanner, the experiment depicted in Figure 3-2 was carried out. The FOC dosimetry system was used with data points being recorded at 0.05 s intervals. Reference fibers were not used since the magnitudes were not of interest; only the timing was of concern. Two real-time dosimeters were fastened a fixed distance apart on a radio-transparent material (to avoid backscatter from the table). A third dosimeter was fixed within the MDCT scanner bore ensuring that it was always within the primary beam. A user planned scan range

was chosen, and different combinations of techniques were selected. Distances between dosimeters and user planned scan edges were measured using the console and scout image. The real-time dosimetric data were plotted and the rising and falling edges for curves were recorded. Calculated table speeds agreed with expected table speeds, and were used to convert the times of rising and falling edges into distances. The table speed (TS) can be derived for MDCT scans by using Equation 3-1.⁴²

$$TS(mm/s) = \frac{pitch \times detector_collimation(mm)}{rotation_time(s)} \quad (3-1)$$

The active area at the tip of each plastic scintillator fibers used for this study is 2 mm long. Active tip length was not an issue for the fiber located within the bore of the scanner since its entire active element was exposed simultaneously during measurements. Nor was this an issue when comparing the distances corresponding to times of rising (or falling) edges between the dosimeters attached to the table. However, when comparing the distances corresponding to rising edge times with those of falling edge times, 4 mm were subtracted from the resulting distances. These distances were compared with the user planned scan range boundaries to evaluate the overranging for different technique selections. Also, the distance corresponding to the rising edge time subtracted from the distance corresponding to the falling edge time of a curve minus the 4 mm that account for the active tip length was equal to the beam width. Ramping up times for the x-ray tube were evaluated using the real-time curves from the dosimeter located within the bore of the MDCT scanner.

Results

Scintillator and reference fiber counts were recorded and corrected using the previously determined PMT calibration factors. The net counts for each dosimeter were converted to exposure (mR) using the calibration factors determined for each fiber. These exposure values

were then converted into absorbed dose (mGy) using the conversion $0.96 \text{ mGy} = 100 \text{ mR}$ for soft tissue. Finally, the average absorbed dose for each tissue was converted into its contribution to effective dose (mSv) using the ICRP 103 weighting factors.

Detector Collimation Width

Figure 3-3 plots the absorbed dose values measured for each point dose location for both collimation widths studied. The blue region in Figure 3-3 represents the user planned scan range. The average absorbed dose within the user planned scan range for the $16 \times 1.5 \text{ mm}$ collimation width was 9.3 mGy, with all values between 7.0 and 13.3 mGy. The average absorbed dose within the user planned scan range for the $16 \times 0.75 \text{ mm}$ collimation width was 10.2 mGy, with all values between 7.8 and 15.8 mGy. Within the user planned scan range, the average absorbed dose values as well as the point by point dose comparison consistently demonstrate a higher absorbed dose value for the $16 \times 0.75 \text{ mm}$ collimation width than the corresponding absorbed dose value for the $16 \times 1.5 \text{ mm}$ collimation width. The average absorbed dose for those points located within the 5 cm on either side of the user planned scan range for the $16 \times 1.5 \text{ mm}$ collimation width was 6.2 mGy, and the average absorbed dose for those points located within the 5 cm on either side of the user planned scan range for the $16 \times 0.75 \text{ mm}$ collimation width was 5.6 mGy. The apparent absorbed dose savings achieved within the user planned scan range resulting from a greater collimation width is diminished by a slight increase in absorbed dose to areas outside the user planned scan range.

Figure 3-4 plots differences in absorbed dose measurement for all corresponding point dose locations for beam collimations of $16 \times 1.5 \text{ mm}$ and $16 \times 0.75 \text{ mm}$. As in Figure 3-3, the user planned scan range is indicated by the blue region. The average point by point difference within the user planned scan range was -1.0 mGy, with all differences lying within a range of -2.5 to 0.1 mGy. Outside the user planned scan range, the greater collimation width resulted in typically

higher point dose measurements, with an average absorbed dose difference for those points located within the 5 cm on either side of the user planned scan range of 0.6 mGy. The largest difference between any two corresponding point measurements (5.9 mGy) was at the point measurement location for the testes. There is a clear trend of decreased absorbed dose within the user planned scan range while using a greater collimation width, and increased absorbed dose outside the user planned scan range while using a greater detector collimation width.

Figure 3-5 is similar to Figure 3-3, but instead of plotting absorbed dose values for each point, average absorbed dose values for each radiosensitive tissue are multiplied by the corresponding ICRP 103 tissue weighting factor. This provides some insight into how changing collimation width might affect effective dose. Excluding those tissues spread throughout the body (i.e., bone-marrow, bone surface, skin, lymphatic nodes, and muscle) and therefore not distinguishable as located either inside or outside the user planned scan range, the contribution towards effective dose from within the user planned scan range was 3.8 mSv for the 16×1.5 mm collimation width and 4.1 mSv for the 16×0.75 mm collimation width. Similarly, the contribution towards effective dose from outside the user planned scan range was 1.6 mSv for the 16×1.5 mm collimation width and 1.1 mSv for the 16×0.75 mm collimation width. Due to tissue locations relative to the scan volume and tissue weighting factors, the contributions from the lung, breast, liver, stomach, colon, bladder, and testes dominated the contributions to effective dose from other tissues.

Figure 3-6 plots differences in contribution to effective dose for all corresponding tissues for beam collimation widths of 16×1.5 mm and 16×0.75 mm. The largest savings in effective dose due to using a larger beam collimation width (-0.2 mSv) come from the stomach, colon, and bladder, all of which lie within the user planned scan range. The largest increase in effective

dose due to using a larger beam collimation width (0.5 mSv) comes from the testes, which lies just outside the user planned scan range.

Figure 3-7 plots the ratio of corresponding absorbed dose measurements for the 16×1.5 mm beam collimation width and the 16×0.75 mm beam collimation width for all points within the user planned scan range. Within the user planned scan range, the absorbed dose measurements for the 16×1.5 mm collimation width were on average only 91% as great as the absorbed dose measurements for the 16×0.75 mm collimation width; the standard deviation for this set of calculated ratios is 3%.

Effective Dose

The contributions to effective dose from all tissues except for bone-marrow, bone surface, skin, lymphatic nodes, and muscle are as described above. The tissues spread throughout the body require additional assumptions in order to estimate their contribution to the effective dose. The strategy employed to quantify the contribution to effective dose from these large tissues was to separate these tissues into portions considered inside and outside the exposed scan range. Absorbed dose values based on the data from Figure 3-3 were assigned to tissue portions within the exposed scan range, and tissue portions outside the exposed scan range were assigned a null absorbed dose. In doing this, estimates of average tissue absorbed doses could be made. Using Figure 3-3, tissue portions located within slices 92 to 181 were selected as having received similar doses to those within the user planned scan range.

The portions of each tissue (except lymph nodes) located within the exposed scan range were obtained using the segmented CT data set on which the physical phantom is based. Using ImageJ software (Version 1.34s, National Institute of Health, Bethesda, MD) substack select and analyze histogram functions, the number of pixels for a particular tissue type located within slices 92 to 181 was compared to the number of pixels for the same tissue type located within the

entire phantom. This was done for skin, muscle, and each individual bone containing bone marrow. Bone surface was compared similarly after assuming its being proportional to total bone. The portion of lymph nodes within the exposed scan range was based on diagrams of the lymphatic system. The lymph nodes that would be located within the scan range were counted and divided by the total lymph nodes within the diagram.⁵⁷ This rough estimate was not of much concern considering the very low tissue weighting factor for lymph nodes. The portions of each tissue type located within the exposed scan region are listed in Table 3-3.

Bone surface, lymphatic nodes, and muscle were assumed to have received the average absorbed doses for each collimation width (9.3 mGy for 16×1.5 mm and 10.2 mGy for 16×0.75 mm) within the exposed scan range and 0 mGy outside that range. Skin was assumed to have received the maximum absorbed dose measured for each collimation width (13.3 mGy for 16×1.5 mm and 15.8 mGy for 16×0.75 mm) within the exposed scan range, and 0 mGy outside that range. The bones containing bone marrow were given their average measured absorbed doses.

The portion within the exposed scan range for each tissue was multiplied by the absorbed dose and the tissue weighting factor to determine the contribution of each tissue toward effective dose. Each bone containing bone marrow was additionally multiplied by its percentage of active bone marrow. The contribution from all of these tissues toward effective dose was 0.7 mSv for the 16×1.5 mm collimation width, and 0.8 mSv for the 16×0.75 mm collimation width.

And so, the estimated effective dose for the abdomen/pelvis scan acquired with a 16×1.5 mm collimation width was 6.1 mSv, and the estimated effective dose for the abdomen/pelvis scan acquired with a 16×0.75 mm collimation width was 6.0 mSv. These values are consistent with those expected in an abdomen MDCT scan.⁷ However, the previously mentioned

comparisons of effective dose between collimation widths, inside and outside of the user planned scan range are more useful than the magnitude.

OVERRANGING, BEAM WIDTH, AND RAMP-UP TIME

Figure 3-8 is a plot of the data resulting from the one of the acquisitions for the study described in Figure 3-2. For the techniques used in the abdomen/pelvis study, the overranging was found to be 55 mm for the 16×1.5 mm collimation width, and 33 mm for the 16×0.75 mm collimation width. These overranging distances were obtained using the rising and falling edge times from the FOC fiber located within the bore of the scanner. These times do not account for beam width. Therefore, a half beam width of additional exposure is present on each side of the overall scan. And so, the scan using a 16×1.5 mm collimation exposed an additional 24 mm (79 mm total) outside the user planned scan range, and the scan using a 16×0.75 mm collimation exposed an additional 12 mm (45 mm total) outside the user planned scan range.

The average measured beam width using the FOC setup in Figure 3-2 for the 16×1.5 mm detector collimation was 27.38 mm. This was very similar to the manufacturer value of 27.25 mm and a previously measured value of 28.3 mm.⁵⁸

In order to quantify x-ray tube ramp-up times, plots for channel 3 were reviewed, and the times necessary to attain dosimetry readings similar to those within the user planned scan range were recorded. Similarly, ramping down times were also recorded. These times needed no correction accounting for the length of the tip of the dosimeter because the entire active element was simultaneously exposed for this fiber located within the bore of the scanner. It was found that the Siemens SOMATOM Sensation 16 helical MDCT scanner used in this study had a ramp-up and ramp-down time of approximately 0.1 s. This time was considered short enough to ignore with regard to patient dosimetry.

Discussion

The results from this study clearly highlight two dose contributors with respect to patient dose in helical MDCT, namely overbeaming and overranging.

Overbeaming

To ensure similar slice sensitivity profiles for each detector array in MDCT, manufacturers typically adjust the collimation so that the focal spot-collimator blade penumbra falls outside the edge detectors.^{11, 39, 40} Therefore, beam collimation is slightly greater than detector collimation in MDCT. Pitch and table feed per rotation are functions of detector collimation, and so the larger beam collimation results in additional dose to patients. For a pitch value of 1, the table will translate the thickness of the detector collimation in one gantry rotation. The larger beam collimation therefore overlaps during each rotation. The differences between beam collimation width and detector collimation width for the two detector collimation widths studied are similar in magnitude,^{40, 65} but this difference as a percentage of total incident beam does increase with decreasing detector collimation width. And so, over the course of identical scan lengths, the amount of overbeaming coinciding with a larger detector collimation width will be less than that coinciding with a smaller detector collimation width. Overbeaming explains the increased dose within the user planned scan range observed for the lower detector collimation width in Figures 3-3 through Figure 3-6. Figure 3-9 illustrates the effect that overbeaming has on the dose contribution for two different detector collimation widths. The smaller detector collimation width requires additional gantry rotations to cover the same scan length, which leads to increased amounts of overbeaming.

Some rudimentary calculations can be performed to evaluate whether or not the dose savings observed within the user planned scan range is plausibly the result of overbeaming. Figure 3-10 illustrates the overbeaming present in a 24 mm scan section within the user planned

scan range due to the 16×1.5 mm and 16×0.75 mm detector collimation widths. For simplicity, the overbeaming for both collimation widths are considered to be equal,^{29, 58} and are treated as an overlapping primary beam with a linearly decreasing intensity that drops to zero after a distance x. A 24 mm section using the 24 mm collimation width will receive 24 mm of primary plus x worth of overlapping primary beam from the adjacent sections (not shown). A 24 mm section using the 12 mm collimation width will receive 24 mm of primary plus 2x worth of overlapping primary beam. The ratio of these two quantities should reflect the average ratio of absorbed doses measured within the user planned scan range as shown in Figure 3-7 (91%). Equation 3-2 compares these ratios.

$$\frac{24 + x}{24 + 2 \cdot x} = 0.91 \quad (3-2)$$

Solving for x in Equation 3-2, the additional primary beam and penumbra past the edge of the detector array drops to zero after 2.6 mm, and drops to half-value at 1.3 mm (since a simplistic linear decrease after the edge of the detector array was assumed). Even so, this value agrees well with previously measured values using the same Siemens SOMATOM Sensation MDCT scanner (~2.1 mm),⁵⁸ those provided by the manufacturer (~1.7 mm),⁵⁸ a general value given for most MDCT scanners (~1.5 mm)²⁹, and that measured using an FOC dosimetry system (~1.7 mm). The details of the FOC derived measurement is in the following subsection of this chapter. A more precise profile for the penumbra should improve the approximation. Since it was possible to use measured absorbed dose reduction to approximate the difference between beam collimation width and detector collimation width, it should be possible to use a measured beam width to approximate potential absorbed dose reduction. And so, the decrease in absorbed dose that can be expected for locations within a user planned scan range by using a larger detector

collimation width setting instead of a smaller detector collimation width setting can be approximated using Equation 3-3.

$$P_{sc} = \frac{LC + x}{LC + \frac{LC}{SC} \cdot x} \quad (3-3)$$

Here, P_{sc} is the percent (fraction) of the absorbed dose resulting from using the smaller detector collimation width, LC is the larger detector collimation width, SC is the smaller detector collimation width, and x is the half the difference between the measured beam width and the detector collimation width.

Overranging

Since the point dose measurements outside the boundaries of the user planned scan range differed in behavior with respect to collimation width setting, overranging was suspected. The reconstruction algorithms for helical MDCT require data from beyond the volume to be reconstructed. Consequently, tissue outside the reconstructed volume is exposed to radiation. This exposed length outside the user planned scan range is known as overranging, but has also been similarly referred to as z-overscanning.^{59,60} Figure 3-11 is a simplified depiction of overranging for helical MDCT scanning. One section width (SW) is automatically added to the planned scan length, so the imaged scan length is slightly longer. Additionally, extra rotations needed for image reconstruction are added to imaged length, resulting in a longer exposed scan length.⁶⁰ The difference in overranging values between different detector collimation settings explains the increased dose outside the user planned scan range, and the large increase in dose to the testes, which were almost 2 cm outside the lower boundary of the abdomen/pelvis scan.

There are two previous studies quantifying the overranging of a Siemens SOMATOM Sensation 16 helical MDCT scanner. Our results agreed very well with van der Molen et al., who used a 102-mm pencil ionization chamber (model CP-4C; Capintec, Ramsey, NJ)

connected to a dosimeter (model 35050A; Keithley Instruments, Cleveland, Ohio) ionization chamber to identify a linear relationship between the dose free in air measurements and the planned length of the scan (in number of tube rotations). The y-intercept of these plots represents the dose from overranging. The y-intercept values were divided by the slope of the dose vs. planned length plots, allowing van der Molen et al. to calculate the number of tube rotations due to overranging; tube rotations could then be converted into distances. Figure 3-12 shows the experimental setup used by van der Molen et al. Figure 3-13 is a representative graph of the relationship of dose to planned CT scan length as created by van der Molen et al.⁶⁰ Tzedakis et al. assumed the overranging to be equivalent to the couch over-travel during scans.⁵⁹ This is an overestimate; their overranging lengths for the smaller and larger collimation values were 14% and 35% too long, respectively, when compared to the van der Molen et al. values.

The FOC overranging study as well as the van der Molen et al. study agreed in magnitude as well as demonstrated that the overranging length in helical MDCT increases with both detector collimation width and pitch. The average dose to tissue savings within a user planned scan range due to increasing collimator width and/or increasing pitch must be weighed against the increase in dose to tissue outside the user planned scan range. Overranging was also found to be independent of user planned scan length. As a consequence, the patient dose received from shorter helical scans has an increased percentage due to overranging, and an increased percentage of that dose is received outside the user planned scan range. Additionally, overranging dose contributions should be considered when more radiosensitive tissues (e.g., breasts, lungs, testes) are near to the outside edges of user planned scan ranges. All of these things are especially important when choosing scan parameters for pediatric patients, whose scan lengths are typically shorter and whose organs are more closely spaced.

Conclusions

The adult phantom from the UF family of physical phantoms and the FOC dosimetry system are capable of providing useful information regarding patient dose in CT. The abdomen/pelvis study illustrated how an anthropomorphic phantom can be used to provide information about absorbed dose to tissue, organ dose, effective dose, and dose trends to patients undergoing particular exams. Dose concepts in helical MDCT such as overbeaming and overranging can also be quantified using an anthropomorphic phantom and dosimetry system. Finally, the real-time aspect of the FOC dosimetry system can be used to directly measure qualities of MDCT such as overranging, beam width, x-ray tube ramping times, and table speed. The combination of tomographic phantom and FOC dosimetry system is an extremely useful, reliable, and practical tool for use in CT dosimetry studies.

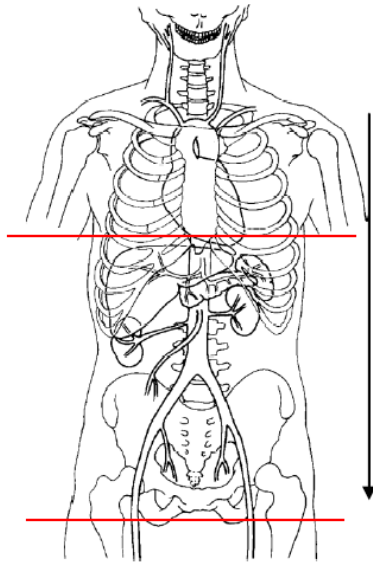


Figure 3-1. Abdomen/pelvis scan range as provided by the UF Shands Department of Radiology website (Clinical Protocol Database, radiology practice Committee of the Department of Radiology, University of Florida. Copyright 2008, http://xray.ufl.edu/protocols/documents/ct/body/abdomen_pelvis.pdf).

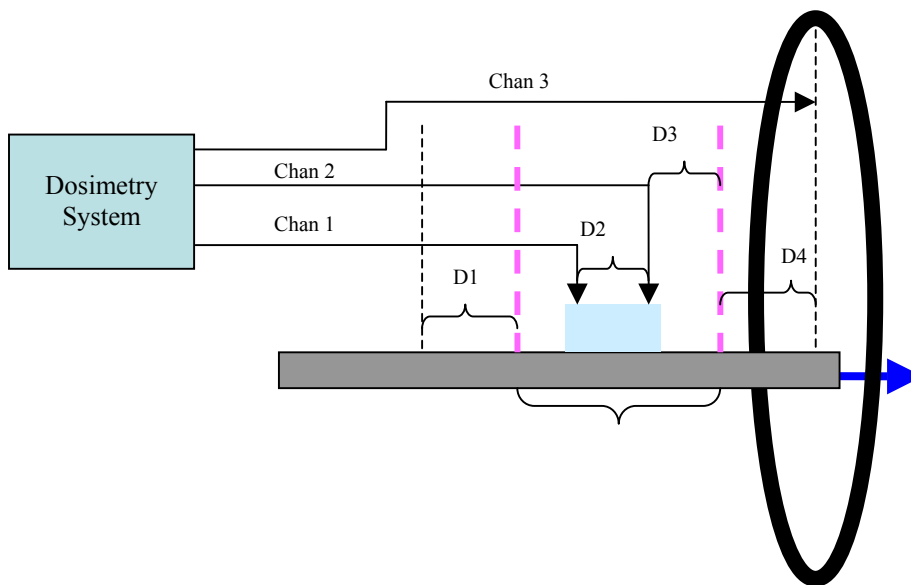


Figure 3-2. Schematic of the experimental setup used to evaluate CT x-ray tube ramp-up and overranging. The dashed pink lines indicate the user planned scan length.

Table 3-1. Active marrow in a given bone expressed as a percentage of active marrow in the body for a 40 year old human.⁵⁶

Bone	Percentage of Active Marrow
Cranium	7.6
Mandible	0.8
Scapulae	2.8
Clavicles	0.8
Sternum	3.1
Ribs	16.1
Cervical Vertebrae	3.9
Thoracic Vertebrae	16.1
Lumbar Vertebrae	12.3
Sacrum	9.9
Os Coxae	17.5
Femora, upper half	6.7
Humeri, upper half	2.3

Table 3-2. Phantom point dose measurement locations.

Organ	Subsection	Phantom Slice	Organ	Subsection	Phantom Slice	
Brain	Superior Anterior	16	Stomach	Superior	104	
	Inferior Anterior	21		Inferior	110	
Extrathoracic Region	Nasal Layer	28	Spleen	Center	104	
	Anterior			Adrenals	Left	107
	Pharynx				Right	107
Oral Mucosa	Larynx	47	Gall Bladder	Center	110	
	Center	33		Kidneys	Left Center	115
Salivary Glands	Left Parotid	33	Pancreas		Right Center	115
	Right Parotid	33		Center	107	
	Left Submaxillary	42	Colon	Superior	115	
	Right Submaxillary	42		Center	130	
	Left Sublingual	42		Inferior	152	
	Right Sublingual	42				

Table 3-2. Continued

Organ	Subsection	Phantom Slice	Organ	Subsection	Phantom Slice
Thyroid	Center	57	Small Intestine	Superior	115
Esophagus	Superior	57		Center	123
	Center	66		Inferior	130
	Center	72	Bladder	Center	159
	Center	80	Prostate	Center	165
	Center	88	Gonads (Testes)	Left	179
Lungs	Inferior	96	Skin	Anterior	130
	Left Superior	66		Posterior	130
	Right Superior	66	Bone Marrow	Cranium	21
	Left Center	80		Mandible	42
	Right Center	80		Cervical Vertebrae	42
	Left Inferior	96		Right Scapula	62
	Right Inferior	96		Left Clavicle	62
	Thymus	Center	62		Right Humerus
Heart	Center	88		Sternum	69
	Inferior	96		Thoracic Vertebrae	80
Breast	Right Breast	88			107
Liver	Superior	96		Ribs	88
	Center	104			110
	Anterior	104			
	Center	104		Lumbar Vertebrae	130
	Posterior	104			
	Left Center	104		Sacrum	144
	Right Center	104		Right Os Coxa	152
	Inferior	110		Right Femur	165

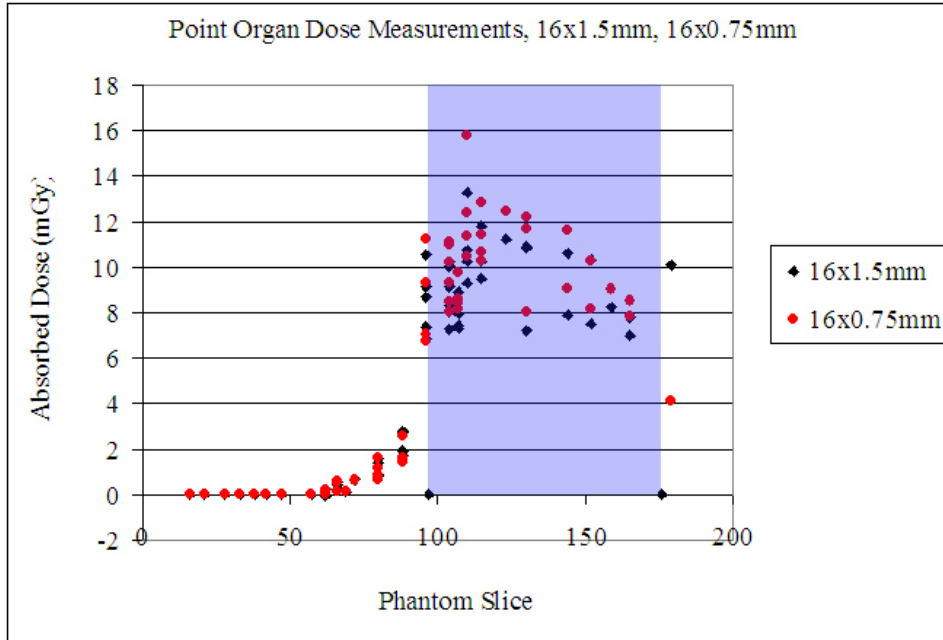


Figure 3-3. Absorbed dose measurement for all point dose locations for detector collimation widths of 16×1.5 mm (black) and 16×0.75 mm (red). Imaged scan range is indicated by the blue region.

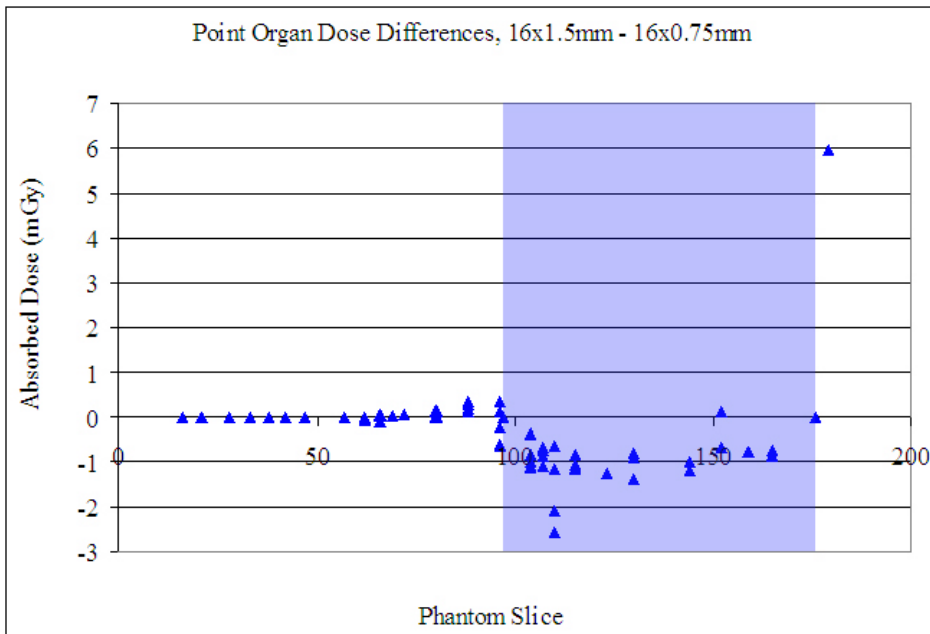


Figure 3-4. Differences in absorbed dose measurement for all point dose locations for detector collimation widths of 16×1.5 mm (black) and 16×0.75 mm (red). Imaged scan range is indicated by the blue region.

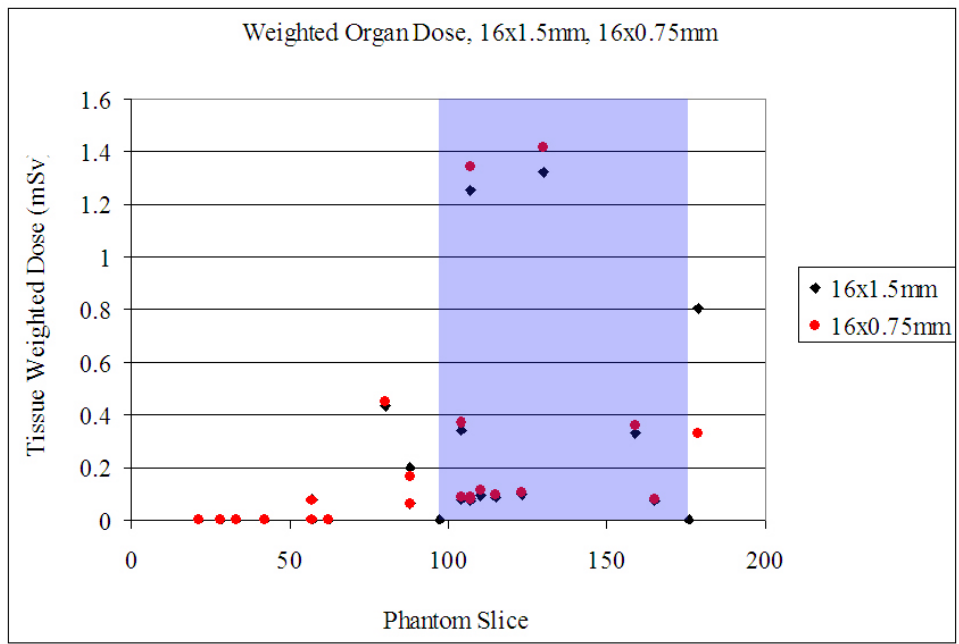


Figure 3-5. Weighted absorbed dose measurement for all point dose locations for detector collimation widths of 16×1.5 mm (black) and 16×0.75 mm (red). Imaged scan range is indicated by the blue region.

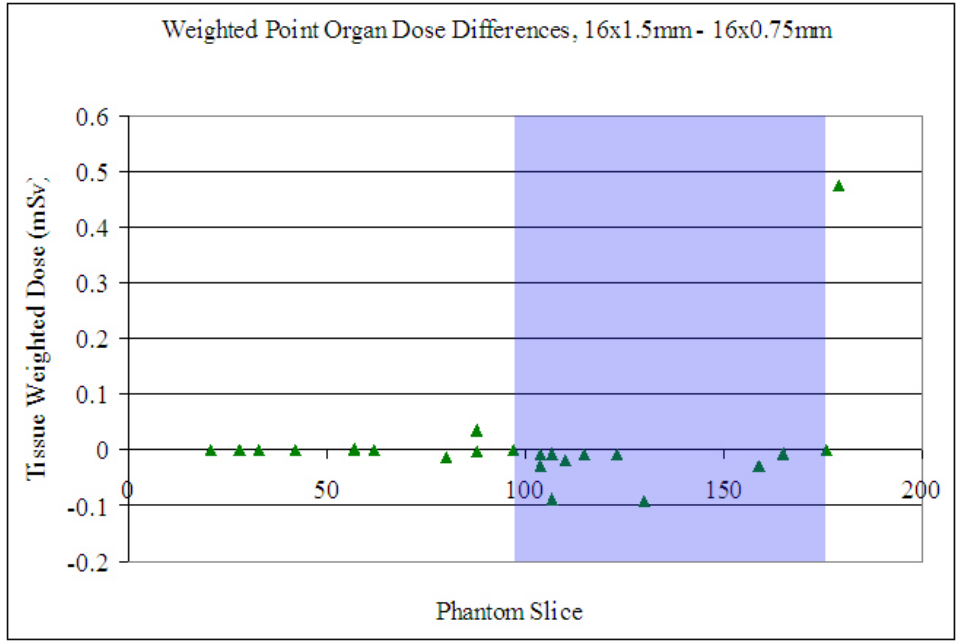


Figure 3-6. Weighted point organ dose differences for detector collimation widths of 16×1.5 mm (black) and 16×0.75 mm (red). Imaged scan range is indicated by the blue region.

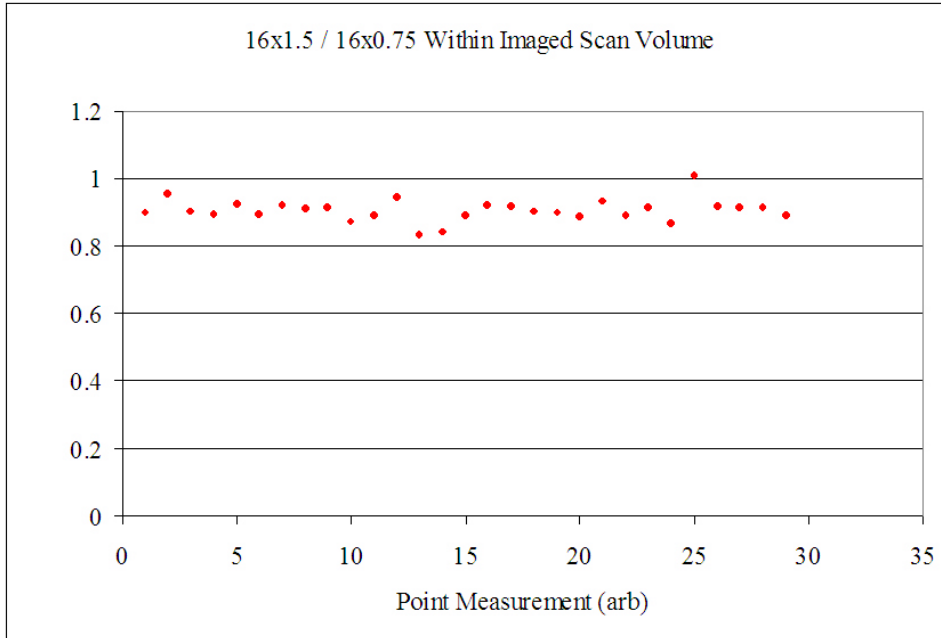


Figure 3-7. Ratio of corresponding absorbed dose measurements for 24 mm detector collimation width and 12 mm detector collimation width for all points within the imaged scan range.

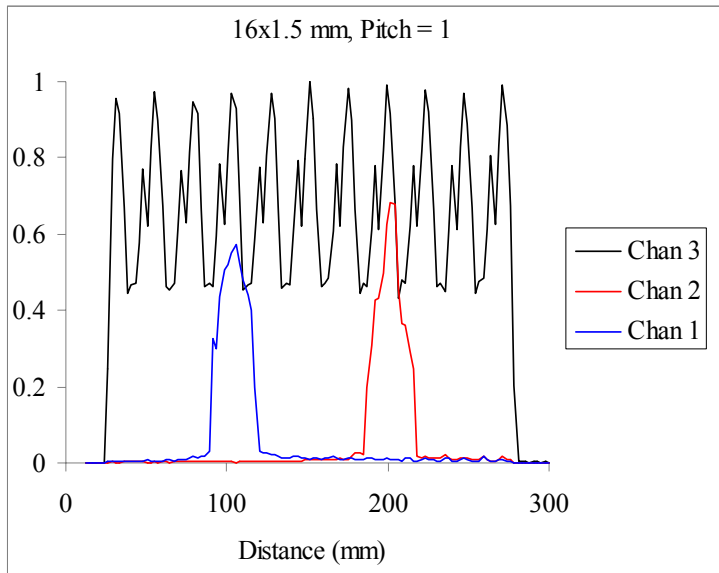


Figure 3-8. Real-time FOC dosimetric data from the experiment illustrated in Figure 3-10. The x-axis was converted to distance using measured CT table speed values.

Table 3-3. The portion of radiosensitive tissue located between slice 92 and 181 as compared to the tissue amount within the entire phantom.

Tissue	Portion of Tissue Exposed to Radiation
Bone Marrow	
Cranium	0
Mandible	0
Scapulae	0
Clavicles	0
Sternum	0.106
Cervical Vertebrae	0
Thoracic Vertebrae	0.378
Lumbar Vertebrae	1
Sacrum	1
Os Coxae	1
Femora, upper half	0.652
Humeri, upper half	0
Ribs	0.429
Bone Surface	0.357
Skin	0.376
Muscle	0.366
Lymph Nodes	0.375

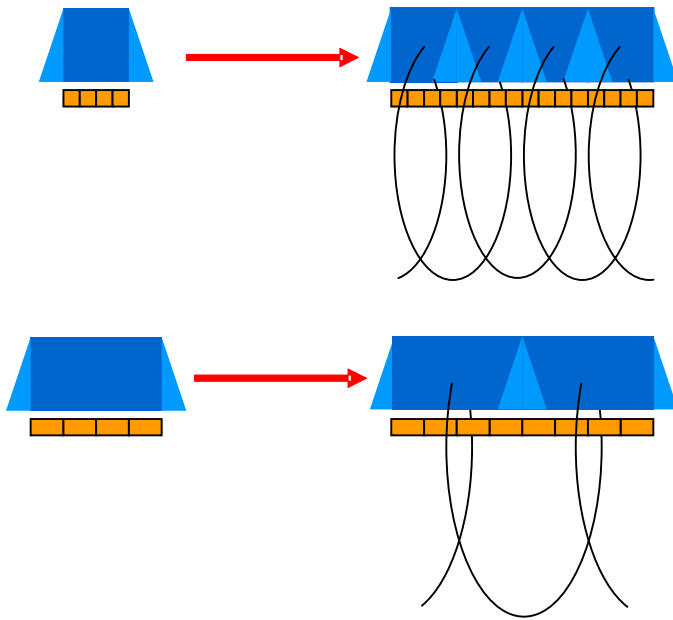


Figure 3-9. Schematic illustrating the difference in overbeaming for two different detector collimation widths over an identical scan length. Represented are the primary beam incident on the detector array (dark blue), the primary beam penumbra not incident on the detector array (light blue), and the detector array (gold).

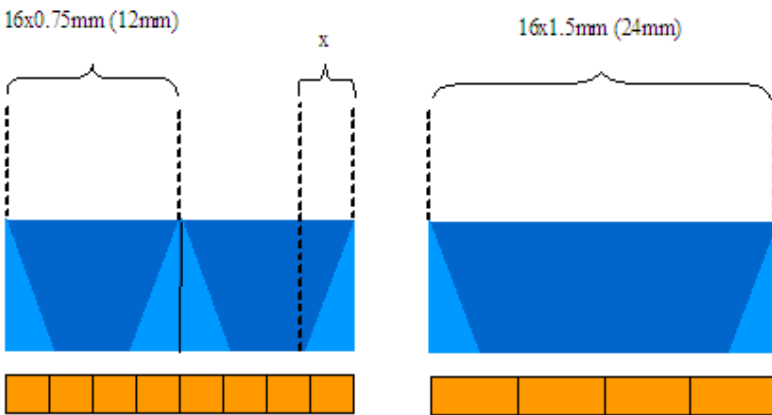


Figure 3-10. The overbeaming present in a 24 mm scan section within the user planned scan range due to 16×1.5 mm and 16×0.75 mm detector collimation widths. Represented are the primary beam incident on the detector array (dark blue), the primary beam penumbra not incident on the detector array (light blue), and the detector array (gold).

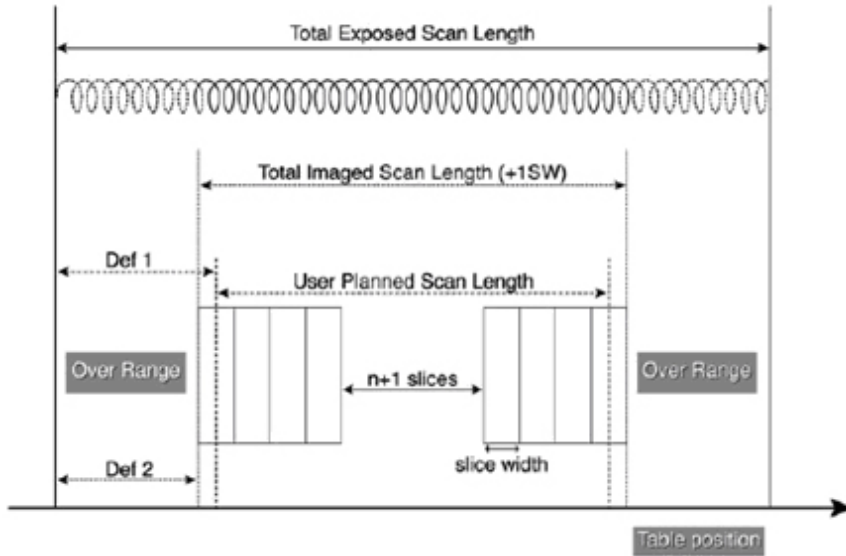


Figure 3-11. A simplified depiction of overranging for helical MDCT scanning. Definitions of overranging vary; either the difference between planned and exposed scan length (Def 1) or the difference between imaged and exposed scan length (Def 2) is used. (A. J. van der Molen and J. Geleijns, *Radiology* **242** (1), 208-216 (2007), Figure 1, p. 210)

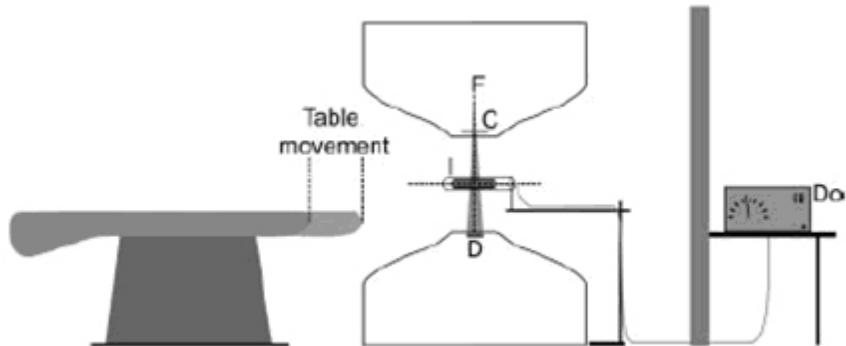


Figure 3-12. Overview setup used by van der Molen et al. I is the ionization chamber, C_ is the collimator, D_ is the detector, Do_ is the dosimeter, and F_ is the focal spot. (A. J. van der Molen and J. Geleijns, *Radiology* **242** (1), 208-216 (2007), Figure 2, p. 210)

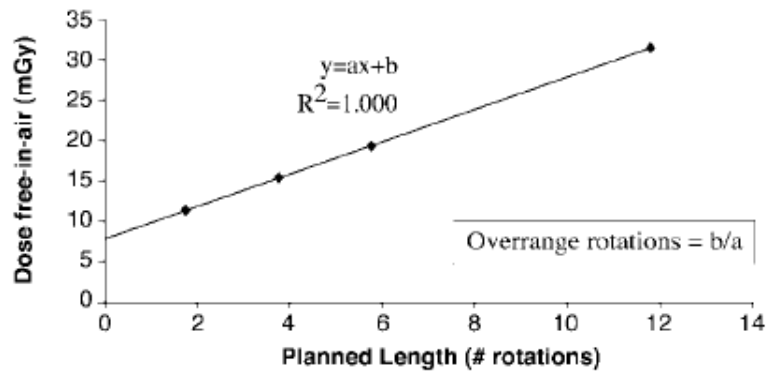


Figure 3-13. Representative graph of the relationship of dose to planned CT scan length. (A. J. van der Molen and J. Geleijns, Radiology 242 (1), 208-216 (2007), Figure 3, p. 211)

CHAPTER 4 COMPARISON TO MONTE CARLO: CT ABDOMEN DOSIMETRY STUDY

Introduction

The major advantage of dosimetric measurements for MDCT scans using physical phantoms as opposed to using computational phantoms is that physical phantom measurements do not require knowledge of the specific energy spectrum, irradiation geometry, or ATCM algorithms. However, using Monte Carlo simulation as opposed to a physical phantom has advantages. First, the average organ doses in physical phantoms are typically extrapolated from one or a few point dose measurements, while Monte Carlo simulations can provide accurate assessments of the absorbed dose averaged across the entire organ. This is particularly useful in larger organs, situations where a noticeable dose gradient is present, or tissues spread over a large area (e.g., skin or bone marrow). Second, computational phantoms are less expensive, easier to manage, and easier to distribute. Access to a CT scanner is also not necessary. Dosimetric measurements in physical phantoms can be used to verify simulated doses, and vice versa. Physical anthropomorphic phantoms, such as those in the UF phantom series, developed to correspond precisely with a complementary computational (i.e., “twin”) phantom are particularly suited for this purpose.^{34, 49, 53, 59}

This chapter compares physically measured organ doses from Chapter 3 with simulated organ doses obtained using a “twin” computational phantom; these simulations were run by Choonsik Lee using a methodology that closely mirrors that used by Staton et al.⁵⁸

Materials and Methods

Computational Phantom

The adult computational phantom was constructed from the same segmented CT data set used to build the GatorMan physical adult phantom described in Chapter 2. This computational

phantom represents an adult 176 cm in height, 72.8 kg, and it included 59 segmented organs and tissues. The tomographic data have an in-plane voxel resolution of 2 mm×2 mm and a slice thickness of 5.146 mm. The voxel array size is 300×150×344. The tissue properties for soft tissue, bone tissue, and lung tissue were as described in ORNL/TM8381.⁵¹

Computational Model of the CT Scanner

Staton et al. modeled a Siemens SOMATOM Sensation 16 helical MDCT scanner. The CT x-ray source was modeled as a fan beam originating from the focal spot, with a fan beam angle of 52°. The helical path of the source was modeled based on scan length, pitch, and detector collimator setting. The source code generates the directional vectors and starting spatial coordinates for each simulated photon. The fact that the beam collimation is different from the detector collimation was also accounted for. The CT x-ray energy spectra were obtained from the manufacturers. Bowtie filtration and the patient table were also included.⁵⁸

Monte Carlo Codes

The Monte Carlo code MCNPX was used for these simulations. The source subroutine was written to allow different technique factors if the CT simulations to be modified by user-definable input parameters. Included among these parameters are x-ray spectrum, type of filter, pitch, detector collimation setting, and scan range. The computational phantom is comprised of soft tissue, lung tissue, bone tissue, and air. To calculate tissue and organ doses, the total energy deposited in each segmented region is divided by the mass of that region.⁵⁸

Conversion to Absolute Organ Absorbed Dose

Tally outputs for an organ obtained using Monte Carlo radiation transport codes are given in the units for absorbed dose (mGy) per launched photon. In order to relate simulated dose values to experimental dose measurements, CTDI₁₀₀ measurements were measured and simulated for different scan parameters. From these measurements, normalization factors (NF)

are calculated, having units of photons per mAs. Tissue absorbed dose (mGy) is equal to the product of the Monte Carlo simulation estimate of tissue absorbed dose (mGy/photon), the appropriate normalization factor (photon/mAs), the mAs per rotation, and the number of rotations.⁵⁸

Scan Parameters

Both studies from Chapter 3 utilized 120 kVp, pitch 1, mAs 130, with a user planned scan range from phantom slice 97 to phantom slice 176. The first study used a detector collimation width of 12 mm, and the other used a detector collimation width of 24 mm. These parameters were also used in the Monte Carlo simulations. However, the Monte Carlo simulations must be performed over slightly different scan ranges to correctly account for overranging, which is a function of detector collimation. Using the overranging data collected and described in Chapter 3, as well as the paper by van der Molen et al.⁶⁰, the scan range for the 12 mm detector collimation study was determined to begin at phantom slice 94, and end at phantom slice 179. The scan range for the 24 mm detector collimation study was determined to begin at phantom slice 92, and end at phantom slice 181. Also, Monte Carlo simulation normalization factors were obtained using 100 mAs instead of 130 mAs. Simulated organ dose calculations will be scaled by 1.3 before comparing them to measured organ doses.

Results

For both studies, simulated average organ doses calculated were for all organs/tissues with an ICRP 103 tissue weighting factor with the exception of breast, bone marrow, oral mucosa, and lymphatic nodes, which were not segmented in the original data set. For each detector collimation width, the simulated average organ dose (and relative error), the corresponding measured average organ dose, and the percent difference between the two are listed in Table 4-1. Although percent difference traditionally uses an absolute value of the differences, the sign of

the difference was left intact to show which measurement was larger. A negative percent difference in Table 4-1 indicates that the simulated measurement was greater than the measured. The organs located within the user planned scan range are in bold. The average percent difference (absolute values) for organs located within the user planned scan range was 9.9% for the 12 mm detector collimation width, and 9.3% for the 24 mm detector collimation width. Percent differences were typically negative, indicating that the measured organ doses were often less than the simulated average organ doses.

The comparable organs between studies can be used to calculate their contribution to the effective dose for the study; these contributions to effective dose are listed in Table 4-2. For the simulated measurements, the contribution to effective dose was 6.0 mSv for the 12 mm detector collimation width, and 5.8 mSv for the 24 mm detector collimation width. For simulated average organ doses inside the user planned scan range, the contribution towards the effective dose was 4.4 mSv for the 12 mm detector collimation width, and 4.0 mSv for the 24 mm detector collimation width. For the physical measurements, the contribution towards effective dose was 5.2 mSv for the 12 mm detector collimation width, and 5.3 mSv for the 24 mm detector collimation width. For measured average organ doses inside the user planned scan range, the contribution towards the effective dose was 4.1 mSv for the 12 mm detector collimation width, and 3.8 mSv for the 24 mm detector collimation width.

Figure 4-1 and Figure 4-2 show the differences between simulated average organ doses and ICRP 103 tissue weighted simulated average organ doses for the two detector collimation widths studied. Differences between simulated dose measurements for organs within the user planned MDCT scan range are located within the blue region in the figures. Figure 4-3 shows the ratio between simulated average organ doses for the two detector collimation widths

considered. The average of all the ratios for simulated measurements within the user planned scan range was 0.92, with a standard deviation of 0.02. Recall that for measured point dose measurements within the user planned scan range, the average ratio was 0.91, with a standard deviation of 0.03.

Discussion

Comparison of Measured and Simulated Data

Overall, the simulated average organ dose data agreed well with physically measured dosimetric data, despite a few organs having a large percent differences; the agreement was better than previous comparisons between twin phantoms.⁵⁸ The organs with the largest percent differences were out of the user planned scan range (e.g. the heart) or were larger organs (e.g. the small intestine). The percent differences would most likely be reduced if a larger sampling of points were used. For example, the liver had the most dosimetric points (6) for measuring average organ dose, and had a relatively low percent difference. Some of the tissues that may benefit from using a larger sampling of points had low ICRP 103 tissue weightings, and there are diminishing returns with increasing numbers of points measured with respect to the assessment of risk. Other tissues that had large percent differences were widely distributed organs (e.g. skin) that required some assumptions to calculate the average organ dose. The large percent difference for those organs located outside the user defined scan range could also be largely attributable to having chosen incorrect scan limits with respect to overranging. The percent difference between the simulated and measured average dose to the testes is particularly sensitive to the choice of scan limits given to the simulation to account for overranging. Even a small overestimate in the adjustments of scan limits accounting for overranging in the simulations could result in large percent differences between simulated and measured average organ doses.

The effective dose contribution from those tissues considered in the simulation was similar to that calculated using the physically measured data. As expected, the differences between simulated and physically measured effective dose contributions were lower when only considering those tissues within the user planned scan range. Also, the largest contributor to percent difference in effective dose contribution was from the testes. The percent difference in contribution to effective dose for all tissues excluding the testes is less than 5% for both detector collimation widths. Again, small errors in the adjustments to scan edges necessary for overranging would result in large differences in average dose to the testes. Taking multiple physical point dose measurements in the testes to calculate average organ dose would likely bring the physically measured and simulated effective dose contributions closer in agreement.

Sources of Error

Percent differences between measured and simulated data were generally indicative of a lower measured value for average organ dose (compared with simulated data). Measured average organ doses were taken from point dose measurements. Simulated average organ doses were calculated over the entire organ. In addition to this difference, there are a few potential sources of error that can explain observed differences in average organ doses. First, the simulation used tissue references as described in ORNL/TM8381,⁵¹ while the physical phantom used the STES, BTES, and LTES described in Chapter 2. If the physical phantom tissue was more attenuating than the reference tissues used in the simulation, lower point dose measurements would result. Second, the FOC dosimetry system has an energy dependence that results in a greater response with increasing x-ray beam energies; this suggests that it may under-respond to scattered radiation. This would also result in lower measured values than simulated values. Third, there are local quasi-periodic dose distributions present in MDCT scanning. These distributions are discussed further in Chapter 5, but for scans using pitch 1, overbeaming

results in periodically occurring higher dose values along the z-axis that can increase the possible range of measured values when using point dosimetry. The uncertainty in point measurements due to these dose distributions is large enough to account for the discrepancies between average organ dose values taken from point dose measurements and simulated average organ doses. These local periodic dose distributions also indicate that it is more likely to measure point doses lower than the average value within a region. Finally, the normalization factors used in the simulation to convert from photons to mAs were those calculated by Staton et al.⁵⁸ The measurements used to derive the normalization factors were performed using a different x-ray tube than that used for the phantom measurements in the abdomen/pelvis study.

Detector Collimation Width Comparison

Figure 4-1 and Figure 4-2 illustrate the simulated dose savings to organs and locations within the user planned scan range when using a larger detector collimation width. The effects of overranging are also evident outside the user planned scan range. These effects agree with those observed for the physical phantom measurements considered in Chapter 3. Figure 4-3 shows the ratio of corresponding average organ doses calculated for each detector collimation width. Figure 4-3 helps quantify the simulated dose savings due to using a larger detector collimation width. Again, this agrees well with the comparable Figure 3-7 in Chapter 3. The average of these ratios for simulated average organ doses was 0.92, and the average of these ratios for measured values was 0.91. Both simulated and measured data suggest dose savings of about 9% to tissues located within the user planned scan range when using the 24 mm detector collimation width in place of the 12 mm detector collimation width with other factors being equal.

Conclusions

This chapter demonstrates how physical phantoms can be used to validate computational phantoms and vice versa. Disagreements that occur between simulated and physically measured average organ doses serve to identify aspects of a study that need modification. After several iterations and subsequent adjustments, physically measured and simulated data should become increasingly closer, and increasingly reliable. Another benefit of having a computational “twin” phantom when performing a physical study is that the one has the option to use simulated average organ doses. By comparing easily measured organ doses (i.e. smaller organs within the user planned scan range), one can see how the simulated data compares against the physical data. Those average organ doses more difficult to physically measure, that require more assumptions (e.g. skin, bone surface, small intestine), can be replaced with those taken from a computational phantom. Using the most reliable organ dose measurements from both types of phantoms should result in more dependable risk assessment studies.

Table 4-1. Comparison of simulated and measured organ doses (mGy) for detector collimation widths of 16×0.75 mm (12 mm) and 16×1.5 mm (24 mm). Organs located within the user planned scan volume are in bold.

Organ/Tissue	12 mm Detector Collimation			24 mm Detector Collimation		
	Measured Organ Dose	Simulated Organ Dose (%RE)	% Difference	Measured Organ Dose	Simulated Organ Dose (%RE)	% Difference
Brain	0	0.01 (14.95)		0	0.01 (14.45)	
Extrathoracic Region	0	0.03 (14.11)		0	0.05 (11.17)	
Salivary Glands	0	0.04 (13.97)		0	0.06 (12.02)	
Thyroid	0	0.14(16.18)		0	0.20 (16.25)	
Esophagus	1.82	2.23 (2.31)	-20.0	1.90	2.53 (2.16)	-28.6
Thymus	0	0.23 (10.48)		0	0.30 (8.92)	
Lung	3.74	2.95 (0.56)	23.5	3.62	3.47 (0.51)	4.2
Heart	6.89	4.11 (0.98)	50.6	6.66	5.13 (0.86)	26.0
Liver	9.22	9.28 (0.50)	-0.6	8.52	8.67 (0.51)	-1.7
Spleen	9.32	10.11 (0.91)	-8.1	8.34	9.48 (0.92)	-12.8
Stomach	11.19	12.41 (0.77)	-10.3	10.46	11.24 (0.79)	-7.2
Adrenals	8.40	9.08 (2.11)	-7.7	7.70	8.41 (2.15)	-8.8
Pancreas	9.76	11.43 (1.17)	-15.7	8.91	10.20 (1.21)	-13.4
Gall Bladder	12.36	11.11 (1.49)	10.6	10.28	10.46 (1.49)	-1.7
Kidneys	10.47	11.45 (0.67)	-8.9	9.48	10.15 (0.70)	-6.8
Small Intestine	11.80	14.46 (0.36)	-20.3	10.76	12.98 (0.37)	-18.7
Colon	11.77	12.73 (0.39)	-7.8	11.00	11.50 (0.40)	-4.4
Bladder	9.00	8.42 (1.13)	6.6	8.23	7.50 (1.18)	9.3
Prostate	8.50	9.65 (2.08)	-12.6	7.75	9.20 (2.13)	-17.1
Testes	4.14	11.86 (1.65)	-96.5	10.08	19.79 (1.51)	-31.1
Skin	5.95	2.35 (0.14)	86.9	5.00	2.26 (0.14)	75.5
Bone Surface	3.64	7.73 (0.20)	-72.0	3.32	7.31 (0.20)	-75.0
Muscle	3.74	4.00 (0.13)	-6.8	3.40	3.91 (0.13)	-13.7

*Simulated dose data received from Choonsik Lee.

Table 4-2. Comparison of the contributions to effective dose (mSv) for detector collimation widths of 16×0.75 mm (12 mm) and 16×1.5 mm (24 mm) from the organs considered in both the simulated and physically measured studies.

	12 mm Detector Collimation			24 mm Detector Collimation		
	Measured Effective Dose	Simulated Effective Dose	% Difference	Measured Effective Dose	Simulated Effective Dose	% Difference
All tissues with simulated data	5.2	6.0	-14.3	5.3	5.8	-9.0
Only tissues within user planned scan range	4.1	4.4	-7.1	3.8	4.0	-5.1

*Tissues not considered: breast, bone marrow, oral mucosa, lymphatic nodes

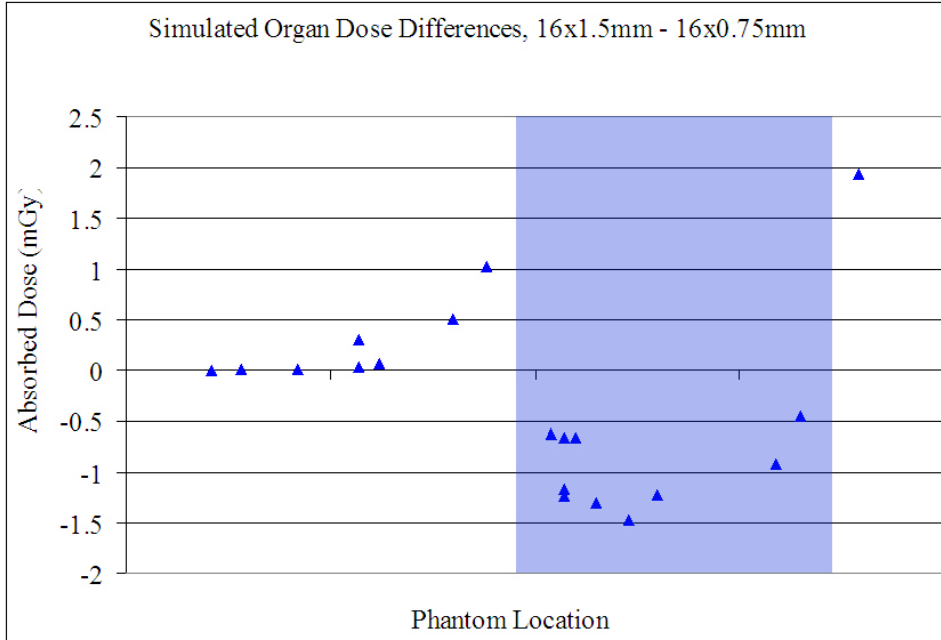


Figure 4-1. Differences in corresponding simulated average organ dose measurements for detector collimation widths of 16×1.5 mm (black) and 16×0.75 mm (red). Imaged scan range is indicated by the blue region.

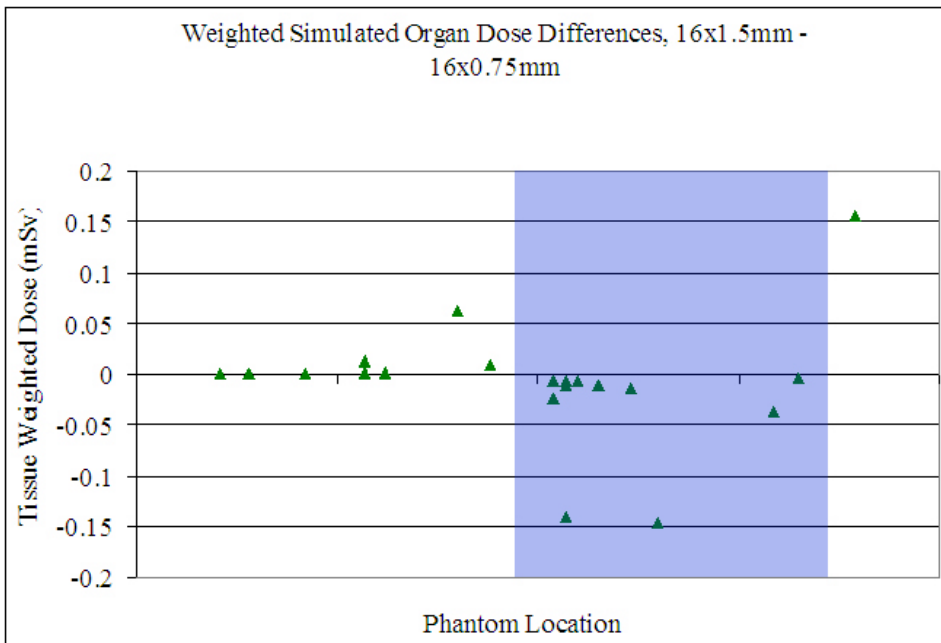


Figure 4-2. Differences in weighted simulated average organ dose measurements for detector collimation widths of 16×1.5 mm (black) and 16×0.75 mm (red). Imaged scan range is indicated by the blue region.

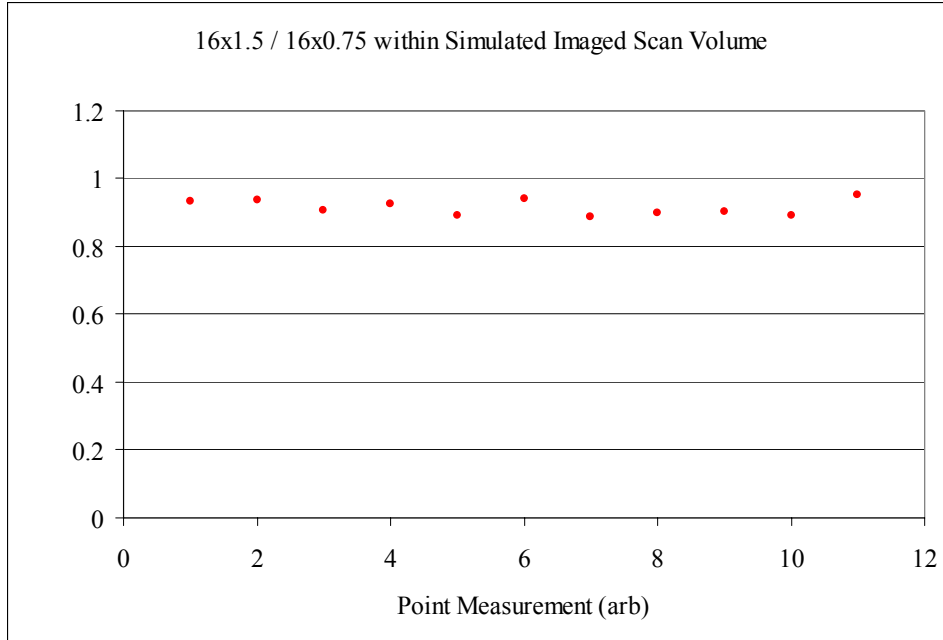


Figure 4-3. Ratio of corresponding simulated average organ dose measurements for 16×1.5 mm and 16×0.75 mm detector collimation width within the user-planned scan range

CHAPTER 5
TEMPORAL/SPATIAL MODULATION OF DOSE IN MDCT

Introduction

In MDCT, variations of z-axis (i.e. the axis parallel to table travel) doses in phantoms are caused by overscanning resulting from using pitch values less than one, underscanning resulting from using pitch values greater than one, amount of overbeaming, and detector collimation width. More specifically, doses within those regions where primary beam overlaps occur during helical scanning (pitch ≤ 1) are greater. Axially, dose rate is not constant over the gantry rotational period. This is primarily due to varying x-ray attenuation through the phantom, and secondarily to beam divergence. The greatest dose rate occurs when the x-ray tube position is nearest to the point dosimeter.⁶¹⁻⁶³ At any moment in time during a helical scan, regions within a phantom that are closer to the x-ray tube position will have a higher dose rate than those regions farther away. “Gaps” at the surface of a phantom in primary beam exposure that occur during helical scanning (pitch > 1) result in lower doses in those regions. Resulting cumulative dose distributions at peripheral locations due to helical scanning are locally periodic in space with a fundamental period equal to the table translation per rotation, which will depend on pitch and detector collimation width. Shape and amplitude of these quasi-periodic distributions of dose are functions of pitch, detector collimation width, the amount of overbeaming, and the attenuation due to the anatomy within that region of a phantom. The phase of these dose distributions is a function of activated x-ray tube starting angle and the starting edge of a scan.

Dixon et al. has derived mathematical expressions for accumulated dose distributions delivered in helical CT scans in cylindrical dosimetry phantoms, including the quasi-periodic dose distributions on the peripheral phantom axes.⁶¹⁻⁶³ Theirs is one of the few sources of information in the literature involving the dose distribution in peripheral phantom locations due

to helical CT. The fundamental period of these dose distributions is equal to the table translation per gantry rotation. These expressions are based on a mathematically derived single axial dose profile. Although these expressions describe the oscillations in dose in peripheral axes, they are valid for cylindrical phantoms only. Also, the analysis by Dixon et al. focuses on compensating for these peripheral dose distributions in calculating average dose to tissue in its application to CTDI type measurements. Potential dose savings to radiosensitive tissues and the quasi-periodic dose distributions in anatomical phantoms are not considered.

The first reason to consider these modulations of dose is that point dose measurements are often used in evaluating the dose to regions within a phantom during MDCT scanning. The magnitudes and extents of these modulations should be more clearly understood before utilizing point dose measurements to ascertain typical or average doses to regions within a phantom. The second reason these modulations should be better understood is that it may be possible to manipulate the technique settings for MDCT scans to minimize absorbed doses to more radiosensitive organs/tissues. This would be similar to, but more complicated than, reducing the breast dose received during radiography by acquiring posterior-anterior (PA) images instead of anterior-posterior (AP) images. A major advantage of manipulating the phase of peripheral quasi-periodic dose distributions by adjusting x-ray tube starting angles in order to achieve dose savings to especially radiosensitive tissues is that it would presumably not affect image quality.

The following discussion describes the extent and relative magnitudes of the dose modulations present in MDCT, and how they depend on technique settings. Also, the potential dose savings to specific radiosensitive organs/tissues is also quantified. The following describes an analysis for modeling the dose distributions at peripheral locations within a phantom due to helical MDCT scanning based on measured axial dose profiles.

Materials and Methods

For this study, a Siemens SOMATOM Sensation 16 helical MDCT scanner and an adult anthropomorphic phantom from the UF phantom series (GatorMan) were used for all scans. In addition, the plastic scintillator FOC dosimetry system described in Chapter 1 was used to record dose measurements. In this chapter, data sets and plots were normalized to better allow comparisons of magnitude.

Locations considered were those that included small volume superficial radiosensitive organs/tissues most likely to be affected by the modulations of dose described previously. Organs/tissues studied were the lens of the eye, thyroid, stomach, and testes. Although it might be possible to decrease breast dose by shifting the phase of the modulation of dose, breast tissue was not studied because it is larger than the other organs/tissues studied, and was not one of the tissues segmented in the CT data set used.

Temporal Modulation of Dose

Dose rate at a point during an axial scan

The first step in evaluating the temporal modulation of dose was measuring the temporal dose response at a point within the phantom during an axial scan. This data illustrates the differences in dose delivered to a point within a time interval (dose rate) at a particular time during a single gantry rotation; this dose is the result of the primary beam as well as scatter from the primary beam. Single axial scans were recorded with the FOC dosimetry system while using the following techniques: 12×1.5 mm (feed 18 mm), 9 mm reconstruction slice width, scan time 0.75 s, 130 mAs, 120 kVp, CAREdose4D (Siemens ATCM) OFF, 1 scan, 2 images. The tip of the FOC dosimeter was placed at the center of the organ/tissue location, and FOC time reading intervals were set to 0.01 s. These measurements were repeated and normalized for the eye, thyroid, stomach, and testes. An advantage of using a measured axial profile is that the axial

attenuation, x-ray beam spectrum, beam divergence, and geometry are accounted for. ATCM could also be used in acquiring these initial axial dose profiles.

Dose rate at a point during a helical scan

To model (only) the dose rate at a point during a helical MDCT scan, the data measured from the axial scan was used as the basis for a periodic function that is used later in this analysis. This helical dose rate curve represents the change in dose rate received at a point due to the continual rotation of the x-ray tube in helical scanning. Normalized dosimeter responses were plotted as a function of arbitrary index i . The curve can represent different gantry rotation times by setting i equal to different time increments. For example, setting i equal to 0.01 s (the time intervals used with the FOC dosimeter during data acquisition) separates the peaks by 0.75 s; this represents a curve for a helical scan with a 0.75 s gantry rotation. Setting i equal to $0.01 \times (0.5/0.75)$ s separates the peaks of the curve by 0.5 s; this represents a curve for a helical scan with a 0.5 s gantry rotation. Equation 5-1 describes the relationship between the time increment (dt) represented by each index i , and the gantry rotation time (t_{rot}).

$$dt(s) = \left(\frac{t_{rot}(s)}{0.75(s)} \times 0.01(s) \right) \quad (5-1)$$

This function represents the dose rate at a point for a helical scan with a pitch of zero (i.e. no table translation). The table translation and beam width are accounted for in subsequent steps.

Cumulative Point Dose

Since the helical dose rate curve described previously was derived using both primary and scatter radiation, and since the scatter to primary ratio is relatively small at peripheral axes in a phantom⁶¹⁻⁶³, it was assumed that the cumulative dose to a point (g) during a helical MDCT scan would be well represented by the sum of a section of that curve that corresponded to the time the

point dosimeter was located within the primary beam of the x-ray tube.⁶¹ To accomplish this, the time (T) for a beam width (W) to pass the point dosimeter was calculated using Equation 5-2.

$$T(s) = \frac{\text{beam_width}(mm)}{\text{table_speed}(mm/s)} = \frac{W}{TS}(s) \quad (5-2)$$

The table speed (TS) can be derived for MDCT scans by using Equation 5-3.⁴²

$$TS(mm/s) = \frac{\text{pitch} \times \text{detector_collimation}(mm)}{\text{rotation_time}(s)} = \frac{p \times dc}{t_{rot}}(mm/s) \quad (5-3)$$

The number of time increments, and therefore indices, within T (N_T), is simply T divided by dt.

$$N_T = \frac{T}{dt} \quad (5-4)$$

The beam width (W) value used was that previously measured for the Siemens SOMATOM Sensation 16 helical slice MDCT.⁵⁸ If one assumes that the normalized magnitude of the beam profile is unity over the thickness W, and zero elsewhere, then the i^{th} value of T (i.e. T_i) can be described by Equation 5-5.

$$\begin{aligned} T_0 = T_1 = T_2 = \dots = T_N = 1 \\ T_{N+1} = T_{N+2} = \dots = T_\infty = 0 \end{aligned} \quad (5-5)$$

And so, the j^{th} value of cumulative point dose (g_j), which represents the sum of a section of the helical dose rate curve corresponding to the beam width, can be represented by Equation 5-6.

The j^{th} value indicates the relative degree with which the section of the curve was shifted within the helical dose rate curve (or conversely, the degree with which the phase of the helical dose rate curve was shifted).

$$g_j = \sum_{i=0}^{\infty} f_{i+j} \cdot T_i = \sum_{i=0}^{N_T} f_{i+j} \cdot 1 = \sum_{i=0}^{N_T} f_{i+j} \quad (5-6)$$

From this, one can normalize and plot the cumulative point dose against index j . Normalized cumulative dose to a point resulting from an MDCT scan can be plotted against distance instead of index j by using Equation 5-7.

$$x_axis(mm) = j \times dt \times TS \quad (5-7)$$

A plot of cumulative point dose versus distance provides the distribution of total dose within the region near the FOC dosimeter, and therefore within the organ/tissue being studied.

Total Dose to Radiosensitive Tissues

Since g is a measure of the cumulative dose to a point within a region near a radiosensitive organ/tissue, the normalized average organ/tissue dose can be quantified by averaging over all points within that radiosensitive organ/tissue. This was done for the lens of the eye, thyroid, stomach, and testes by summing over a section of g that corresponded to the length of each organ/tissue, while weighting the sum based on the distribution of mass within that organ/tissue. One can estimate how the total average organ/tissue dose will change depending on its location within the local dose distribution by comparing the sums of shifted weighted sections.

The distribution of mass within lens of the eye along the z -axis was approximated by using the chord lengths of a circle with a similar diameter (~ 10 mm).⁵⁷ Chord lengths were obtained using Equation 5-8.

$$chord_length = 2 \cdot \sqrt{r^2 - d^2} \quad (5-8)$$

Here, r is the radius of the circle, and d is the perpendicular distance from the chord to the center of the circle. The distributions of mass within the thyroid, stomach, and testes along the z -axis were obtained from the segmented CT data set used in creating the GatorMan physical phantom. Using ImageJ software (Version 1.34s, National Institute of Health, Bethesda, MD) substack select and analyze histogram functions, the number of pixels for a particular tissue type located

within each organ containing slice was compared to the total number of pixels for the entire organ. These mass distributions over length were recorded to contain the appropriate number of data points necessary to facilitate easier mathematics for series. The appropriate number of data points needed (N_{organ}) to plot the mass distribution in terms of the index j was obtained using Equation 5-9.

$$N_{organ} = \frac{organ_length(mm)}{TS(mm/s) \cdot dt(s)} \quad (5-9)$$

And so, the total organ/tissue dose (h_k) can be represented by Equation 5-10; M_{organ} is the organ/tissue mass distribution. The k^{th} value indicates the relative degree with which the organ was shifted within the local dose distribution (or conversely, the degree with which the phase of the local dose distribution was shifted).

$$h_k = \sum_{j=0}^{\infty} g_{j+k} \cdot [M_{organ}]_j = \sum_{j=0}^{N_{organ}} g_{j+k} \cdot [M_{organ}]_j \quad (5-10)$$

From this, one can normalize and plot the total organ/tissue dose against index k . Each value of h represents a possible total organ/tissue dose during a helical MDCT scan. The plot of normalized h indicates the dependence total organ/tissue dose has on the organ/tissue location with respect to the phase of the local dose distribution for the scan. The plot of the total organ/tissue dose is easier to appreciate when plotted against the shift in distance, instead of index k ; this can be accomplished by using Equation 5-7.

Starting Angle Study

The phase of local total dose distributions at organ/tissue locations being considered in this study are dependent on the starting edge of the scan in addition to the starting angle at which the x-ray tube in the gantry becomes activated. The starting edge of each MDCT scan was controllable at the user console by adjusting the user-planned scan range. The starting angle of

the activated x-ray tube during a helical scan was studied for MDCT scans. Five gadolinium based scintillator FOC dosimeters were placed at the periphery of the bore of a Siemens SOMATOM Sensation 16 helical MDCT scanner (at angles 0° , 72° , 144° , 216° , 288°). as shown in Figure 5-1 (PMT 1 is at 0°). The response from each dosimeter was recorded for 14 identical scans using the following scan settings: 120 kVp, 50 mAs, pitch 1, rotation time 0.5 s, CAREDOSE4D OFF, and 24 mm detector collimation width. The time interval used with the FOC dosimeter was 0.02 s. Because of beam divergence and beam angle, each dosimeter response would reach a maximum each time the rotating x-ray tube passed that dosimeter; another easily identifiable smaller local maximum was recorded when the rotating activated x-ray tube was across from each dosimeter. From the synchronized real-time plots of the FOC dosimeters, the approximate starting angle for the activated x-ray tube was determined for each run.

Sample Set of Total Point Dose Measurements

Two sets (13 each) of MDCT scans using pitch 1 and pitch 1.5 were taken over the GatorMan phantom. FOC measurements were taken at two superficial (~ 1 cm from the surface) locations near the chest of the phantom for each scan. The following scan settings were used: 120 kVp, 100 mAs, rotation time 0.5 s, CAREDOSE4D OFF, and 24 mm detector collimation width. The time interval used with the FOC dosimeter was 0.02 s. For each scan, the total point dose for each dosimeter was recorded.

Results

Temporal Modulation of Dose

Dose rate at a point during an axial scan

FOC real-time measurements were recorded and plotted for points within the lens of the eye, thyroid, stomach, and testes. The normalized plot of the axial dose profile to the eye is

shown in Figure 5-2. The time between the rise and fall of this plot was 0.75 s as expected. This plot indicates that the x-ray tube was activated at the 12 o'clock x-ray tube position (nearest to the eye dosimeter), circled around the head of the phantom, and returned to the 12 o'clock position before turning off. The FOC counts during maximum x-ray beam attenuation by the phantom were less than 5% of the peak measured counts for each organ/tissue considered.

Dose rate at a point during a helical scan

The curve for each organ/tissue location represents the dose in time at a point for a hypothetical helical scan with no table translation, or pitch 0. One such curve is shown in Figure 5-3. The number of periods had to be great enough to accommodate subsequent steps in this analysis (i.e. the steps accounting for beam width, table translation, and tissue weighting). The time dependant data plotted (as measured by the FOC system) in Figure 5-3 represents only rotation times of 0.75 s, and so the data from this figure was also plotted as a function (f) of an arbitrary index (i). For convenience, each data point from the FOC measurement (corresponding to 0.01 s) was given its own index.

The curve in Figure 5-3 represents the “instantaneous” dose received at a point located within the lens of the eye of the GatorMan phantom, while in the primary beam, during a helical MDCT scan for an arbitrary gantry rotation time. It is worth noting that the phase of this repeating curve is a function of the scan start position and the starting angle of the activated x-ray tube.

Cumulative Point Dose

The function g represents cumulative dose at a point after having been passed completely by a primary beam of width W, during a helical MDCT scan. The plot of normalized g represents the quasi-periodic dose distribution near the region of the organ/tissue along the z-axis. Again, the phase would be shifted by altering the starting edge of the scan volume and/or

by changing the activated x-ray tube starting angle. The plot of the dose distribution is also plotted against distance instead of index j . The plot of g near the region of the lens of the eye for beam widths both equal to (no overbeaming) and greater than (overbeaming) the detector collimation width for pitch 1 is located in Figure 5-4.

Axial dose profiles were measured within phantom locations representing the lens of the eye, thyroid, stomach, and testes. Following the procedure described previously, normalized total dose distributions at each tissue location were calculated and plotted for pitch values of 1 and 1.5, as well as for detector collimation widths of 24 mm and 40 mm. The beam width was assumed to be 4.3 mm wider than the detector collimation width.⁵⁸ This beam width was measured at FWHM, but was treated as a full maximum width in these calculations in order to avoid underestimating the time a point is exposed to the primary beam in higher pitch scans (the scenario most likely to be used for organ/tissue dose reduction). Figure 5-5 through Figure 5-8 illustrate the local total dose distributions within a region expected for different tissue locations, detector collimation widths, and pitch values. Each plot in these figures has been normalized against its own maximum value. Therefore, each plot has a maximum value of one, and magnitudes between plots can not be directly compared in these figures. The relative variability can be compared between plots. Also evident from the methodology, Figure 5-5 through Figure 5-8, and an intuitive understanding of MDCT, the period of the local total dose distribution is equal to the pitch times the detector collimation width (i.e. the table translation per gantry rotation). The period lengths for collimation 24 mm, and pitch 1 and pitch 1.5 are 24 mm and 36 mm, respectively. Similarly, the period lengths for collimation 40 mm, and pitch 1 and pitch 1.5 are 40 mm and 60 mm, respectively. The phase as plotted for each total dose distribution at a

point is arbitrary and would depend upon the starting location of the scan as well as the angle at which the x-ray tube is activated.

These figures represent the possible range and likelihood of total point dose measurements for given scan parameters. As expected, the range in magnitude of total point dose measurement values increased with pitch. The range of possible point dose measurement values in the plots for pitch 1 is due exclusively to overbeaming. Figure 5-4 illustrates that setting the beam width equal to the detector collimation width in this model eliminates the variability for scans using pitch 1.

Table 5-1 provides the maximum values, minimum values, range, average values, and standard deviations of the normalized locally periodic dose distributions for each combination of organ/tissue, detector collimation width, and pitch. The values for each particular organ/tissue were normalized using the overall maximum value for that organ/tissue (this is different from Figure 5-5 through Figure 5-12). This maximum value occurred during pitch 1 and detector collimation of 24 mm for each organ/tissue location. Also provided are the minimum and average values renormalized against the maximum values of the corresponding pitch and detector collimation width (displayed as a percentage). Average values were taken over a single period for each curve. Values for each organ/tissue location can be compared directly. In addition to the relationship between total point dose and that point's location relative to the phase of the local dose distribution present in helical MDCT, average values can be directly compared to identify trends in total dose to a point with pitch and detector collimation width. The average value is an indication of the typical point dose measurement value expected for a point dosimeter in helical MDCT. The standard deviation and range are measures for the distribution (variability) of possible total point dose measurements.

Table 5-3 lists the ratio of the normalized total point dose at each organ/tissue location between pitch 1.5 and pitch 1 for the averages for the two detector collimation widths considered. The values for this ratio range from 0.65 to 0.67, with an average of 0.665. Table 5-4 lists the ratio between the normalized total point dose averages for detector collimation 40 mm and those for detector collimation 24 mm. The values for this ratio range from 0.93 to 0.96, with an average of 0.939.

Total Dose to Radiosensitive Tissues

The plot of normalized organ/tissue mass distributions is shown in Figure 5-13. Figure 5-9 through Figure 5-12 show the degree of variation in total organ/tissue dose depending on the organ's location with respect to the phase of the local total dose distribution present in helical MDCT. These differences in total organ/tissue dose are governed by the location of the x-ray tube as the primary beam passed by the organ/tissue during an MDCT scan. Generally, as the pitch and the detector collimation width increased, the range in magnitude of possible total organ/tissue dose increased. The way to interpret these figures is that each point on each plot represents a possible total organ/tissue dose that depends exclusively on where the organ/tissue is located with respect to the phase of the local dose distribution; the amplitude of these periodic curves indicates the variability of the total organ/tissue dose as well as the potential to minimize total organ/tissue doses by manipulating the phase of the local dose distribution.

Table 5-2 provides the maximum values, minimum values, range, average values, and standard deviations of the normalized total organ/tissue dose for each combination of organ/tissue, detector collimation width, and pitch. The values for each particular organ/tissue were normalized using the overall maximum value for that organ/tissue (this normalization differs from that used in Figures 5-5 through Figure 5-12). This maximum value occurred during pitch 1 and detector collimation 24 mm for each organ/tissue location. Also provided are the

minimum and average values renormalized against the maximum values of the corresponding pitch and detector collimation width (displayed as a percentage). Average values were taken over a single period of each curve. Values for each organ/tissue can be compared directly. In addition to the relationship between total organ/tissue dose and an organ's location relative to the phase of the local dose distribution present in helical MDCT, the values for each organ/tissue can be directly compared to identify trends in total organ/tissue dose with pitch and detector collimation width. The average value is an indication of the typical total organ/tissue dose expected in helical MDCT. The standard deviation and range are measures of the distribution of possible total organ/tissue doses.

Starting Angle Study

Figure 5-14 shows the FOC dosimeter plots for one of the sets of data taken. It is clear that in this case, PMT 5 was the first dosimeter passed by the activated x-ray tube, followed sequentially by the other dosimeters. The first dosimeter passed was recorded for each of the 14 sets of data and the tally is shown in Table 5-5. The starting angle of the x-ray tube was determined to be unpredictable, but not necessarily perfectly random.

Sample Distribution of Total Point Dose Measurements

The normalized average, standard deviation, and minimums were calculated for the two sets of FOC measured data acquired at pitch 1 and pitch 1.5. Table 5-6 and Table 5-7 compare these measured values against the calculated values found in Table 5-1.

Discussion

One aspect of this study was to attempt to quantify the quasi-periodic local dose distribution present within patients/phantoms undergoing MDCT scans. Another was to evaluate whether these dose distributions could be shifted to reduce the dose to especially radiosensitive organs/tissues. There are some additional results worth noting. Data calculated using the

methodology derived in this chapter agrees with theoretical expectations for the relationship between dose and pitch⁴², the relationship between dose and overbeaming described in Chapter 3, and point dose measurements using an FOC dosimetry system and anthropomorphic phantom.

In Figure 5-4, the plot showing the resulting local dose distribution when the beam collimation width is equal to the detector collimation width is a constant value. This was expected, and implies that the mathematics used was correct. The curves in Figure 5-5 and Figure 5-7 have a flat minimum feature that is consistent with the thought that overbeaming is responsible for the local dose distribution present in scans using pitch 1. Overbeaming would increase the dose where an overlap of the primary beam occurs between gantry rotations. And so, the intermediate regions between these overlaps should be a minimum value reflective of an MDCT without overbeaming (i.e. flat). Dixon et al. shows similar results for peripheral axes in a phantom.^{69, 70} The curves in Figure 5-6 and Figure 5-8 have a flat maximum feature consistent with an understanding of using pitch values greater than one. Pitch values greater than one should result in gaps between x-ray tube rotations that result in lower total dose values at superficial points in a phantom. Regions between these gaps should have relatively constant values. Also, tissue dose savings due to increasing pitch (while holding other parameters constant) is expected to be proportional to 1/1.5, or 0.67.⁴² This value is nearly identical to the values found in Table 5-3 for all organs/tissues and both detector collimation widths.

If Equation 3-3 is adjusted for the fact that the beam width considered represents a width at full max (i.e. the penumbra for the beam modeled in this chapter are twice as great as that used to derive Equation 3-3), the resulting Equation 5-11 can provide a value for the expected dose decrease due to overbeaming when changing detector collimation widths.

$$P_{sc} = \frac{LC + 2x}{LC + \frac{LC}{SC} \cdot (2x)} \quad (5-11)$$

Using 4.3 mm in place of 2x, 24 mm in place of SC, and 40 mm in place of LC, Equation 5-11 yields 0.94. This value agrees well with those measured values in Table 5-4.

Finally, Table 5-6 and Table 5-7 list the individually normalized average, minimum, and standard deviation values for total point dose at each organ/tissue location considered using the methodology mentioned previously. The same metrics are provided for two sets (one using pitch 1, and another using pitch 1.5) of FOC dosimetry measurements at superficial locations within the GatorMan phantom. It is clear that the measured values reflect the same trends and magnitudes as the modeled values.

Cumulative Point Dose Measurements

The variability of cumulative dose at a point within MDCT scans as shown in Table 5-1 should be considered when taking point dose measurements within a phantom; more point-like dosimeters are more subject to the periodic nature of dose distributions in helical CT. Dosimeters that might be subject to dose distribution amplitude variability would include TLDs, OSLs, FOC fibers, and MOSFETs. As expected, the minimum values associated with pitch 1 scans are approximately equal to maximum values for pitch 1.5 scans. It is important to realize that the difference in total point dose measurements, at identical locations, between scans using different pitch values can span from almost zero to the sum of the expected ranges for each scan. For example, comparing point dose measurements at the lens of the eye for detector collimation 24 mm between pitch 1 and pitch 1.5 might indicate a 0.01 difference (normalized to one) up to a 0.65 difference, despite the difference in averages being 0.29. Another issue with using point dosimeters in MDCT pitch studies is that image noise increases with increased pitch, and tube current is typically increased to maintain the image noise levels associated with lower pitch values.^{29, 33} This could lead to circumstances where measurements indicate a higher total dose at

a point for greater pitch value scans, even if the average of the higher pitch scan were actually lower.

This problem can be minimized by utilizing multiple dosimetry points to measure the dose within a particular region. Using multiple points would average out the maximum and minimum values. However, the success of this depends on the number of points used, and their placement. The fact that peripheral points within a phantom during helical MDCT have periodic dose distributions means that low resolution sampling of the dose (most likely) could result in dose measurement aliasing. For example, RANDO® and ATOM® phantoms are assembled in axial slices 2.5 cm thick and are often used with TLDs to measure dose to tissue.⁴¹ When the length of TLDs is not equal to the fundamental period of the dose distribution, dose measurement aliasing is possible. This minimum allowable distance between TLDs of 25 mm for these phantoms would not help average out the dose distribution for a 24 mm detector collimation width at pitch 1 because the period of the dose distribution (24 mm) aligns with (i.e. is in phase with) the separation of dosimeters (25mm). Alternatively, 25 mm between two dosimeters should work well for a 40 mm detector collimation width and a pitch of 1.25 because the period of the resulting dose distribution would be 50 mm. Here, the first dosimeter would be measuring a peak within the dose distribution as the next dosimeter was measuring a valley. This situation is not ideal if a third dosimeter in a contiguous section was also used for averaging because there would now be unequal contributions from peaks and valleys within the local dose distribution. These considerations should all be made when using small point dose measurements to represent some sort of average tissue dose at a particular location within a phantom. Because of potential aliasing, using additional dosimetric points, while ignoring the periodic nature of peripheral dose along the z-axis, will not necessarily produce more reliable measurements. It may be possible to

use a longer space integrating dosimeter instead of multiple point measurements. For example, a length of scintillating fiber used in an FOC system might avoid any aliasing in measuring dose in a helical scan dose distribution. Lengths of scintillating tips with magnitudes similar to the lengths of table translation per gantry rotation would be expected to produce responses representative of actual average organ/tissue doses.

Another way to minimize the variability in point dose measurements within a phantom is to run multiple MDCT scans. One concern with this method is that the starting angle of the activated x-ray tube must be perfectly random. The Siemens SOMATOM Sensation was found to have an unpredictable activated x-ray tube starting angle, but not necessarily perfectly random. If the starting angle for a particular MDCT scanner is not random, or even has preferred starting locations, dose distributions may not trend toward being averaged out by using multiple scans because the phase of these distributions would not be randomly aligned. The standard deviations listed in Table 5-1 could be used to relate the number of scans taken with the expected variability of point measurements.

The magnitudes of these inherent uncertainties for point dose measurements are large enough to account for the discrepancies in dose between the measured organ doses in Chapter 3 and simulated organ doses in Chapter 4. Moreover, the dose distributions discussed in this chapter may also explain the tendency for point dose measurements taken in Chapter 3 to be lower than the simulated average organ doses from Chapter 4. Figure 5-5 shows the dose distribution for pitch 1 and a detector collimation width of 24 mm. Only regions including overbeaming would record higher than average point doses, and other regions would record lower than average point doses. If one considers Figure 5-5 as a probability distribution for

possible point dose measurements, very few measurements would record the average dose, and the majority of measurements would record values lower than average.

Total Dose to Radiosensitive Tissues

With the exception of studies involving the use of selective in plane shielding, tissue radiosensitivity is not normally focused on when contemplating reductions in radiation dose to patients. Very recently, vendors have been investigating techniques such as adjusting the tube current during MDCT scans to reduce the dose to superficial tissues such as the breast. However, traditional dose reduction strategies such as adjusting mAs, kVp, and ATCM do not focus on specific tissues that are especially radiosensitive. Selective in-plane shielding usually includes the use of thin sheets of flexible latex impregnated with bismuth and shaped to cover the eye lens, thyroid, or breast.^{29, 31, 32} However, these shields result in increased image noise and image artifacts near the shields. Their use is not generally recommended because the dose reductions can usually be achieved by decreasing the x-ray tube current, at the cost of a more uniformly noisy image, instead of an image with non-uniform beam hardening artifacts.²⁹ Despite a historical lack of emphasis on specific tissues, there is still interest in reducing the radiation dose to especially radiosensitive tissues during MDCT scans, just as there is interest in reducing breast dose in radiography by acquiring PA images.

This chapter investigated the possibility of reducing radiation dose to especially radiosensitive organs/tissues by shifting local dose distributions present during MDCT scans. Any dose reductions due to phase shifting of the dose modulation would come with no cost to image quality (holding other techniques constant). Table 5-2 shows the plausibility and expected magnitude of dose reduction to the lens of the eye, thyroid, stomach, and testes when manipulating the phase of the local dose distribution with respect to these organs/tissues. For the lens of the eye, 23% reductions from maximum doses, and 11% reductions from averages were

calculated for scans using pitch 1 and detector collimation of 24 mm. And by increasing the pitch to 1.5, a dose reduction of 46% from maximum was calculated.

A major factor in the potential dose reduction to organs/tissues is the size and distribution of the organ/tissue, which is why the stomach showed the least variability. The lens of the eye, thyroid, and testes are particularly suited for organ/tissue dose reduction by manipulating the phase of local dose distributions. Although not considered in this study, it is possible that breast dose reduction is possible for MDCT scanners with larger reconstruction slice capabilities. This technique would be even more effective in dose reduction to especially radiosensitive organs/tissues in pediatric patients because the relatively smaller size of their organs/tissues would better fit within the valleys of locally periodic MDCT dose distributions. Another instance where this technique might prove useful is during MDCT scanning of pregnant patients, which is sometimes necessary.²⁹ Fetal length during the first trimester (~5 cm and less) are short enough to potentially benefit from manipulating the phase of the z-axis dose distribution, although they are not as superficially located as the organs/tissues considered in this chapter. If the location of the fetus could be identified on the scout image, by using ultrasound, or some other method, then the fetus could be placed within a valley of a local dose distribution in order to reduce fetal dose.

This study shows that dose reductions to especially radiosensitive organs/tissues during MDCT scanning by shifting the phase of the local dose distribution are possible. Most importantly, these dose reductions would come at no cost in image quality (assuming no dependence of image quality on activated x-ray tube starting angle).

Conclusions

This chapter described a method to identify the relative magnitudes, amplitudes, shapes, and fundamental periods of the dose distributions within a phantom based on real-time axial

FOC dosimetric measurements. The reasoning is similar to Dixon et al.⁶¹ Quasi-periodic dose distributions present during MDCT scanning are a source of uncertainty when using point dosimeters. The uncertainty becomes significantly greater with increased pitch, and can be minimized by averaging over many carefully selected points or many scans. Potential total organ/tissue dose reduction was quantified; this reduction would result in no loss of image quality so long as image quality is not dependant on the x-ray tube starting angle. The dose reduction was more apparent in the lens of the eye and the thyroid, and this technique would be particularly suited for use with pediatric patients. Monte Carlo studies could be performed to further quantify or validate these dose reductions.

The obvious problem with this dose reduction technique is that this is not presently clinically applicable/available. There is no easily controllable way to align the x-ray tube rotation with patient organs/tissues. Vendors/manufacturers would have to incorporate a method of shifting the phase of the dose distribution. This could most likely be accomplished by adjusting existing or writing new software. Manufacturers could enable dose reduction to especially radiosensitive tissues by overlaying the x-ray tube path over the console scout image, and permit the shifting of the phase of this path by automatically changing the x-ray tube starting angle; the dose distribution valleys occur between gantry rotations for pitch greater than 1, and at the middle of the beam for pitch 1.

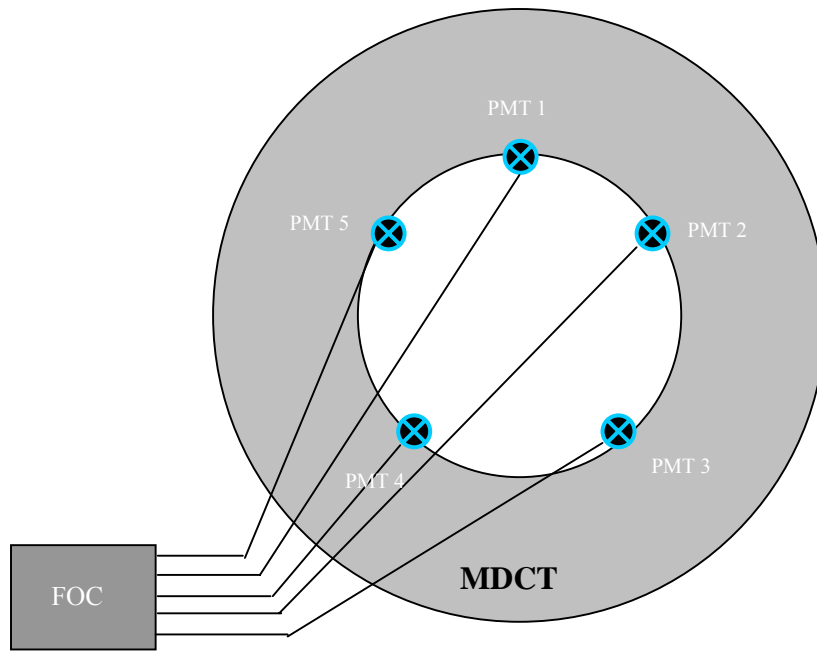


Figure 5-1. Schematic for the starting angle study.

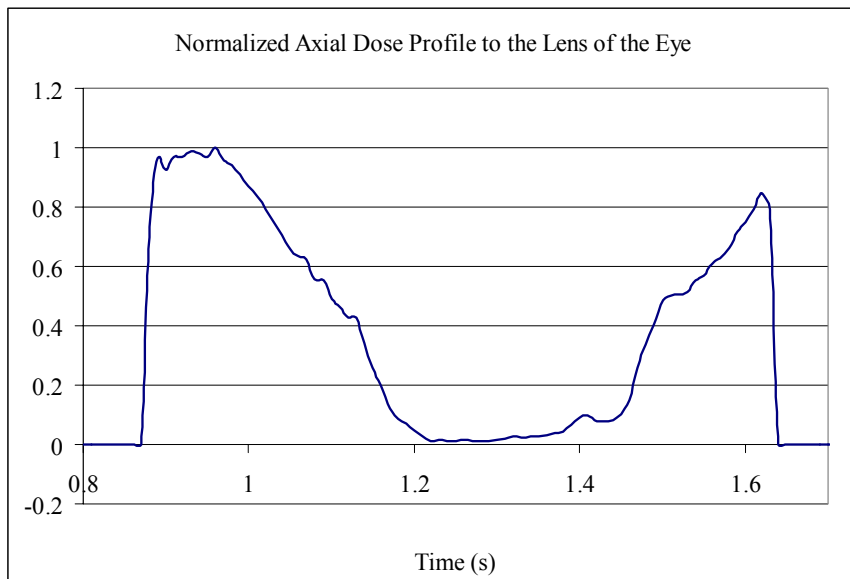


Figure 5-2. Normalized plot of FOC dosimeter counts received at a point located within the lens of the eye of the GatorMan phantom, in the center of the primary beam, during a single axial MDCT scan.

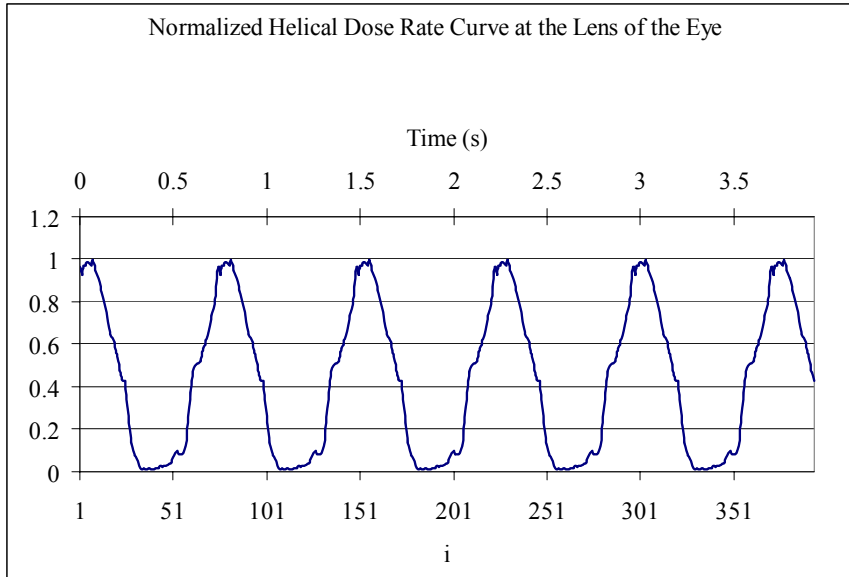


Figure 5-3. Axial-based normalized helical dose rate plot at a point located within the lens of the eye of the GatorMan phantom, while continuously in the primary beam, during a hypothetical helical MDCT scan with no table translation, plotted as a function of index i , and time.

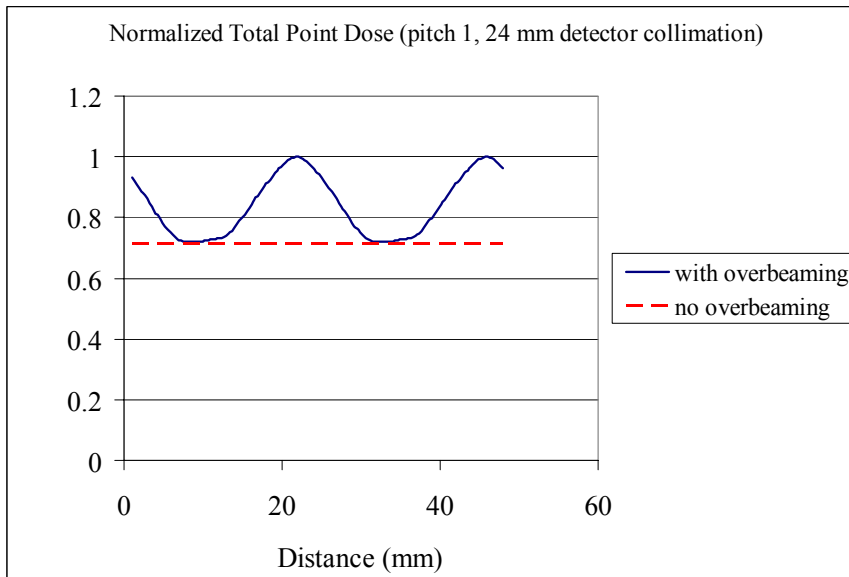


Figure 5-4. Total normalized point dose as a function of distance expected near the region of the lens of the eye for settings of pitch 1, detector collimation 24 mm, for a given x-ray tube starting angle and starting scan location. The blue curve represents the dose distribution that results when the beam width is 28.3 mm. The red curve results if the beam width was equal to the detector collimation (24 mm).

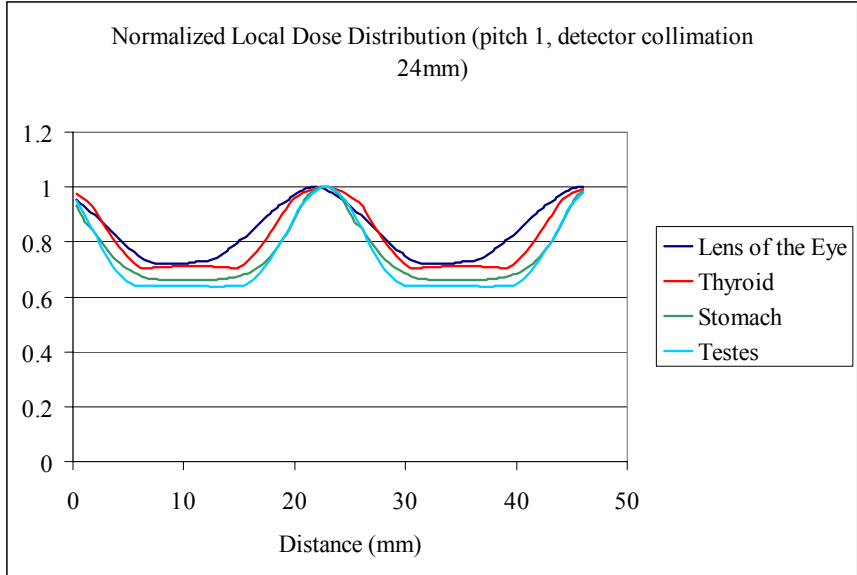


Figure 5-5. Total normalized point dose as a function of distance expected near different tissue locations for settings of pitch 1 and detector collimation 24 mm.

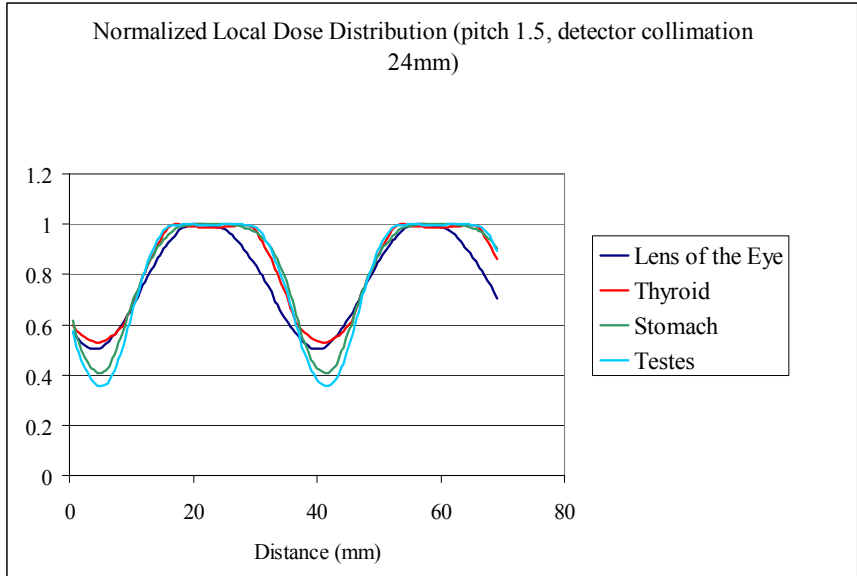


Figure 5-6. Total normalized point dose as a function of distance expected near different tissue locations for settings of pitch 1.5 and detector collimation 24 mm.

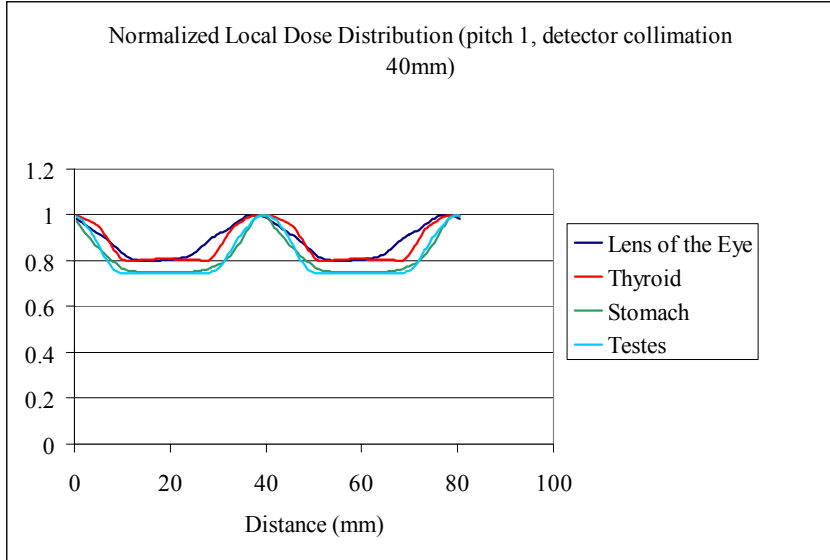


Figure 5-7. Total normalized point dose as a function of distance expected near different tissue locations for settings of pitch 1 and detector collimation 40 mm.

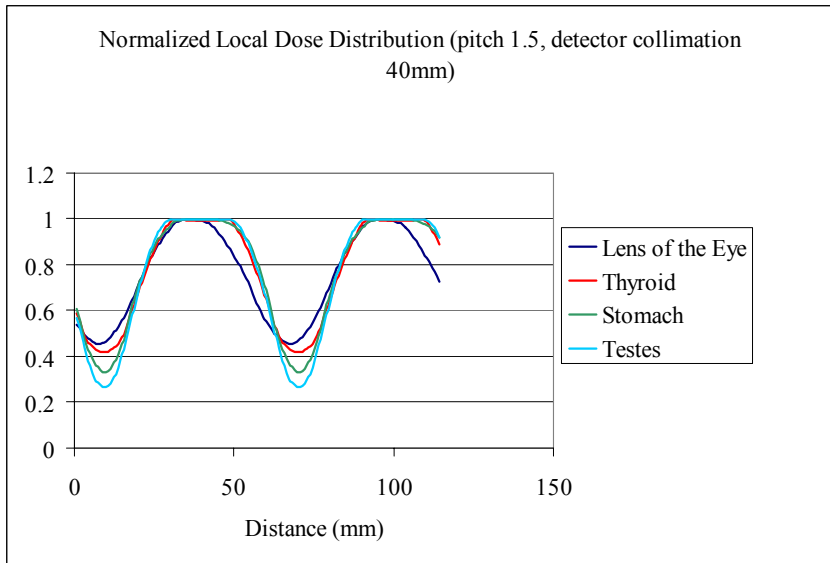


Figure 5-8. Total normalized point dose as a function of distance expected near different tissue locations for settings of pitch 1.5 and detector collimation 40 mm.

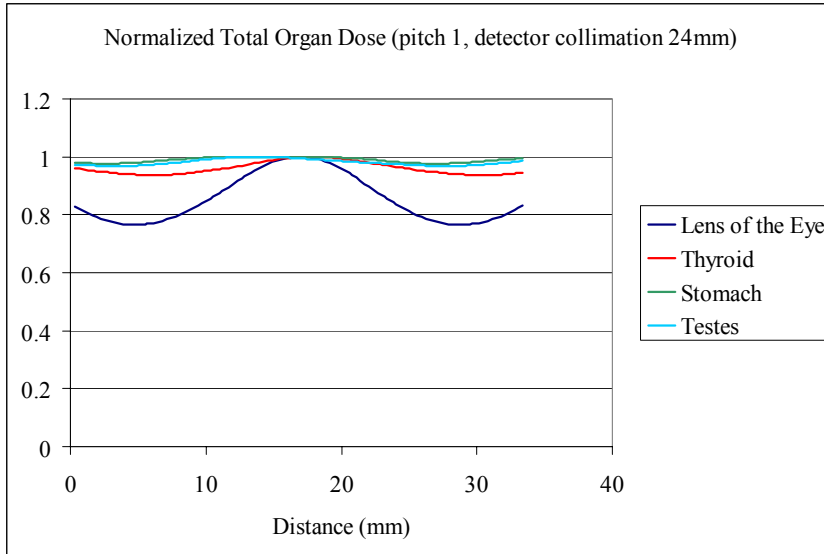


Figure 5-9. The degree of variation in total organ/tissue dose depending on the organ's location with respect to the point dose distribution for pitch 1 and detector collimation 24 mm.

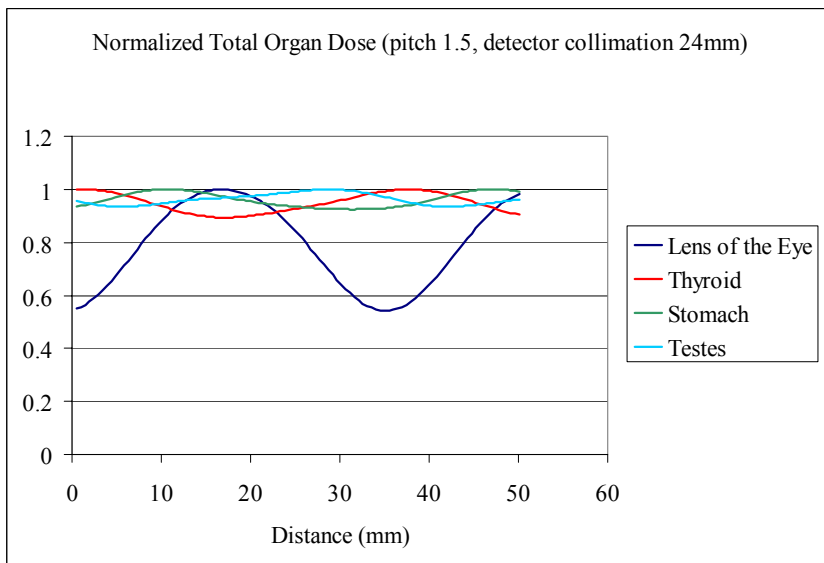


Figure 5-10. The degree of variation in total organ/tissue dose depending on the organ's location with respect to the point dose distribution for pitch 1.5 and detector collimation 24 mm.

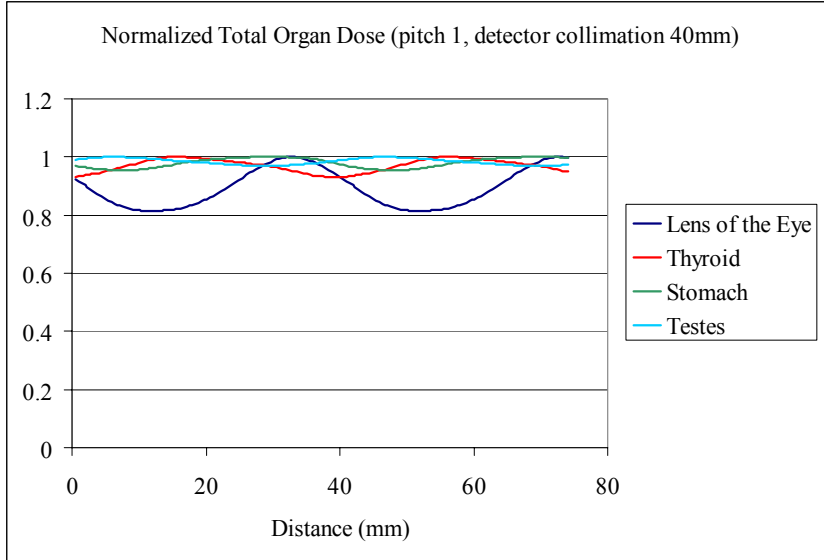


Figure 5-11. The degree of variation in total organ/tissue dose depending on the organ's location with respect to the point dose distribution for pitch 1 and detector collimation 40 mm.

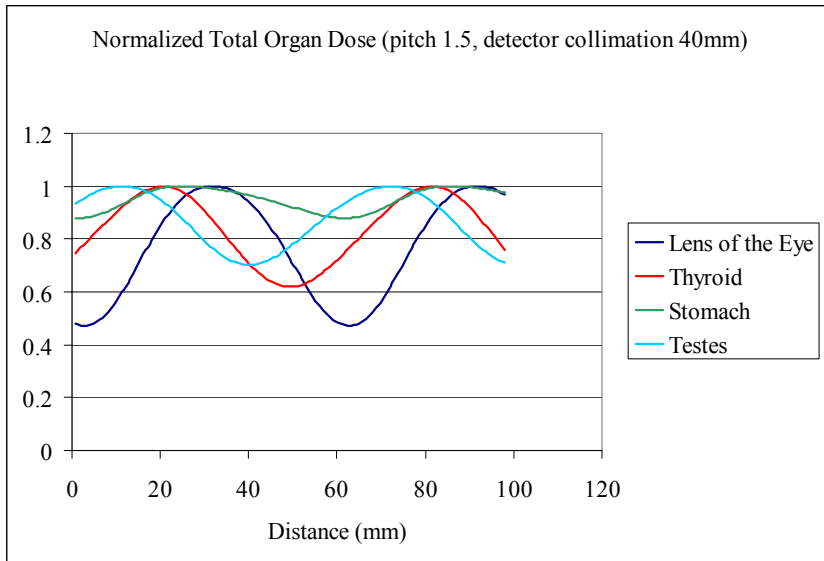


Figure 5-12. The degree of variation in total organ/tissue dose depending on the organ's location with respect to the point dose distribution for pitch 1.5 and detector collimation 40 mm.

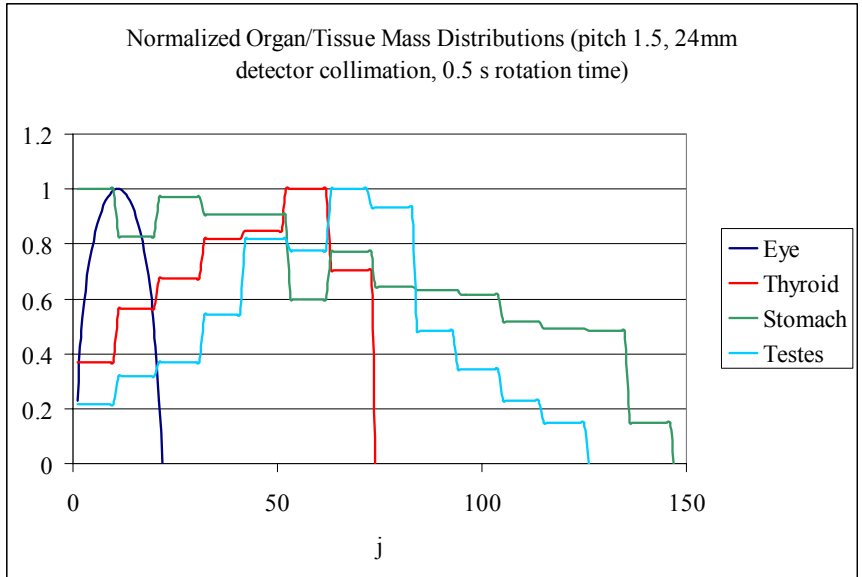


Figure 5-13. Normalized organ/tissue mass distributions plotted against index j corresponding to using a pitch 1.5, detector collimation 24 mm, and gantry rotation time 0.5s. The step pattern for the thyroid, stomach, and testes is due to deriving mass distributions from a segmented CT data set comprising 5 mm axial slices.

Table 5-1. Minimum values, maximum values, average values, and standard deviations for normalized point dose distributions.

	Lens of the Eye				Thyroid			
	24 mm		40 mm		24 mm		40 mm	
	Pitch 1	Pitch 1.5	Pitch 1	Pitch 1.5	Pitch 1	Pitch 1.5	Pitch 1	Pitch 1.5
Maximum	1.00	0.71	0.9	0.70	1.00	0.67	0.87	0.66
Minimum	0.72	0.35	0.72	0.32	0.70	0.36	0.70	0.28
Minimum (% of Maximum)	72%	50%	80%	46%	70%	53%	80%	42%
Range	0.28	0.36	0.18	0.38	0.30	0.31	0.17	0.38
Average	0.84	0.55	0.79	0.53	0.82	0.55	0.77	0.51
Average (% of Maximum)	84%	78%	88%	75%	82%	82%	88%	77%
Standard Deviation	0.10	0.13	0.06	0.14	0.12	0.12	0.07	0.15

Table 5-1. Continued

	Stomach				Testes			
	24 mm		40 mm		24 mm		40 mm	
	Pitch 1	Pitch 1.5						
Maximum	1.00	0.63	0.87	0.62	1.00	0.63	0.85	0.62
Minimum	0.66	0.26	0.65	0.21	0.64	0.22	0.63	0.17
Minimum (% of Maximum)	66%	41%	75%	33%	64%	35%	74%	27%
Range	0.34	0.27	0.22	0.41	0.36	0.41	0.22	0.45
Average	0.77	0.50	0.71	0.48	0.75	0.49	0.7	0.47
Average (% of Maximum)	77%	80%	82%	77%	75%	79%	82%	75%
Standard Deviation	0.12	0.13	0.07	0.15	0.13	0.15	0.08	0.17

*Values for each organ/tissue are normalized to the overall maximum value for that organ. Headings “24 mm” and “40 mm” refer to the detector collimation.

Table 5-2. Minimum values, maximum values, average values, and standard deviations of normalized total organ/tissue doses

	Lens of the Eye				Thyroid			
	24 mm		40 mm		24 mm		40 mm	
	Pitch 1	Pitch 1.5	Pitch 1	Pitch 1.5	Pitch 1	Pitch 1.5	Pitch 1	Pitch 1.5
Maximum	1.00	0.49	0.56	0.29	1	0.46	0.56	0.31
Minimum	0.77	0.26	0.45	0.14	0.94	0.41	0.52	0.19
Minimum (% of Maximum)	77%	54%	81%	47%	94%	89%	93%	62%
Range	0.23	0.23	0.11	0.15	0.06	0.05	0.04	0.12
Average	0.88	0.39	0.5	0.22	0.97	0.43	0.54	0.25
Average (% of Maximum)	88%	79%	90%	75%	97%	94%	97%	81%
Standard Deviation	0.08	0.08	0.04	0.06	0.02	0.02	0.01	0.04

Table 5-2. Continued

	Stomach				Testes			
	24 mm		40 mm		24 mm		40 mm	
	Pitch 1	Pitch 1.5						
Maximum	1	0.46	0.56	0.26	1	0.45	0.56	0.29
Minimum	0.98	0.42	0.53	0.23	0.97	0.42	0.54	0.2
Minimum (% of Maximum)	98%	92%	95%	88%	97%	93%	97%	70%
Range	0.02	0.04	0.03	0.03	0.03	0.03	0.02	0.09
Average	0.99	0.44	0.55	0.25	0.98	0.44	0.55	0.25
Average (% of Maximum)	99%	96%	98%	95%	98%	97%	98%	86%
Standard Deviation	0.01	0.01	0.01	0.01	0.01	0.01	0.01	0.03

*Values for each organ/tissue are normalized to the overall maximum value for that organ. Headings “24 mm” and “40 mm” refer to the detector collimation.

Table 5-3. Normalized total point dose average for pitch 1.5 divided by that for pitch 1
Pitch 1.5 / Pitch 1

	Lens of the Eye	Thyroid	Stomach	Testes
24 mm	0.66	0.67	0.65	0.66
40 mm	0.67	0.67	0.67	0.67

*Rows labels “24 mm” and “40 mm” refer to the detector collimation width. The expected dose savings to tissue by increasing pitch from 1 to 1.5 is

Table 5-4. Normalized total point dose average for detector collimation 40 mm divided by that for detector collimation 24 mm.
40 mm / 24 mm

	Lens of the Eye	Thyroid	Stomach	Testes
Pitch 1	0.94	0.93	0.93	0.93
Pitch 1.5	0.96	0.93	0.95	0.94

*Heading labels “24 mm” and “40 mm” refer to the detector collimation width.

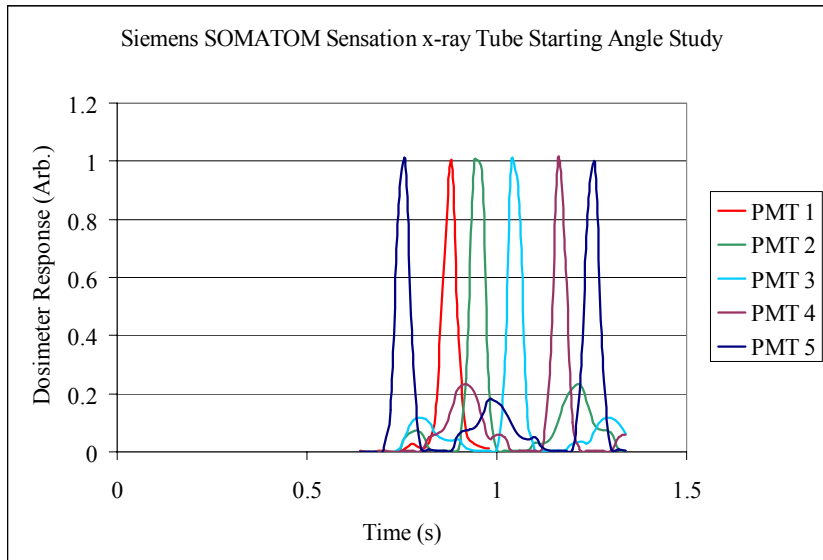


Figure 5-14. Synchronized FOC dosimeter responses used to determine the starting angle of the activated x-ray tube.

Table 5-5. Results for the MDCT starting angle study.

Number of Times First Exposed				
Dosimeter at ~0°	Dosimeter at ~72°	Dosimeter at ~144°	Dosimeter at ~216°	Dosimeter at ~288°
1	0	5	3	5

*Angles listed begin at the 12 o'clock position, and increase clockwise.

Table 5-6. Comparison of FOC measured and calculated total point dose metrics for pitch 1.

	FOC Measured	Lens of the Eye	Thyroid	Stomach	Testes
Maximum	1.00	1.00	1.00	1.00	1.00
Minimum	0.62	0.72	0.7	0.66	0.64
Range	0.38	0.28	0.30	0.34	0.36
Average	0.86	0.84	0.82	0.77	0.75
Standard Deviation	0.11	0.10	0.12	0.12	0.13

*Values are for 24 mm detector collimation.

Table 5-7. Comparison of FOC measured and calculated total point dose metrics for pitch 1.5.

	FOC Measured	Lens of the Eye	Thyroid	Stomach	Testes
Maximum	1.00	1.00	1.00	1.00	1.00
Minimum	0.45	0.50	0.53	0.41	0.35
Range	0.55	0.50	0.47	0.59	0.65
Average	0.71	0.78	0.82	0.80	0.79
Standard Deviation	0.18	0.18	0.18	0.21	0.24

*Values are for 24 mm detector collimation.

CHAPTER 6 A DOSIMETER RESPONSE WEIGHTED TECHNIQUE FOR MEASURING EFFECTIVE DOSE CONTRIBUTIONS

Introduction

Generally, phantom organ point dose measurements are made as a method of quantifying the risk due to a particular exposure. To assess that risk, the average of the point dose measurements for each organ are often used in conjunction with ICRP suggested tissue weightings to calculate the contribution from that organ to the effective dose for that radiation exposure.⁵ Although there are disadvantages, using effective dose is one of the best ways to assess and compare the risks due to many different kinds of exposures.

There are competing considerations with regard to the number of points used to measure average organ dose in phantoms. First is convenience, measuring greater numbers of points takes greater amounts of time. Second, measuring greater numbers of points improves the estimate of average organ dose. Third, measuring increased numbers of points increasingly interferes with the anatomy and attenuation characteristics of the phantom. A wide range of numbers of point dose measurements can be justifiably used to measure average organ dose.

TLD and OSL dosimeters are the most common dosimeters used in phantom studies. For effective dose calculations, TLD and OSL dosimeters are placed into phantom organ locations and exposed to radiation. While being removed, the organ location for each TLD (or OSL) must be catalogued and maintained throughout the reading process. Each group of TLDs (OSLs) representing an organ/tissue dose must be measured separately, and must be erased before reuse. The measured average dose values for each organ is then multiplied by its ICRP tissue weighting factor to calculate the contribution towards effective dose; this must be done for each type of exposure compared in a study. This process is very time consuming and tedious.^{15, 42}

Similarly, FOC dosimetry systems utilize point dose measurements to predict effective dose, and assess the risks due to particular radiation exposures. In these systems, the many point measurements are associated with an optical fiber. Each of these fibers carries photons that are ultimately counted by a PMT or CCD. The problem with using a PMT to measure the output from each fiber is that many simultaneous measurements require many PMTs, which becomes increasingly expensive. The bulk of such a system also increases as the number of PMTs is increased. Using a CCD for measuring the light output for each fiber is less costly, and is more receptive to making multiple simultaneous measurements. However, the time resolution and sensitivity for a CCD are worse than those for a PMT. CCD-based FOC systems are less capable of producing real-time measurements for MDCT scanning and are less able to use the less efficient water equivalent plastic scintillators.

The following is a more convenient and inexpensive theoretical alternative method of using phantom dosimetry to assess the risk due to radiation exposures.

Methods and Materials

TLDs and OSLs

In anthropomorphic phantom dosimetry, TLDs and OSLs are placed within specific locations representative of organs/tissues. The number of dosimeters used at each organ location can vary. If the dose response for each dosimeter within a particular organ/tissue location is $[D_T]_i$ and the number of dosimeters used for a particular organ/tissue is N_T , then the average dose to that organ, $\langle D_T \rangle$ is represented by Equation 6-1.

$$\langle D_T \rangle = \frac{\sum_{i=1}^{N_T} [D_T]_i}{N_T} \quad (6-1)$$

Notice that the sum in the numerator equals the sum of all the dosimeter response for that particular organ location. The contribution to the effective dose from this organ (E_T) would follow from Equation 1-5 and Table 1-1, where w_T is the tissue weighting factor, and is shown in Equation 6-2. The sum over all tissues would give the total effective dose. It is worth noting that ICRP 103 uses only five different values of weighting factors (see Table 1-1).⁵

$$E_T = w_T \cdot \langle D_T \rangle = w_T \cdot \frac{\sum_{i=1}^{N_T} [D_T]_i}{N_T} \quad (6-2)$$

Consider the contribution to effective dose from three different organs having three different tissue weighting factors (w_1, w_2, w_3), and three different numbers of total point dose measurements (N_1, N_2, N_3). The total contribution toward effective dose from these three organs, $E_{1,2,3}$, would be as shown in Equation 6-3.

$$\begin{aligned} E_{1,2,3} &= w_1 \cdot \langle D_1 \rangle + w_2 \cdot \langle D_2 \rangle + w_3 \cdot \langle D_3 \rangle \\ &= w_1 \cdot \frac{\sum_{i=1}^{N_1} [D_1]_i}{N_1} + w_2 \cdot \frac{\sum_{i=1}^{N_2} [D_2]_i}{N_2} + w_3 \cdot \frac{\sum_{i=1}^{N_3} [D_3]_i}{N_3} \end{aligned} \quad (6-3)$$

Factoring out w_1 gives Equation 6-4.

$$E_{1,2,3} = w_1 \cdot \left(\frac{\sum_{i=1}^{N_1} [D_1]_i}{N_1} + \frac{w_2}{w_1} \cdot \frac{\sum_{i=1}^{N_2} [D_2]_i}{N_2} + \frac{w_3}{w_1} \cdot \frac{\sum_{i=1}^{N_3} [D_3]_i}{N_3} \right) \quad (6-4)$$

Since there is an inherent flexibility in choosing the number of points used in determining an average organ dose, one can decide to use the number of point doses present in each organ as described in Equation 6-5.

$$N_2 = \frac{w_2}{w_1} \cdot N_1$$

$$N_3 = \frac{w_3}{w_1} \cdot N_1$$
(6-5)

Doing so leads to Equation 6-6.

$$E_{1,2,3} = w_1 \cdot \left(\frac{\sum_{i=1}^{N_1} [D_1]_i}{N_1} + \frac{w_2}{w_1} \cdot \frac{\sum_{i=1}^{N_2} [D_2]_i}{\frac{w_2}{w_1} \cdot N_1} + \frac{w_3}{w_1} \cdot \frac{\sum_{i=1}^{N_3} [D_3]_i}{\frac{w_3}{w_1} \cdot N_1} \right)$$
(6-6)

Clearly, the weighting factors in the second and third terms cancel. The N_1 can be factored out, resulting in Equation 6-7. Equation 6-8 represents the total dose measured from all the dosimeters used.

$$E_{1,2,3} = \frac{w_1}{N_1} \cdot \left(\sum_{i=1}^{N_1} [D_1]_i + \sum_{i=1}^{N_2} [D_2]_i + \sum_{i=1}^{N_3} [D_3]_i \right)$$
(6-7)

$$D_{1,2,3} = \left(\sum_{i=1}^{N_1} [D_1]_i + \sum_{i=1}^{N_2} [D_2]_i + \sum_{i=1}^{N_3} [D_3]_i \right)$$
(6-8)

FOC Dosimetry

A similar derivation can be made for an FOC dosimetry system that utilizes a scintillating fiber tip. As before, the number of point dosimeters used at each organ location can vary. Analogously, different lengths of scintillating tips can be used to measure the average organ dose for each organ location. If the response in counts from the FOC fiber within each particular organ/tissue location is C_T , and the count to dose conversion factor for that particular fiber is λ_T (which is a function of the length of the scintillating tip for each fiber), then the average dose to that organ, $\langle D_T \rangle$ is represented by Equation 6-9.

$$\langle D_T \rangle = \lambda_T \cdot C_T$$
(6-9)

The contribution to the effective dose from this organ (E_T) would follow from Equation 1-5 and Table 1-1, where w_T is the tissue weighting factor, and is shown in Equation 6-10. Again, the sum over all tissues would give the total effective dose.⁵

$$E_T = w_T \cdot \langle D_T \rangle = w_T \cdot \lambda_T(L_T) \cdot C_T \quad (6-10)$$

As before, consider the contribution to effective dose from three different organs having three different tissue weighting factors (w_1, w_2, w_3), using three different FOC fibers scintillating tip lengths, and three different count to dose conversion factors ($\lambda_1, \lambda_2, \lambda_3$). The total contribution toward effective dose from these three organs, $E_{1,2,3}$, would be as shown in Equation 6-11.

$$\begin{aligned} E_{1,2,3} &= w_1 \cdot \langle D_1 \rangle + w_2 \cdot \langle D_2 \rangle + w_3 \cdot \langle D_3 \rangle \\ &= w_1 \cdot \lambda_1 \cdot C_1 + w_2 \cdot \lambda_2 \cdot C_2 + w_3 \cdot \lambda_3 \cdot C_3 \end{aligned} \quad (6-11)$$

Factoring out w_1 gives Equation 6-12.

$$\begin{aligned} E_{1,2,3} &= w_1 \cdot \langle D_1 \rangle + w_2 \cdot \langle D_2 \rangle + w_3 \cdot \langle D_3 \rangle \\ &= w_1 \cdot \left(\lambda_1 \cdot C_1 + \frac{w_2}{w_1} \cdot \lambda_2 \cdot C_2 + \frac{w_3}{w_1} \cdot \lambda_3 \cdot C_3 \right) \end{aligned} \quad (6-12)$$

The count to dose conversion factor, λ_T , is a function of the length of the scintillating tip for each particular fiber. Correctly chosen lengths for each scintillating tip would lead to the relationships in Equation 6-13.

$$\begin{aligned} \lambda_2 &= \frac{w_1}{w_2} \cdot \lambda_1 \\ \lambda_3 &= \frac{w_1}{w_3} \cdot \lambda_1 \end{aligned} \quad (6-13)$$

Using these relationships leads to Equation 6-14.

$$E_{1,2,3} = w_1 \cdot \left(\lambda_1 \cdot C_1 + \frac{w_2}{w_1} \cdot \frac{w_1}{w_2} \cdot \lambda_1 \cdot C_2 + \frac{w_3}{w_1} \cdot \frac{w_1}{w_3} \cdot \lambda_1 \cdot C_3 \right) \quad (6-14)$$

Clearly, the weighting factors in the second and third terms cancel. The λ_1 can be factored out, resulting in Equation 6-15. Equation 6-16 represents the total counts from all fibers used.

$$E_{1,2,3} = w_1 \cdot \lambda_1 \cdot (C_1 + C_2 + C_3) \quad (6-15)$$

$$C_{1,2,3} = (C_1 + C_2 + C_3) \quad (6-16)$$

Results

The generalized form for Equation 6-7 for measuring effective dose while making a single TLD or OSL measurement is shown in Equation 6-17. Here, w_{ref} and N_{ref} are the reference weighting factor and reference number of dosimeters with which all other numbers of dosimeters will be scaled. The number of TLDs (OSLs) used in the n^{th} organ in order to use Equation 6-17 is shown in Equation 6-18.

$$E = \frac{w_{ref}}{N_{ref}} \cdot \sum_{All_tissues} \left(\sum_{i=1}^{N_n} [D_n]_i \right) \quad (6-17)$$

$$N_n = \frac{w_n}{w_{ref}} \cdot N_{ref} \quad (6-18)$$

The generalized form for Equation 6-15 for measuring effective dose using only the total counts measured from all FOC fibers is shown in Equation 6-19. Here, w_{ref} , and λ_{ref} are the reference weighting factor and reference count to dose factor, from which all other FOC fiber scintillating tip lengths will be determined. The scintillating tip lengths used for the FOC fiber in the n^{th} organ in order to use Equation 6-19 is shown in Equation 6-20.

$$E = w_{ref} \cdot \lambda_{ref} \cdot \sum_{All_tissues} (C_n) \quad (6-19)$$

$$\lambda_n = \frac{W_{ref}}{W_n} \cdot \lambda_{ref} \quad (6-20)$$

Discussion

The main advantage of measuring effective dose as described in Equation 6-17 and Equation 6-18 is that TLDs (OSLs) can be read simultaneously in a single measurement. Also, cataloging of the TLDs (OSLs) after a radiation exposure is now unnecessary because it is no longer required to know which TLDs (OSLs) came from which organ location. The tissue weighting is achieved physically by using different numbers of dosimeters in each organ location instead of weighting tissues computationally after organ measurements have been made. Individual average organ dose measurements are lost by using this technique; however, the risk associated with all organ locations is accounted for.

With the FOC dosimetry system, the tissue weighting would be achieved by using different lengths of scintillating tips for each FOC fiber. Effective dose can be calculated by measuring the total counts from all fibers. The major advantage of this is that by coupling optical fibers from different organs, as few as one PMT can be used to measure effective dose. This decreases the cost of FOC systems significantly. It also lessens the number of radiation exposures required to measure many organ doses, which would be particularly useful in lengthy exposures. Also, measuring effective dose as a function of a single count of photons allows one to plot the effective dose (or the contribution to effective dose from fewer organs) in real-time. In MDCT, this would be particularly interesting because one could effectively plot the overall risk due to a particular MDCT scan as a function of where the x-ray beam is located with respect to a patient.

This dosimeter response weighted technique is likely to be less straight forward to apply to FOC dosimetry in practice. First, FOC fibers for each organ location must be coupled in order to be summed. Fiber optic couplers for multiple fibers exist, but care must be taken to ensure that

the coupling does not non-uniformly attenuate the different fibers being coupled. It is also important that too much attenuation does not occur during coupling.

Second, the response from reference fibers will not necessarily be correctly weighted because the entire fiber is sensitive to radiation. However, using longer length scintillating tips should help reduce the relative noise from the optical fibers used in the FOC dosimetry system, and reference fibers may not be necessary to achieve a decent signal to noise ratio.

Finally, the count to dose calibration factors, λ_T , are functions of scintillating tip length. One might expect the response from a scintillating tip of length L in an FOC system to respond linearly with length, logarithmically with length, or proportionally to $(1-e^{-L})$. The dependence of λ_T on the scintillating tip length may complicate the tip length selection needed to achieve the relationship described in Equation 6-20. If for the scintillating tip lengths considered, FOC fiber counts behave linearly with scintillating tip length, then the relationship described in Equation 6-20 could be achieved by making the scintillating tip lengths proportional to their respective count to dose calibration factor. If FOC fiber counts do not behave linearly with scintillating tip length, then the response relationship could be studied further, or one could simply use trial and error.

Alternatively, one could couple fibers with equivalent dose responses from organs whose tissue weighting factors are equal; the coupled sum of these fibers could be read by a single PMT. Since ICRP 103 only uses five distinct tissue weighting factors⁵, only five PMTs would be necessary. If reference fibers are required, the exposure could be performed twice using the same five PMTs. The tissue weightings would then be applied to the sum response of groups of organs/tissues, instead of to each organ/tissue individually.

Conclusions

An alternative method for evaluating effective dose by using a dosimeter response weighted technique was derived. In instances where effective dose (or contributions toward effective dose by a few tissues) is all that is desired, this derived technique is less time consuming or tedious for TLD (OSL) dosimetry; using this method is less expensive and less time consuming in FOC dosimetry. Real-time effective dose measurements are possible, requiring less post measurement data manipulation. There are likely to be some challenges in applying this derived technique to FOC dosimetry.

CHAPTER 7 CONCLUSIONS

Results of This Work

The goal of this work was to develop an inexpensive, partially automated process for manufacturing anthropomorphic phantoms that are based upon tomographic data sets.

Dosimetric measurements using physical phantoms are useful in assessing the risk to patients undergoing diagnostic procedures. Physical phantom dosimetry is especially important considering that many diagnostic procedures are using advancing technology such as automatic tube current modulation (ATCM) in MDCT scanning, and automatic exposure control (AEC) in fluoroscopy, which are increasingly difficult to model. A tomographic physical phantom can also serve as a direct comparison to its computational “twin” phantom for the experimental validation of Monte Carlo codes.

As a result of this dissertation, a variety of physical phantom shapes and sizes can now be manufactured, improving their applicability to the patient population. Chapter 3 and Chapter 4 illustrated the effects that choice of detector collimation width has on patient organ doses. The relationship that detector collimation width has with overbeaming and overranging was also investigated. Chapter 4 compared measured and simulated average organ doses and their contributions to effective dose. The results were closer than previous comparative studies of physical and computational phantoms. Chapter 5 identified and quantified an inherent source of uncertainty when using point dosimetry in MDCT phantom studies, namely, the quasi-periodic dose distributions along the z-axis. Also presented was a theoretical method of reducing average organ dose to smaller, more peripheral organs/tissues that would not reduce image quality. Finally, a cost-effective, more convenient method of measuring effective dose contributions in physical phantoms was described.

Future Work and Development

Several opportunities for future work arise as natural extensions of the work presented in this dissertation. These prospective areas for research include phantom construction, the dose distribution to peripheral axes in MDCT, and FOC dosimetry.

Phantom Construction

Currently, three adult phantoms have been constructed using the process outlined in Chapter 2: GatorMan, a male adult hybrid phantom, and a female adult hybrid phantom. New phantoms of differing heights and weights can be constructed using the techniques that have been developed. Physical phantoms representing pregnant females at different stages of gestational development can be designed and constructed to facilitate fetal dose measurements, estimates, or reconstructions.

Phantoms available presently do not accurately represent obese patients. An adipose tissue-equivalent substitute (ATES) can be developed and incorporated into the phantom construction process. It could either be incorporated into the early slice construction stages, or added to the fully constructed phantoms.

The idea of constructing a phantom in coronal (instead of axial) slices has also been discussed. Although new obstacles would arise, a phantom organized in coronal sections would avoid an angular dependence in FOC dosimeters for CT applications, would circumvent some of the problems observed in holding axial sections of phantoms together, and would allow aliasing-free point dose measurements (as described in Chapter 5). It could also permit average organ dose measurements using FOC dosimetry based on integrated signals over lengths of scintillating fiber instead of point measurements.

Dose Distribution to Peripheral Axes in MDCT

The quasi-periodic dose distributions present in peripheral axes in phantoms during MDCT scanning were examined for pitch values of 1 and 1.5, and for detector collimation widths of 24 mm and 40 mm, at a few select organ locations. However, with some additional measurements and using the methodology in Chapter 5, a MATLAB program could be written that can provide expected normalized dose distributions for any combination of organ location, pitch value, and different detector collimation width. This would provide a means of knowing the level of inherent uncertainty in making point dose measurements with MDCT as well as the possible organ dose savings that can result from shifting the phase of the local MDCT dose distributions. It might be interesting to see how breast dose can be affected with larger pitch and detector collimation widths. Also, these predictions can be improved by using a more accurate model of the x-ray beam width (shape of penumbra, etc.). Doing so would slightly reduce the uncertainty and organ dose range for pitch 1, and would increase the uncertainty and organ dose range for pitch values greater than 1.

The predictions made in Chapter 5 could be compared against results from Monte Carlo simulations. This would be a simple matter in that the simulations could use a long scan whose starting and ending points were far from the organ being considered. The shift in phase of the local dose distribution could be accomplished by shifting the starting edge of the scan slightly between runs, while holding the starting angle constant (which is the case with the monte carlo code used in Chapter 4). Monte Carlo validation of potential organ dose savings could convince vendors to include the ability to visualize and control the location of the x-ray tube with respect to organ locations.

FOC Dosimetry

If any of the recommendations in Chapter 6 are to be attempted, fundamental studies on the system must be performed. The dosimeter response must be characterized with increasing lengths of scintillating fiber tips. Also, the uniformity and magnitude of attenuation when fibers are coupled must be studied. Once these things are characterized, real-time measurements of effective dose contributions from multiple organs may be performed for many different types of radiation exposures. Coordinating this data with details of the exposure will allow researchers to identify which aspects of an exposure contribute the greatest risk to a patient. It will therefore be easier to target adjustments in exposures that will minimize those risks.

Final Words

There are statistically significant risks to patients associated with the radiation exposure received during MDCT studies. It is in the interests of patients to minimize these risks. Before one can minimize the risks to patients, one must be able to assess the risk, and physical anthropomorphic phantoms are an essential tool for dose/risk assessment in MDCT. The construction process described previously can be used to construct a phantom based on any segmented tomographic data set, and so, every patient group (or individual) can have a representative physical phantom. Physical validation of computational phantoms and simulations can facilitate widespread distribution and adoption of computational models, which can subsequently be used to adjust MDCT scan parameters to minimize the radiation dose to patients. Providing a reliable means to quantify and reduce the risk to patients receiving MDCT procedures was the underlying objective of this project, and the constantly improving series of physical/computational phantoms at the University of Florida achieves this goal.

LIST OF REFERENCES

1. D. J. Brenner and E. J. Hall, "Computed tomography--an increasing source of radiation exposure," *N Engl J Med* **357**, 2277-2284 (2007).
2. H. D. Royal, "Effects of low level radiation-what's new?," *Semin Nucl Med* **38**, 392-402 (2008).
3. D. Hintenlang, "OSL Based Anthropomorphic Phantom and real-Time Dosimetry," (2005).
4. C. H. McCollough, M. R. Bruesewitz, M. F. McNitt-Gray, K. Bush, T. Ruckdeschel, J. T. Payne, J. A. Brink and R. K. Zeman, "The phantom portion of the American College of Radiology (ACR) computed tomography (CT) accreditation program: practical tips, artifact examples, and pitfalls to avoid," *Med Phys* **31**, 2423-2442 (2004).
5. "The 2007 Recommendations of the International Commission on Radiological Protection. ICRP publication 103," *Ann ICRP* **37**, 1-332 (2007).
6. W. Huda, J. G. Ravenel and E. M. Scalzetti, "How do radiographic techniques affect image quality and patient doses in CT?," *Semin Ultrasound CT MR* **23**, 411-422 (2002).
7. D. Lockwood, "Diagnostic imaging: Radiation dose and patients' concerns," *J Radiol Nursing* **26**, 121-124 (2007).
8. E. Cardis, M. Vrijheid, M. Blettner, E. Gilbert, M. Hakama, C. Hill, G. Howe, J. Kaldor, C. R. Muirhead, M. Schubauer-Berigan, T. Yoshimura, F. Bermann, G. Cowper, J. Fix, C. Hacker, B. Heinmiller, M. Marshall, I. Thierry-Chef, D. Utterback, Y. O. Ahn, E. Amoros, P. Ashmore, A. Auvinen, J. M. Bae, J. Bernar, A. Biau, E. Combalot, P. Deboodt, A. Diez Sacristan, M. Eklof, H. Engels, G. Engholm, G. Gulis, R. R. Habib, K. Holan, H. Hyvonen, A. Kerekes, J. Kurtinaitis, H. Malker, M. Martuzzi, A. Mastauskas, A. Monnet, M. Moser, M. S. Pearce, D. B. Richardson, F. Rodriguez-Artalejo, A. Rogel, H. Tardy, M. Telle-Lamberton, I. Turai, M. Usel and K. Veress, "The 15-Country Collaborative Study of Cancer Risk among Radiation Workers in the Nuclear Industry: estimates of radiation-related cancer risks," *Radiat Res* **167**, 396-416 (2007).
9. D. L. Preston, D. A. Pierce, Y. Shimizu, H. M. Cullings, S. Fujita, S. Funamoto and K. Kodama, "Effect of recent changes in atomic bomb survivor dosimetry on cancer mortality risk estimates," *Radiat Res* **162**, 377-389 (2004).
10. National Research Council (U.S.). Committee to Assess Health Risks from Exposure to Low Level of Ionizing Radiation., *Health risks from exposure to low levels of ionizing radiation : BEIR VII Phase 2*. (National Academies Press, Washington, D.C., 2006).
11. A. D. Wrixon, "New ICRP recommendations," *J Radiol Prot* **28**, 161-168 (2008).

12. F. A. Mettler, Jr., P. W. Wiest, J. A. Locken and C. A. Kelsey, "CT scanning: patterns of use and dose," *J Radiol Prot* **20**, 353-359 (2000).
13. C. Hohl, A. H. Mahnken, E. Klotz, M. Das, A. Stargardt, G. Muhlenbruch, T. Schmidt, R. W. Gunther and J. E. Wildberger, "Radiation dose reduction to the male gonads during MDCT: the effectiveness of a lead shield," *AJR Am J Roentgenol* **184**, 128-130 (2005).
14. C. Hohl, J. E. Wildberger, C. Suss, C. Thomas, G. Muhlenbruch, T. Schmidt, D. Honnef, R. W. Gunther and A. H. Mahnken, "Radiation dose reduction to breast and thyroid during MDCT: effectiveness of an in-plane bismuth shield," *Acta Radiol* **47**, 562-567 (2006).
15. G. F. Knoll, *Radiation detection and measurement*, 3rd ed. (Wiley, New York, 2000).
16. C. Kawaura, T. Aoyama, S. Koyama, M. Achiwa and M. Mori, "Organ and effective dose evaluation in diagnostic radiology based on in-phantom dose measurements with novel photodiode-dosimeters," *Radiat Prot Dosimetry* **118**, 421-430 (2006).
17. T. Aoyama, S. Koyama and C. Kawaura, "An in-phantom dosimetry system using pin silicon photodiode radiation sensors for measuring organ doses in x-ray CT and other diagnostic radiology," *Med Phys* **29**, 1504-1510 (2002).
18. S. L. Dong, T. C. Chu, G. Y. Lan, T. H. Wu, Y. C. Lin and J. S. Lee, "Characterization of high-sensitivity metal oxide semiconductor field effect transistor dosimeters system and LiF:Mg,Cu,P thermoluminescence dosimeters for use in diagnostic radiology," *Appl Radiat Isot* **57**, 883-891 (2002).
19. E. G. Yukihiro and S. W. McKeever, "Optically stimulated luminescence (OSL) dosimetry in medicine," *Phys Med Biol* **53**, R351-379 (2008).
20. F. Lacroix, L. Archambault, L. Gingras, M. Guillot, A. S. Beddar and L. Beaulieu, "Clinical prototype of a plastic water-equivalent scintillating fiber dosimeter array for QA applications," *Med Phys* **35**, 3682-3690 (2008).
21. L. M. Hurwitz, T. T. Yoshizumi, P. C. Goodman, D. P. Frush, G. Nguyen, G. Toncheva and C. Lowry, "Effective dose determination using an anthropomorphic phantom and metal oxide semiconductor field effect transistor technology for clinical adult body multidetector array computed tomography protocols," *J Comput Assist Tomogr* **31**, 544-549 (2007).
22. J. Lambert, T. Nakano, S. Law, J. Elsey, D. R. McKenzie and N. Suchowerska, "In vivo dosimeters for HDR brachytherapy: a comparison of a diamond detector, MOSFET, TLD, and scintillation detector," *Med Phys* **34**, 1759-1765 (2007).

23. T. T. Yoshizumi, P. C. Goodman, D. P. Frush, G. Nguyen, G. Toncheva, M. Sarder and L. Barnes, "Validation of metal oxide semiconductor field effect transistor technology for organ dose assessment during CT: comparison with thermoluminescent dosimetry," *AJR Am J Roentgenol* **188**, 1332-1336 (2007).
24. A. K. Jones, F. D. Pazik, D. E. Hintenlang and W. E. Bolch, "MOSFET dosimeter depth-dose measurements in heterogeneous tissue-equivalent phantoms at diagnostic x-ray energies," *Med Phys* **32**, 3209-3213 (2005).
25. B. D. Pomije, C. H. Huh, M. A. Tressler, D. E. Hintenlang and W. E. Bolch, "Comparison of angular free-in-air and tissue-equivalent phantom response measurements in p-MOSFET dosimeters," *Health Phys* **80**, 497-505 (2001).
26. W. E. Moloney, University of Florida, 2008.
27. C. D. Villagrasa, J. Clairand, I. Queinnec, F. Furstoss, C. Bottollier-Depois, J.F., "Anthropomorphic phantom for effective dose measurements: Feasibility numerical study and presentation of the detector development," *Radiation Measurements* **43**, 590-593 (2008).
28. A. K. Jones and D. Hintenlang, "Potential clinical utility of a fibre optic-coupled dosimeter for dose measurements in diagnostic radiology," *Radiat Prot Dosimetry* **132**, 80-87 (2008).
29. C. H. McCollough, A. N. Primak, N. Braun, J. Kofler, L. Yu and J. Christner, "Strategies for reducing radiation dose in CT," *Radiol Clin North Am* **47**, 27-40 (2009).
30. E. K. Fishman, "The increasing impact of multidetector row computed tomography in clinical practice," *Eur J Radiol* **62S**, S1-S13 (2007).
31. B. L. Fricke, L. F. Donnelly, D. P. Frush, T. Yoshizumi, V. Varchena, S. A. Poe and J. Lucaya, "In-plane bismuth breast shields for pediatric CT: effects on radiation dose and image quality using experimental and clinical data," *AJR Am J Roentgenol* **180**, 407-411 (2003).
32. D. E. Heaney and C. A. Norvill, "A comparison of reduction in CT dose through the use of gantry angulations or bismuth shields," *Australas Phys Eng Sci Med* **29**, 172-178 (2006).
33. J. Valentin, "Managing patient dose in multi-detector computed tomography(MDCT). ICRP Publication 102," *Ann ICRP* **37**, 1-79, iii (2007).
34. D. P. Frush, "Review of radiation issues for computed tomography," *Semin Ultrasound CT MR* **25**, 17-24 (2004).

35. D. P. Frush and K. Applegate, "Computed tomography and radiation: understanding the issues," *J Am Coll Radiol* **1**, 113-119 (2004).
36. D. R. White, "The formulation of tissue substitute materials using basic interaction data," *Phys Med Biol* **22**, 889-899 (1977).
37. D. R. White, "Tissue substitutes in experimental radiation physics," *Med Phys* **5**, 467-479 (1978).
38. D. R. White, C. Constantinou and R. J. Martin, "Foamed epoxy resin-based lung substitutes," *Br J Radiol* **59**, 787-790 (1986).
39. D. R. White, R. J. Martin and R. Darlison, "Epoxy resin based tissue substitutes," *Br J Radiol* **50**, 814-821 (1977).
40. ICRU, 1989.
41. D. Hintenlang, W. Moloney, and J. Winslow, *Physical phantoms for experimental radiation dosimetry*, Chapter 14, in *Handbook of anatomical models for radiation dosimetry*, Edited by X.G. Xu and K.F. Eckermann, CRC Press, In Review.
42. J. T. Bushberg, *The essential physics of medical imaging*, 2nd ed. (Lippincott Williams & Wilkins, Philadelphia, 2002).
43. B. Li, G. B. Avinash, J. W. Eberhard and B. E. Claus, "Optimization of slice sensitivity profile for radiographic tomosynthesis," *Med Phys* **34**, 2907-2916 (2007).
44. B. Li, G. B. Avinash and J. Hsieh, "Resolution and noise trade-off analysis for volumetric CT," *Med Phys* **34**, 3732-3738 (2007).
45. M. W. Kan, L. H. Leung, W. Wong and N. Lam, "Radiation dose from cone beam computed tomography for image-guided radiation therapy," *Int J Radiat Oncol Biol Phys* **70**, 272-279 (2008).
46. R. J. Staton, A. K. Jones, C. Lee, D. E. Hintenlang, M. M. Arreola, J. L. Williams and W. E. Bolch, "A tomographic physical phantom of the newborn child with real-time dosimetry. II. Scaling factors for calculation of mean organ dose in pediatric radiography," *Med Phys* **33**, 3283-3289 (2006).
47. A. K. Jones, D. E. Hintenlang and W. E. Bolch, "Tissue-equivalent materials for construction of tomographic dosimetry phantoms in pediatric radiology," *Med Phys* **30**, 2072-2081 (2003).
48. C. Lee, S. H. Park and J. K. Lee, "Development of the two Korean adult tomographic computational phantoms for organ dosimetry," *Med Phys* **33**, 380-390 (2006).

49. International Commission on Radiation Units and Measurements., *Tissue substitutes in radiation dosimetry and measurement*. (International Commission on Radiation Units and Measurements, Bethesda, Md., U.S.A., 1989).
50. R. Fisher, University of Florida, 2006.
51. M. Cristy and K. F. Eckerman, "Specific absorbed fractions of energy at various ages from internal photon sources. ORNL/TM 8381," ORNL **VI-VII** (1987).
52. A. K. Jones, T. A. Simon, W. E. Bolch, M. M. Holman and D. E. Hintenlang, "Tomographic physical phantom of the newborn child with real-time dosimetry I. Methods and techniques for construction," *Med Phys* **33**, 3274-3282 (2006).
53. C. Lee, D. Lodwick, D. Hasenauer, J. L. Williams and W. E. Bolch, "Hybrid computational phantoms of the male and female newborn patient: NURBS-based whole-body models," *Phys Med Biol* **52**, 3309-3333 (2007).
54. C. Lee, D. Lodwick, J. L. Williams and W. E. Bolch, "Hybrid computational phantoms of the 15-year male and female adolescent: applications to CT organ dosimetry for patients of variable morphometry," *Med Phys* **35**, 2366-2382 (2008).
55. Clinical Protocol Database, radiology practice Committee of the Department of Radiology, University of Florida. Copyright 2008.
56. "Basic anatomical and physiological data for use in radiological protection: reference values. A report of age- and gender-related differences in the anatomical and physiological characteristics of reference individuals. ICRP Publication 89," *Ann ICRP* **32**, 5-265 (2002).
57. F. Martini and W. C. Ober, *Fundamentals of anatomy & physiology*, 5th ed. (Prentice Hall, Upper Saddle River, N.J., 2001).
58. R. J. Staton, C. Lee, M. D. Williams, D. E. Hintenlang, M. M. Arreola, J. L. Williams and W. E. Bolch, "Organ and effective doses in newborn patients during helical multislice computed tomography examination," *Phys Med Biol* **51**, 5151-5166 (2006).
59. A. Tzedakis, J. Damilakis, K. Perisinakis, J. Stratakis and N. Gourtsoyiannis, "The effect of z overscanning on patient effective dose from multidetector helical computed tomography examinations," *Med Phys* **32**, 1621-1629 (2005).
60. A. J. van der Molen and J. Geleijns, "Overranging in multisection CT: quantification and relative contribution to dose--comparison of four 16-section CT scanners," *Radiology* **242**, 208-216 (2007).
61. R. L. Dixon, "A new look at CT dose measurement: beyond CTDI," *Med Phys* **30**, 1272-1280 (2003).

62. R. L. Dixon and A. C. Ballard, "Experimental validation of a versatile system of CT dosimetry using a conventional ion chamber: beyond CTDI100," *Med Phys* **34**, 3399-3413 (2007).
63. R. L. Dixon, M. T. Munley and E. Bayram, "An improved analytical model for CT dose simulation with a new look at the theory of CT dose," *Med Phys* **32**, 3712-3728 (2005).

BIOGRAPHICAL SKETCH

James Frederick Winslow was born in Long Island, New York to Robert and Bonnie Winslow. He is one of three children born to Robert and Bonnie, along with his older brother Robert, and younger brother Kenneth. He graduated from Island Trees High School in Levittown, New York. He then graduated from the State University of New York at Potsdam, where he earned a Bachelor of Arts degree in physics, and another in speech communication. He then attended the University of South Florida in Tampa, Florida. There, he earned a Master of Science degree in physics from the Physics Department, and another in engineering science from the Electrical Engineering Department.